ELECTRICAL CONDUCTION AND RESISTIVE SWITCHING IN POLYMER AND BIODEGRADABLE NANOCOMPOSITES

By

Zolile Wiseman Dlamini

submitted in accordance with the requirements for the degree of

DOCTOR OF PHILOSOPHY

in the subject

PHYSICS

at the

UNIVERSITY OF SOUTH AFRICA

PRINCIPAL SUPERVISOR

Prof. V. S. Vallabhapurapu

CO-SUPERVISORS

DR. S. Vallabhapurapu and DR. S. Wu

18 October, 2022

DECLARATION

Name: **Zolile Wiseman Dlamini**

Student number: **46118357**

Degree: **Doctor of Philosophy in Physics**

Dissertation title: **ELECTRICAL CONDUCTION AND RESISTIVE SWITCHING IN POLYMER AND BIODEGRADABLE NANOCOMPOSITES**

I declare that the above thesis is my own work and that all the sources that I have used or quoted have been indicated and acknowledged by means of complete references.

I further declare that I submitted the thesis to originality checking software and that it falls within the accepted requirements for originality.

I further declare that I have not previously submitted this work, or part of it, for examination at UNISA for another qualification or at any other higher education institution.

Signature:

ACKNOWLEDGEMENTS

I want to extend my deepest gratitude to my principal Supervisor, Prof. Vallabhapurapu, for showing trust and belief in me and, especially, his guidance throughout this study. Likewise, I thank my co-supervisors, Dr Sreedevi Vallabhapurapu and Dr Shuying Wu, for their valuable contribution to this study.

I am also grateful to the South African Government for the nGAP program and NRF funding. The nGAP and NRF management structure and mentors at Central University of Technology have supported me throughout this study, and I am deeply grateful.

I am also grateful for my collaboration with Walter Sisulu University and Rhodes University researchers and everybody who collaborated with me.

I am grateful to Anton Paar, particularly Jocelyne Abreu, for a free AFM training and her assistance in the AFM study used in this work.

Dedication

I dedicated this thesis to the entire Dlamini family. Specifically, my beloved mother, Jabulile Dlamini; my late sisters Nosipho and Thobile Dlamini; my brother, Sandile Dlamini; niece Anele Dlamini; nephew, Alwande Dlamini. Lastly, but not list my lovely sons, Mivuyo, Hlalumi and Luncumo.

LIST OF PATENTS AND PUBLICATIONS

LIST OF PATENTS

Zolile Wiseman Dlamini, Sreedevi Vallabhapurapu and Vijaya Srinivasu Vallabhapurapu. ***"Nonvolatile Resistive Random Access Memory And A Manufacturing Method Thereof"*** (**PA176739/PCT**)

LIST OF PUBLICATIONS

Z. W. Dlamini, S. Vallabhapurapu, O. A. Daramola, P. F. Tseki, R. W. M. Krause, X. Siwe-Noundou, T. S. Mahule, and S. V. Vallabhapurapu, *"Resistive Switching in CdTe/CdSe core-shell quantum dots embedded Chitosan-based Memory devices".* **Journal of Circuits, Systems and Computers, Vol. 31, 6, 1-16(2021). https://doi.org/10.1142/S0218126622501134**

Z. W. Dlamini, S. Vallabhapurapu, O. A. Daramola, P. F. Tseki, R. W. M. Krause, X. Siwe-Noundou, T. S. Mahule, and S. V. Vallabhapurapu, *"Resistive Switching in Drop cast CdTe/CdSe Quantum Dots Embedded Chitosan Composite".***Iranian Journal of Science and Technology, Transition A: Science, Vol 43, 2, 709-716, 2022. https://doi.org/10.1007/s40995-022-01272-y**

Zolile Wiseman Dlamini, Sreedevi Vallabhapurapu, Ananthakrishnan Srinivasan, Shuying Wu, and Vijaya Srinivasu Vallabhapurapu, *"Resistive Switching in Polyvinylpyrrolidone/Molybdenum disulfide composite-based Memory devices".* **Acta Physica Polonica, Vol. 141, 5, 439-444 2022. http://przyrbwn.icm.edu.pl/APP/PDF/141/app141z5p01.pdf**

Zolile Wiseman Dlamini, Sreedevi Vallabhapurapu, Shuying Wu,

Tebogo Sfiso Mahule, Ananthakrishnan Srivivasan and Vijaya SrinivasuVallabhapurapu, *"Resistive Switching Memory based on Chitosan/ Polyvinylpyrrolidone blend as active layers".* **Solid State Communications, Vol. 345, 1 April 2022, 114677.**
https://doi.org/10.1016/j.ssc.2022.114677

Zolile Wiseman Dlamini, Sreedevi Vallabhapurapu, and Vijaya Srinivasu Vallabhapurapu, *"Resistive switching memory based on Raw Cow Milk".* **CMC-Journal of Computers, Matterials Contina** (**Accepted**).

Abstract

Modern memory devices such as static random-access memory (SRAM), dynamic random-access (DRAM), and Flash memories demonstrated inevitable limitations, i.e., large cell size ($50 - 120\ F^2$) of SRAM, accompanied by current leakage; high operating voltages of 3 V and up to 6 V for DRAM and NOR Flash, respectively; DRAM capacity should sustain enough charges (there is a limit to how small the DRAM capacitor can be) and Flash need a novel array structure. Additionally, these current memory devices contribute significantly to the world's earth pollution. These memories still use heavy metals such as Pb, which are harmful to humans. There is a demand for a next-generation random-access memory (RAMs) having fast read and write operations as the SRAM, high density and cost-benefit as the DRAM, and nonvolatility as the Flash. Furthermore, new memory device must be compatible with on-chip computing. Resistive switching memories (ReRAMs) are an emerging memory technology with prospects of combined benefit found in all current memories. Furthermore, ReRAMs can be fabricated using any material, including organic polymers and biological materials. This gives ReRAM environmentally friendly properties and compatibility with futuristic electronics, where special mechanical properties such as transparency and flexibility are important. In this study, we conducted intense research on electrical conduction and resistive switching in biodegradable polymers such as chitosan and polyvinylpyrrolidone, and in the process, we discovered, for the first time, resistive switching in raw cow milk.

First resistive switching and conduction mechanisms in spin-coated devices consisting ofcadmium telluride/cadmium selenide (CdTe/CdSe) core-shell quantum dots embedded in a chitosan active layer sandwiched between (1) aluminium (Al) and silver (Ag) and (2) indium-doped tin oxide (ITO)

and Ag electrodes were studied. Here, both devices exhibited bipolar memory behavior at low (+0.70 V) voltage, enabling both devices to be operated at low powers. The devices displayed different switching mechanisms, i.e., conductive bridge mechanism in the Al-based device and space-charge-limited driven conduction filament attributed in the ITO device. Additionally, the Al-based device showed long retention ($> 10^3$ s) and a reasonable large ($> 10^3$) ON/OFF ratio. We also observed a sweeping cycle-induced reversal of the voltage polarity of the V_{SET} and V_{RESET} in the Al-based device, which is a new observation. Using the same composite but changing the film deposition method, i.e., now using the drop-casting method. All devices consisting of 0.96 $wt\%$, 0.48 $wt\%$, 0.32 $wt\%$ and 0.24 $wt\%$ CdTe/CdSe QDs to chitosan showed 'O-type' memory behavior with OFF-state current conduction mechanism attributed to the hopping mechanism. However, the ON-state current in each device followed a unique mechanism, such that Ohmic behavior was observed for the device with 0.96 $wt\%$, while linear then hopping, space-charge limited, and lastly, hopping conduction mechanisms were attributed to devices with 0.48 $wt\%$, 0.32 $wt\%$ and 0.24 $wt\%$, respectively. Proving that memory behavior and conduction in these devices can be exploited by controlling the amount of CdTe/CdSe.

Next, we investigated the effect of molybdenum(IV) sulfide (MoS_2) on both conduction and memory behavior in polyvinylpyrrolidone (PVP) by fabricating various ReRAM devices using (1) plain MoS_2 (device A), (2) plain PVP (device B), (3) PVP and MoS2 bilayer (device C), and (4) PVP $+MoS_2$ nanocomposites with 10 $wt\%$ (device D), 20 $wt\%$ (device E), 30 $wt\%$ (device F) and 40 $wt\%$ (device G) MoS_2 fabricated with Al and Ag as bottom and top electrodes, respectively. We did not observe switching in devices A and B. Device C showed a combination of bipolar and threshold switching at 0.40 V. Device G portrayed bipolar switching at 0.56 V. In Device C, space charge-limited conduction while Ohmic behavior followed by trapping of charge before switching was noticed in device G. Both devices C and G showed reasonably ($\geq 10^2$) ON/OFF ratio. In the nanocomposite devices, we observed that an increase in MoS_2 content increased electrical conductivity in the Ohmic region, leading to threshold switching at 30 $wt\%$ (device F) and ultimately bipolar switching at 40 $wt\%$ (device G). These studies showed that both switching and conduction mechanisms are sensitive to the type and composition of the active layer in the devices studied.

Next, we investigated resistive switching in chitosan/PVP composite as the active layers sandwiched between Al and Ag electrodes. ReRAMs with active layers consisting of 1 : 3, 1 : 1, and 3 : 1 chitosan to PVP ratios were studied. Asymmetric threshold switching with only the negative voltage bias was obtained for the device with a chitosan to PVP ratio of 1 : 3. The 1 : 1 chitosan to PVP ratio device showed optimal memory behavior with bipolar switching with low (0.28 V) switching voltage in the first cycle, followed by asymmetric threshold switching during the second cycle and back to bipolar switching. We did not observe memory behavior in the 3 : 1 chitosan to PVP-based device. Electrochemical conduction metalization was attributed to the switching mechanism in the device with a 1 : 1 ratio of chitosan to PVP. Our results reveal the applicability of chitosan and PVP blend in memory device fabrication and that both the memory and switching can be exploited by varying the ratio of chitosan to PVP in the composite.

Lastly, we fabricated the first resistive switching memory devices that use raw organic cow milk as active layers. Our devices comprised fat-free, medium cream, and full cream raw cow milk active layers sandwiched between ITO and Ag. All devices showed low switching voltages, with the medium fat milk-based device showing the lowest $V_{SET} = +0.45\ V$ and $V_{RESET} = -0.25\ V$. Additionally, the medium fat-based device showed an ‘S-type’ memory mode attributed to the space-charge-limited conduc-

tion mechanism. Alternatively, fat-free and fill-cream-based devices both showed ‘O-type’ memory behavior attributed to hopping conduction. EDS analysis of all active layers revealed a relatively higher weight percentage of metallic ions in the medium fat milk film than in fat-free and full-cream milk films, which explains the different behaviors. These devices combine biodegradability and low power characteristics that are important for green computing.

Keywords: Biodegradable memories; CdTe/CdSe core-shell quantum dots; Chitosan; Cow milk; Green computing; Low power memory devices; MoS_2; Non-volatile memory; PVP; Resistive switching

List of acronyms and abbreviations

- AFM - Atomic force microscope
- ASCII - American standard code for information interchange
- BE - Bottom electrode
- BL - Bitline
- CBRAM - Conductive bridge random access memory
- CD - Compact disc
- CF - Conductive filament
- CPU - Central processing unit
- DRAM - Dynamic random access memory
- DVD - Digital versatile disc ECM - Electrochemical metallization
- EDS - Energy dispersive spectroscope
- E-Waste - Electronic waste

- FeRAM - Ferroelectric random access memory
- HHD - Hard disc drive
- HRS- High resistive state
- IT - Information technology
- LRS - Low resitive state
- MLC - Multi-level cell
- MRAM - Magnetic random access memory
- NVM - nonvolatile memory
- PCRAM - Phase change memory
- RAM - Random access memory
- ReRAM resistive switching memory
- SCLC - Space charge-limited conduction
- SEM -Scanning electron microscope
- SRAM - Static random access memory
- SSD - Solid-state drive
- STT-RAM - Sin-transfer torque random access memory
- TE - Top electrode
- TMR - Tunneling magnetoresistance
- USB - Universal serial bus
- VM - Volatile memory
- WL - Wordline

Contents

1 Introduction 1

1.1 Basics of memory devices 2

1.1.1 Volatile memory 5

1.1.2 Nonvolatile memories (NVM) 7

1.2 Prototypical memories 12

1.2.1 Ferroelectric Random-Access Memory (FeRAM) . . . 12

1.2.2 Phase change random access memory (PCRAM) . . . 13

1.2.3 Magnetic random-access memories (MRAMs) 15

1.2.4 Resistive switching memory (ReRAM) 17

1.2.5 Materials for ReRAM devices 26

1.3 Identification of research problem 29

1.3.1 Problem statement 29

1.3.2 Aim/Purpose of the study 30

1.3.3 Research objectives 30

1.4 Thesis Outline 31

2 Fabrication, characterization and experiment techniques of memory devices 32

2.1 Introduction 32

2.2 Thin-film deposition and device fabrication 34

2.3 Characterization 35

2.3.1 Topography and Morphology study 35

2.3.2 Electrical transport study using the Keysight SMU . . 37

3 Resistive Switching in CdTe/CdSe core-shell quantum dots embedded Chitosan-based Memory devices 39

3.1 Introduction 39

3.2 Experimental details 41

3.2.1 Materials and methods 41

3.2.2 Memory device fabrication 42

3.2.3 Characterization 42

3.3 Results and discussion 43

3.3.1 Topography study and thickness study 43

3.3.2 Conduction and memory study 45

3.3.3 Conduction and resistive switching mechanisms 50

3.4 Conclusion 54

4 Conduction and Resistive Switching in Drop-cast CdTe/CdSe Core-Shell Quantum Dots Embedded Chitosan Composite 56

4.1 Introduction 56

4.2 Experimental details 57

4.2.1 Materials and methods 57

4.2.2 ReRAM fabrication 58

4.2.3 Characterization 59

4.3 Results and discussion 59

4.3.1 Topography 59

4.3.2 Electrical study 59

4.3.3 Conduction mechanism discussion 66

4.4 Conclusion 69

5 Resistive Switching in Polyvinylpyrrolidone/ Molybdenum disulfide composite-based Memory devices. 70

5.1 Introduction 70

5.2 Experimental details 72

5.2.1 Solution preparation 72

5.2.2 Device Fabrication 72

5.2.3 Device characterization 72

5.3 Results and discussion 73

5.3.1 Topology and composition 73

5.3.2 Electrical studies 75

5.3.3 Conduction mechanisms and RS in devices C and G . 77

5.4 Conclusion 81

6 Resistive switching memory based on chitosan/ polyvinyl pyrrolidone blend as active layers 82

6.1 Introduction 82

6.2 Experimental details 84

6.2.1 Solution Preparation 84

6.2.2 Device fabrication 84

6.2.3 Device characterization 85

6.3 Results and discussion 86

6.3.1 Morphology characterization 86

6.3.2 Electrical conduction and Memory behaviour 86

6.4 Switching mechanism in Al/chitosan+PVP(1:1) /Ag device . 96

6.5 Conclusion 98

7 Resistive Switching Memory-Based on Raw Cow Milk 99

7.1 Introduction 99

7.2 Experimental Details 100

7.3 Results and Discussion 101

7.3.1 Morphology and Topography 101

7.3.2 Electrical Transport and Memory Study 103

7.4 Conduction Mechanism Analysis 109

7.5 Conclusion 113

8 Conclusion 117

8.0.1 Future research 120

List of Figures

1.1 The schematic diagram of (a) a typical memory device and (b) a typical memory hierarchy. 3

1.2 Classification of current and emerging memory devices [Vallabhapurapu2018a]. 4

1.3 schematic diagrams showing two designs of a 1-bit SRAM cell. Design (a) consists of four transistors plus two additional transistors, while design (b) consists of four transistors and two resistors [Aliakhmet2018]. 5

1.4 A schematic diagram shows a primary organization of DRAM internals, while the magnified image shows the 1T1C DRAM cell[Jacob2009]. 6

1.5 (a) A schematic diagram of a typical ROM. Reprinted from [Li2012]. A schematic diagram showing a series connection of a MOSFET transistor and a floating gate transistor in an EEPROM cell (b). 9

1.6 A cross-sectional area of a typical flesh memory (a) and a 1-bit flash memory cell symbol (b). 10

1.7 Schematic diagrams showing (a) NOR and (b) NAND Flash memory arrays. Reprinted from [Autran2014]. 11

1.8 A schematic diagram showing a hysteresis loop in polarization versus electric field for a ferroelectric film. Reprinted from [Eshita2014]. 13

1.9 A schematic diagram showing (a) the basic design of a phase change memory cell and (b) the temperature versus time for a conventional PRAM. Reprinted from [Wong2010]. 14

1.10 A schematic diagram showing the low and high resistive states for an MTJ MRAM. Reprinted form [Apalkov2016]. 16

1.11 A diagram showing a basic design of a ReRAM cell 17

1.12 A basic schematic diagram of a typical ReRAM (a) cell and (b) a configuration of a crossbar array of a ReRAM memory. 18

1.13 Schematic diagrams showing dc current-voltage relationship for unipolar (a) and bipolar RS modes (b)[Pan2010a]. 20

1.14 I-V hysteresis showing O-type RS mode[48], (b) N-type, as well as (c) symmetric and asymmetric S-type RS modes (d)[Prime2009] 21

1.15 Classification of resistive switching mechanisms. Reprinted from[Wang2018a]. 22

1.16 A schematic diagram showing a series of events in a filament type conduction mechanism. (a) a fresh sample, (b) the presence of a conduction filament after the forming process, (c), and (d) the partial rupture and reformation of the conduction filament, respectively. 23

1.17 Formation and rapture of conduction filaments using oxidation and reduction of the electrodes. 24

1.18 A schematic diagram showing the formation of virtual CF using oxygen vacancies. 25

1.19 This image shows an 8 × 8 array Ti/Au/Al/Pi: PCBM/Al flexible organic memory. (a) a schematic and (b) optical images. (c) and (d) respectively show the schematic diagram and the SEM micrograph of the cross-section of the device. This image is taken from[Ouyang2016]. 28

1.20 The classification of organic materials for ReRAM active layers. This image is taken from[Li2020]. 29

2.1 Molecular diagram of (a) chitosan and (b) PVP polymers (Images are taken from wikiwand.com.) 33

2.2 Schematic diagram depicting the steps involved in the spin-coating method. 34

2.3 The photograph of a spin coating machine available at UNISA 35

2.4 A photograph of a Nanosurf FlexAFM available at UNISA, and (b) a schematic diagram showing the working principle of a typical AFM. 36

2.5 (a) the photograph of a JEOL JSM FE-SEM available at UNISA labs, and (b) a typical SEM schematic diagram. Image is taken from[NanoScienceinstruments2018]. 37

2.6 Schematic diagram showing different signals obtained from a FEG-SEM specimen. Image is taken from[JeolManual]. . . . 38

2.7 A photograph of the Keysight precision source/measure unit (SMU) B2901A available at UNISA. 38

3.1 This figure shows a schematic diagram of the memory device fabricated on Al substrate, also showing is the simplified circuit of the current-voltage studies 43

3.2 This image shows a 1 $\mu m \times 1 \mu m$ (a)FEG-SEM and (b) AFM phase trace images showing the distribution of QDs in the chitosan medium. (c) is a 5 μm AFM height trace image, while (d) is a 3D plot of the height trace image of the selected area in (c). (e) shows the line profiles constructed over the area selected in (c). 44

3.3 This image shows the thickness measurements of the active layers using step method. (a) shows the topography scan taken over the edge of the sample, and (b) is the corresponding 3D chart view.(d) shows the point-to-point estimation of the thickness. 45

3.4 Typical I-V curve showing electrical characteristics of the ReRAM devices that use (a) bare CdTe/CdSe QDs and (b) bare chitosan as active layers sandwiched between ITO and Ag electrodes. 46

3.5 Typical I-V curves showing electrical characteristics of the Al/Chitosan+QDs/Ag device. (a) is the I-V curve for the electroforming process. (b) is the semi-log curves showing the memory behaviour during the 1st voltage sweeping cycle. (c) is the semi-log curves showing the memory behaviour during 260 voltage sweeping cycles, while (d) shows the 200th cycle showing interchanged V_{SET} and V_{RESET} polarities. (e) is resistance versus time graph showing the retention properties of the Al/chitosan+QDs/Ag device within the 2000 s. 47

3.6 Typical I-V curves showing electrical characteristics of the PET-ITO/Chitosan+QDs/Ag device. (a) is the I-V curve for the electroforming process. (b) is the semi-log curves showing the memory behaviour during the 1st voltage sweeping cycle. (c) is the semi-log curves showing the memory behaviour during 10 voltage sweeping cycles, while (d) shows the 11th cycle showing that the device has lost its memory behaviour. (e) shows the ON- and OFF- state resistance against sweeping cycles showing endurance of the PET-ITO/chitosan+QDs/Ag device under 11 consecutive voltage sweeping cycles. The inset shows loss of memory beyond the 6th cycle. 49

3.7 log-log fitting results of the conduction mechanism for the Al/Chitosan+QDs/Ag device. (a) and (b) show the positive and negative voltage bias region for the first sweeping cycle, while (c) and (d) is for the 200th sweeping cycle. 53

3.8 Log-log fitting results of the conduction mechanism for the PET-ITO/Chitosan+QDs/Ag device. (a) shows the positive voltage bias region, while (b) shows the negative voltage bias region. 53

4.1 A schematic diagram depicting a cross-sectional are of a ReRAM device consisting of chitosan and CdTe/CdSe core shell QDs with Ag and Al electrodes. The circuit diagram shows a simplified experimental setup for current-voltage measurements . 58

4.2 (a) FEG-SEM micrograph, and AFM height trace images of the chitosan/CdTe/CdSe active layer in (b) 2D and (c) 3D. . 60

4.3 Electroforming I-V characteristics of the Al/chitosan/QDs(S1)/Ag device 61

4.4 I-V characteristics of the Al/chitosan/QDs(S2)/Ag device, showing the electroforming curve. 62

4.5 I-V characteristics of the Al/chitosan/QDs(S3)/Ag device showing the electroforming curve. 64

4.6 I-V characteristics of the Al/chitosan/QDs(S4)/Ag device, showing the first cycle. 65

4.7 Figures a-d show the $\ln I - \ln V$ linear fitting, while the insets show the exponential function fitting of the I-V data for the (a) Al/chitosan/QDs(S1)/Ag, (b) Al/chitosan/QDs(S2)/Ag and (c) Al/chitosan/QDs(S3)/Ag devices. (d) shows the exponential fitting of the I-V data for the Al/chitosan/QDs(S4)/Ag device. 67

5.1 A schematic diagram showing the cross-section of a typical ReRAM cell and the I-V measurement scheme. 73

5.2 (a) and (b) are FEG-SEM micrographs of the active layer of device C and device G, respectively. (c) is the EDS spectrum of device G (main graph) and device C (inset). Lastly, (d) is the magnified FEG-SEM micrograph of the MoS_2 agglomerate inside a PVP polymer. 74

5.3 I-V characteristics of (a) device C and (b) device G in semi-logarithmic scale. 75

5.4 The I-V characteristics of (a) device D, (b) device E, and (c) device F. 76

5.5 ln(I) versus ln(V) plots of device C, showing the entire forward and reverse sweep of the negative voltage bias (a) and the magnified graph of region ii. 78

5.6 ln(I) versus ln(V) plots of device G. 78

6.1 (a) the FEG-SEM micrograph and (b) AFM image of the active layer consisting of 1:1 chitosan to PVP ratio. 86

6.2 Current-voltage curves, showing different electroforming behaviour of the Al/chitosan+PVP/Ag devices consisting of 1:3(a), 1:1(b), and 3:1(c) chitosan to PVP. 88

6.3 Current-voltage characteristics of the Al/chitosan+PVP/Ag ReRAMs with 1:3 chitosan to PVP 88

6.4 Current-voltage characteristics of the Al/chitosan+PVP/Ag ReRAMs with 1:1 chitosan to PVP, showing the first sweeping cycle(a), the second(b), the third(c) and the 4th-24th cycles(d). 89

6.5 Current-voltage characteristics of the Al/chitosan+PVP/Ag ReRAMs with 3:1 chitosan to PVP. 90

6.6 Current-voltage curves, showing different electroforming behaviour of the ITO/chitosan+PVP/Ag devices consisting of 1:3(a), 1:1(b), and 3:1(c) chitosan to PVP. 91

6.7 Current-voltage characteristics of the ITO/chitosan+PVP/Ag ReRAMs with 1:3 chitosan to PVP. The inset shows the 5^{th} scan cycle with $I_{CC} = 0.005\ A$. 92

6.8 I-V graphs for the ITO/chitosan+PVP(1:3)/Ag device showing 1^{st} to 8^{th} voltage scans at increasing I_{CC}. The inset shows the 1^{st} and 2^{nd} cycles at 0.0001 A 92

6.9 Current-voltage characteristics of the ITO/chitosan+PVP/Ag ReRAMs with 1:1 chitosan to PVP.The inset shows the 3^{rd} scan cycle with $I_{CC} = 0.0005\ A$. 94

6.10 The I-V characteristics of the ITO/chitosan+PVP/Ag ReRAM with 1:1 chitosan to PVP ratio showing (a) the In—I—-In—V— curve fitting. (b) shows linear fitting of data for the first three consecutive scan cycles. 94

6.11 Current-voltage characteristics of the ITO/chitosan+PVP/Ag ReRAMs with 3:1 chitosan to PVP.The inset shows the 4^{th} scan cycle with $I_{CC} = 0.0005\ A$. 95

6.12 lnI againts lnV graph fitting of the Al/chitosan+PVP/Ag ReRAMs with 1:1 chitosan to PVP. This graph is a replot of Fig. 6.4c. 97

7.1 The main figure shows the schematic diagram of a typical PET-ITO/cow milk/Ag ReRAM device connected to a simplified current-voltage measurement circuit. The insets show (a) the actual photography of the PET-ITO/Cow milk(S2)/Ag ReRAM and (b) the cross-sectional FESEM micrograph of the S2 active layer. 102

7.2 EDS spectrum of typical cow milk. 102

7.3 FEG-SEM micrographs of (a) fat-free (S1), (c) medium cream (S2), and (e) full-cream (S3) cow milk films. On the same image, (b), (d) and (f) show the AFM topography images of the fat-free, medium cream and full cream cow milk, respectively. 104

7.4 I-V characteristics of the PET-ITO/cow milk(S1)/Ag device, showing (a) the forming curve, (b) the first and (c) the third sweeping cycle. 106

7.5 I-V characteristics of the PET-ITO/cow milk(S2)/Ag device, showing (a) the forming curve, (b) the first and (c) the first 30 sweeping cycles. 107

7.6 I-V characteristics of the PET-ITO/cow milk(S3)/Ag device, showing (a) the forming curve, (b) the first and (c) the first 80 sweeping cycles. (d), on the other hand, shows the resistance-number of sweeping cycle. 108

7.7 The I-V fitting (main figure) and lnI-lnV fitting (inset) of the PET-ITO/cow milk(S1)/Ag device. 110

7.8 The lnI-lnV fitting of the PET-ITO/cow milk(S2)/Ag device. 110

7.9 The I-V fitting (main figure) and InI-InV fitting (inset) of the PET-ITO/cow milk(S3)/Ag device. 111

List of Tables

1.1 Comparative summary of device characteristics mainstream and emerging memory[Yu2016]. 19

2.1 The summary of materials used in this study and their suppliers. 33

5.1 Details of the active layers of various devices and resistive switching characteristics. 80

7.1 The comparative summary of metallic element content from the EDS data, switching type, and conduction mechanism of fat-free, medium fat and full ream raw cow milk-based active layers. 114

7.2 Summary of important memory device parameters of some bare organic/biological material based ReRAMs.(CBCM-Conductive-bridge filament conduction mechanism.) 115

Chapter 1

Introduction

The use of information technology (IT) has been significantly increasing these recent years and more so during the current fourth industrial revolution (4IR). However, this increase in the use of technology is proportional to the rise in electronics waste (E-waste), as more electronic devices are discarded and replaced by their newer and advanced versions[1]. E-waste poses a threat to the environment and to human life due to heavy metals such as lead[1]. Therefore, high speed, low cost, and, more importantly, environmentally friendly devices are needed for the future green electronics world[2–4]. Memory devices are the heartbeat of the IT industry. They ensure that the data containing programs and files are stored and accessed conveniently and intact. Therefore, with the increasing demand and use of IT devices, memory devices must be improved to meet the required standards. Accordingly, the memory device industry must reduce its environmental footprint. In such an attempt, the memory industry is researching a new generation of nonvolatile random-access memories (RAM), called resistive switching memory (ReRAM). ReRAMs have the potential to replace conventional RAMs such as static random access memory (SRAM), dynamic random access memory (DRAM), and flash memory, which pose a threat to the environment by consuming high power and contain heavy metals. Furthermore, these recent memories have shown significant optimization limits. This thesis entails the study of electrical conduction and resistive switching in polymer and biodegradable nanocomposites.

1.1 Basics of memory devices

A memory device is a device that works to store data containing programs or information. A typical memory device consists of individual memory cells that are arranged to form a $2^N \times 2^M$ array of N rows and M columns, as shown in Fig. 1.1(a). Memory cells of the same memory device are identical, and they are connected to the same column called bitline (BL) and a common raw called wordline (WL). The WL and BL are connected to decoders that extract row address bits and column address bits, respectively[5–7]. Typically, each memory cell stores only one bit of data represented as a binary number (or codes) '1' or '0'. However, scientists have provided evidence of multilevel data storage where more than one bit of data is stored[8, 9]. A series of eight binary numbers is called a "byte" and describes just one letter, number or character. For example, the letter "A" is represented by the string "01000001", arranged according to the American Standard Code for Information Interchange (ASCII). There are two fundamental operations of any memory device, i.e., the "write" and the "read" operations. However, in some memories, such as DRAM, a third operation, i.e., the "refresh" operation, is also performed. During the "read" or "write" operations, the decoder activates the WL and the BL associated with the targeted memory cell[6]. The three essential memory parameters characterize these operations: the "write-access-time", i.e., the time-lapse between the "write" request and the final writing of the input data into the memory, the "read-access-time", i.e.,

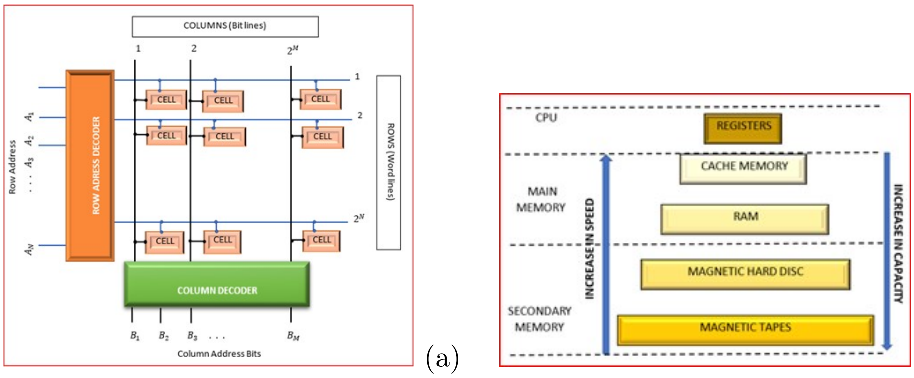

(a) (b)

Figure 1.1: The schematic diagram of (a) a typical memory device and (b) a typical memory hierarchy.

time-lapse between the "read" request and the moment the data is available, and the "read/write-cycle time", i.e., the minimum time required between successive "read/write" operations[7]. Figure 1.1(b) shows different categories of memory devices used to store information inside a computer. All these memories have different physical designs and working principles. The type of memory used to store data or applications depends on parameters such as memory size, read/write access times, access patterns, and system requirements[7]. The primary memory, also known as the main memory, constitute RAM and cache memory, while the secondary memory constitutes the hard disc drive (HHD) or solid-state drive (SSD). Other offline storage devices, such as, external hard drive, compact discs (CDs), thumb drive or universal serial bus (USB), and digital versatile discs (DVDs) are also often used as supplementary data storage. Random access memories, so-called because each memory cell can be accessed directly and independently store applications and data for programs in current use so that the processor quickly accesses them[10]. This is due to its fast speed and easy access to stored information. Usually, there are two RAMs in a computer; one is located in the central processing unit (CPU); this is called the cache memory. The other is located outside the CPU but in the computer chip.

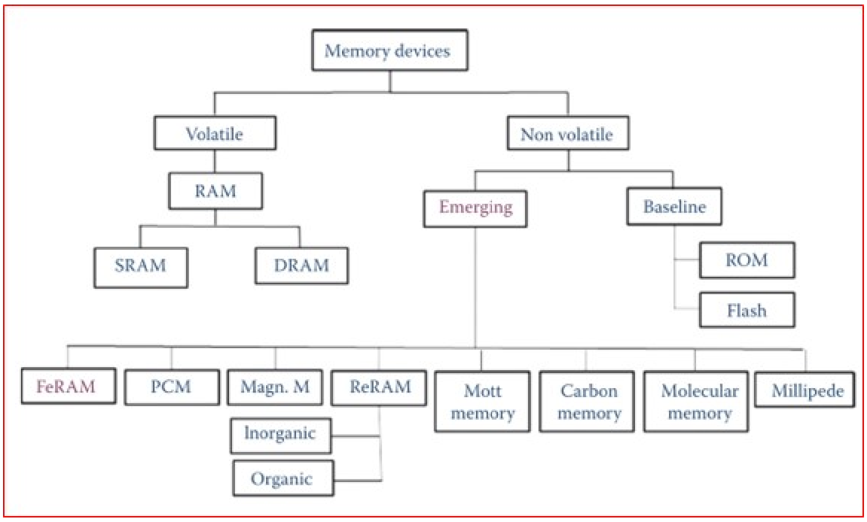

Figure 1.2: Classification of current and emerging memory devices [Vallabhapurapu2018a].

Cache RAMs are the fastest of the two RAMs; therefore, they store the data for an operating system, such as boot files. Static random-access memories (SRAM) are usually used as cache memory. Dynamic random-access memories (DRAM) are used as the primary RAM storing data for the currently running applications. All the data for the applications and files waiting to be accessed is kept in the secondary memory.

Different authors classify memory devices in different ways, depending on the individual's interest. However, we shall adopt the classification of memories as volatile and nonvolatile as used by Vallabhapurapu *et al.*[11], as shown in Fig. 1.2. Volatile memories (VMs) require a constant power supply to retain their stored data, such that, when power is interrupted, all stored data is lost. Nonvolatile memories (NVMs), on the other hand, keep their data even without any power supply.

1.1.1 Volatile memory

Static random-access memory (SRAM)

By definition, static memory refers to a memory device that retains data indefinitely[6]. However, SRAMs are classified as volatile memories because they only keep the stored data as long as the power is supplied and a slight interruption to the power results in loss of data. Figure 1.3 depicts a typical SRAM cell consisting of a bistable flip-flop circuit, consisting of four (M_1, M_2, M_3 and M_4) transistors plus either an additional two (M_5 and M_6) transistors, as shown in Fig. 1.3(a), or two polysilicon resistors (R) as pull-up devices, as shown in Fig. 1.3(b)[6, 12]. These cells have two stable states, which denote logic "1" and logic "0". These states represent a high potential at the ¯BL and low potential at BL, and vice versa. The first 64-bit metal-oxide-semiconductor (MOS) p-channel SRAM was developed in 1964 by an electrician John Schmidt at Fairchild Semiconductor, and the first SRAM chip, the 256-bit Intel 1101, was released by Intel in 1969. The common disadvantages of this cell are large cell size due to at least four transistors, structural complexity making SRAM expensive to build, high power consumption and the tendency to exhibit "latch-up" phenomena[6].

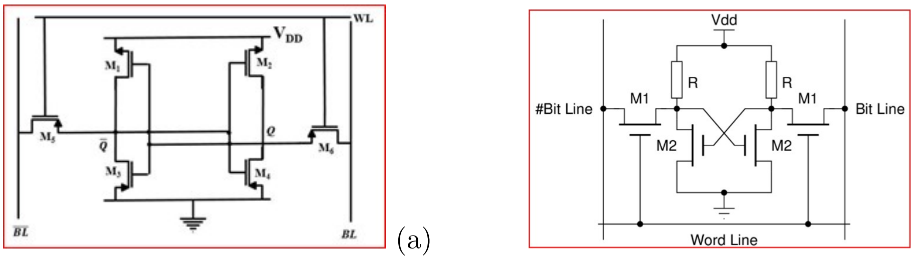

(a) (b)

Figure 1.3: schematic diagrams showing two designs of a 1-bit SRAM cell. Design (a) consists of four transistors plus two additional transistors, while design (b) consists of four transistors and two resistors [Aliakhmet2018].

Dynamic random-access memory (DRAM)

The dynamic random-access memory (DRAM) is the first solid-state-memory that was proposed in 1968 by Robert H. Dennard. DRAM became dominant due to its low energy consumption and simple architecture compared to its SRAM counterparts. Figure 1.4 shows the simplest DRAM architect, namely the $1T1C$ DRAM, consisting of one transistor and one capacitor connected in series[13]. To write data in a DRAM cell, a voltage V_{CC} representing the data is applied on the BL connected to the gate of the access transistor. This voltage charges the capacitor and when the capacitor is fully charged, the voltage on the wordline is removed, and the transistor is turned off[14]. The fully charged state of a capacitor represents the binary number "1," and the utterly uncharged state represents the binary number "0". DRAMs are volatile memories as the capacitor gradually loses the stored charge.

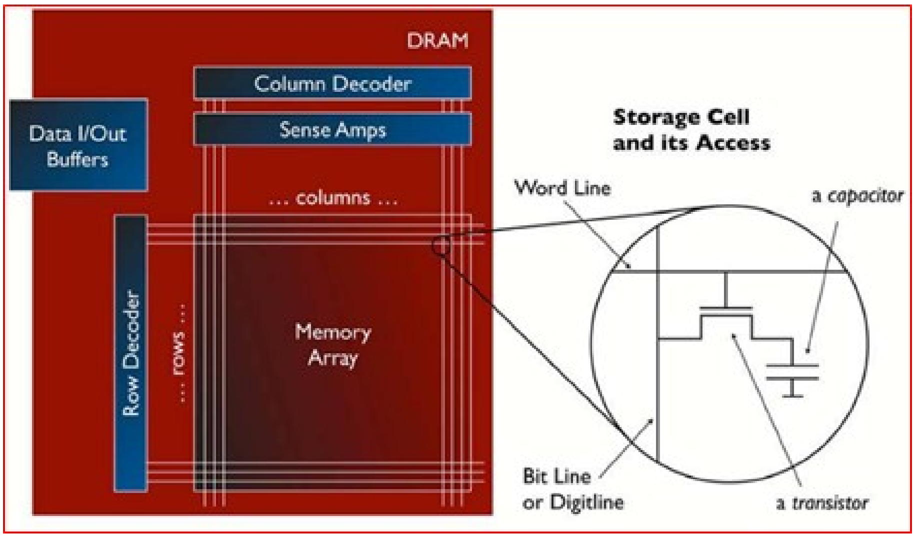

Figure 1.4: A schematic diagram shows a primary organization of DRAM internals, while the magnified image shows the 1T1C DRAM cell[Jacob2009].

To keep the integrity of the stored data, the capacitor must be frequently refreshed. Advancements have been made to the number of transistors in each cell; for example, three transistors can be installed to create a $3T1C$ (three-transistor-one-capacitor) DRAM. The 3T1C DRAM is faster than the 1T1C DRAM; however, the cell size is compromised by the addition of transistors. Other advancements can be made to the cell architecture to achieve an operating temperature of as high as 500 K[15]. Also, an improvement of 128× and 20× in capacity and access bandwidth, respectively, over the past two decades, have been achieved[16]. Tremendous improvement in DRAM technology, such as a successful decrease of stored charge, which results from reducing the operating voltage from about 12 V to as low as 3.3 V while the capacitance of the capacitor is still maintained in the range of 30 fF. DRAMs have also been researched for reliability at high temperatures[17], operating temperature[15], materials for the improved capacitor[18], reduced leakage currents[19], power consumption[20] and retention time[21]. However, there is always a limit to how small the capacitor can be. This scaling limit poses a significant threat to the compatibility of DRAMs, as modern devices are becoming smaller.

1.1.2 Nonvolatile memories (NVM)

Nonvolatile memories are memories that retain the stored data indefinitely even when power is off. NVMs exist primarily in the class of read-only memories (ROMs). We shall provide a moderate discussion of ROMs and other forms of NV RAMs in the following subsections.

Read-only memory (ROM)

Read-only memory (ROM) is fundamentally a type of memory that once it has been programmed, it is impossible to alter any stored data. Figure 1.5(a) depicts a typical REOM cell. Each cell consists of a single N-channel metal-oxide-semiconductor field-effect transistor (MOSFET) connected such that its source is connected to the bitline (BL), drain to the ground, and the gate connected or not connected to the wordline (WL). When the application of a voltage activates a WL, the presence/absence of contact between the gate and the WL causes different voltages (Low or High) at the bitline to be registered, which are translated as logics “0” or “1”[12]. ROMs are widely used to store data such as boot files for the operating system in computers, or systems’ operating programs, e.g., program code for vending machines. ROMs can be classified into non-programmable ROMs (NPROMs), one-time programmable ROMs (OT-PROM), and programmable ROMs (PROMs)[12]. Non-programmable ROMs are also referred to as Mask ROMs. Upon manufacturing, these ROMs are preloaded with data programmed by the chip manufacturer. Thus, they can only be read without any alteration. Programmable ROMs (PROMs), on the other hand, are initially empty; and this allows the user an opportunity to program the memory chip. Conventional PROM chips will enable the user to program the chip only once; no further alteration of data can be performed. Such PROMs are referred to as One-Time Programmable ROMs (OT-PROMs)[22]. With the advancements of technology, different successful attempts have been made to provide erasability and re-programmability in PROMs. Therefore, PROMs are recently converted into another class called erasable and programable ROMs (EPROMs) which allow the user to erase and re-program the memory chip a few times. EPROMs are classified into two categories based on the erasing stimulus, i.e., ultraviolet radiation EPROM (UV-EPROM) and electrically EPROM (EEPROM). UV-EPROM uses UV radiation to erase the memory chip. As such, a UV-EPROM chip is designed with a small window, which, when unsealed, allows UV radiation to enter the memory chip and thus erase the stored data. The disadvantages of UV-EPROM include: (1) the erasure

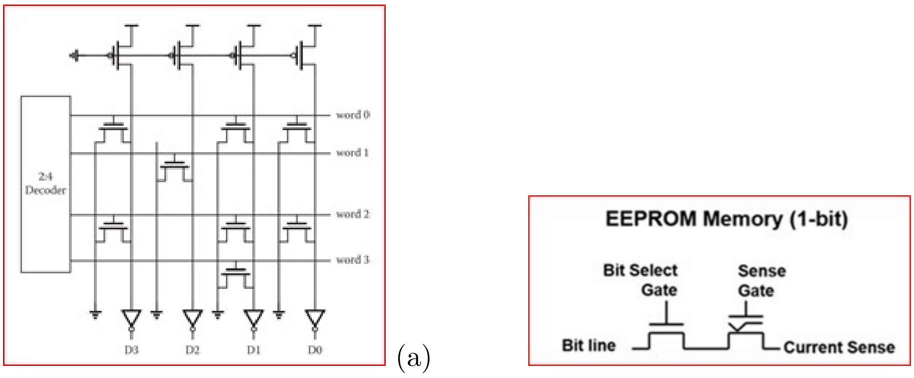

(a) (b)

Figure 1.5: (a) A schematic diagram of a typical ROM. Reprinted from [Li2012]. A schematic diagram showing a series connection of a MOSFET transistor and a floating gate transistor in an EEPROM cell (b).

operation protocol involves physically removing the memory chip from the module, then removing the window seal and leaving the chip under sunlight for UV-radiation exposure for some time. This is a long process, and it takes a long time, (2) the chip can only be erased once, and (3) the entire memory is erased, i.e., no bit erasure. The EEPROM technology addresses all the UV-EPROM shortcomings. EEPROM chip can be erased and written several times, and these operations are performed inside the device. In addition, the memory cells can be erased byte-wise[22]. Conventional EEPROMs design is shown in Fig. 1.5(b). They consist of two MOSFETs, one of which has an additional floating gate (FG). The floating gate transistor in EEPROMs is charged and discharged through the Nordheim-Fowler tunnelling (NFT) effect[23]. EEPROMs generally have a large chip size (because of the use of two transistors), are low-density, and require a large voltage to perform the write and erase operations.

Flash memory

Flash memory is, by definition, an EEPROM. However, Flash memory addresses some of the underlying issues facing conventional EEPROMs, such as speed and large memory cell size. Figure 1.6(a and b) show a cross-sectional area of a typical flash cell and its symbol, respectively. Flash memory uses only one transistor and thus has a smaller chip size compared to the ordinary EEPROM. This structural simplicity allows for more memory cells per unit area, thus providing more density and compatibility for many applications. In addition, flash memories applications are outspread to removable portable devices such as digital storage for digital photographic devices, e.g., SmartMedia cards, memory sticks, embedded storage for cellular phones, MP3 players/iPod, and solid-state drives (SSDs)[24]. The first Flash memory idea was proposed in 1977 by Jack Huang[25]. In 1987 the first NAND flash memory chip was developed at the Toshiba Corporation[26]. In 1988, Intel Corp developed the first commercial NOR Flash memory[27]. Flash memory chips largely dominated the electronics industry in the 1990s in Flash memory cards and a significant component of nonvolatile solid-state drives (SSD's).

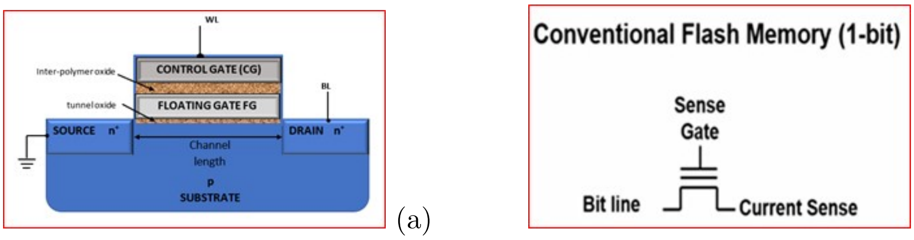

(a) (b)

Figure 1.6: A cross-sectional area of a typical flesh memory (a) and a 1-bit flash memory cell symbol (b).

Flash memories architect involves a structural modification of a transistor by introducing a layer of material capable of trapping charge. This material is called the floating gate (FG) because it cannot be accessed electrically. The FG and the control gate (CG) are separated by a thin oxide layer, i.e., interpolymer oxide and tunnel oxide. A cross-sectional area of a flash memory cell is shown in Fig. 1.6(a). The CG is connected to the wordline (WL), which is used to activate each cell, while the drain is connected to the bitline (BL), which in the end, is connected to the power source. All the source terminals are connected to the ground[28]. Silicon-based flash memories have two classes: the NOR flash memory and the NAND Flash memory (see Fig. 1.7).

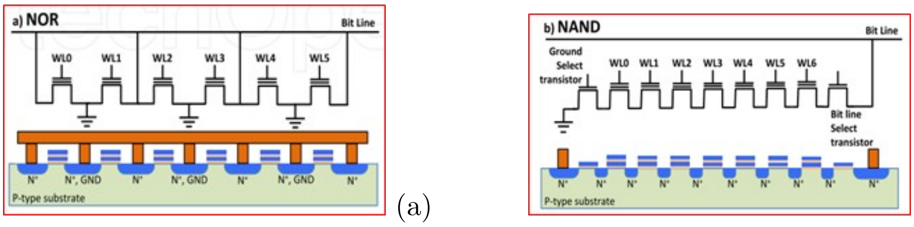

(a) (b)

Figure 1.7: Schematic diagrams showing (a) NOR and (b) NAND Flash memory arrays. Reprinted from [Autran2014].

The NOR Flash memories have low density, large cell size but high speed compared to NAND Flash. They provide random access to each cell; therefore, they are used as RAMs. On the other hand, NAND-Flash memories have a relatively small cell size and low speed; however, they have high memory density. They provide chronological access to the stored memory; therefore, they are being used as a solid-state drive (SSD), replacing magnetic discs in modern computers' hard drives[11]. The cell size of NAND is about $4F^2$, whereas the NOR has about $10F^2$; where F is the design rule of a chip called the minimum feature size[27]. The floating gate transistor can take on two states, i.e., the charged state and the no-charge state. These states represent the binary code "1" or "0", which represents 1-bit per cell of data. In NAND-flash, increasing the charge stored or the threshold voltage (V_t) results to increase in the bits-per cell. For example, according to Micheloni *et al.*[27] “Two bits per cell (MLC) storage is enabled by increasing the number of V_t levels to four representing 11, 10, 01 and 00. Similarly by increasing the number of voltage threshold levels to eight and 16, 3-bit per cell and 4-bit per cell storage is enabled”, this is called multi-level cell (MLC) storage[27]. However, MLC results in degradation of endurance, retention, and write performance[27]. Other challenges faced by the Flash memory include scalability challenges associated with limitation in the reduction of the transistor size, therefore preventing the cell size from becoming smaller; the power needed to write to Flash is also a limitation that affects the battery life in portable devices. High write voltage, low write speed are also a challenge. Also, generally, the performance of Flash memories can be affected by the interaction of electrons stored on one transistor interacting with an adjacent cell[11].

1.2 Prototypical memories

1.2.1 Ferroelectric Random-Access Memory (FeRAM)

Ferroelectric random-access memories (FeRAMs) utilize a ferroelectric material sandwiched between two electrodes. When a strong electric field (E) exceeding the coercive field (E_c) is applied at the electrodes, the polarization of the ferroelectric material changes due to the ferroelectric effect phenomenon[22]. FeRAM cell architecture is analogous to DRAM cells, except that in FeRAM, the ferroelectric layer replaces the silicon dioxide layer[11]. FeRAMs retain their polarization states without the need constant power supply, making FeRAM nonvolatile memories. FeRAMs have advantages such as low power consumption compared to flash memories, high speed read/write ($< 50\ ns$), high switching endurance ($\geq 10^{13}$), mak-

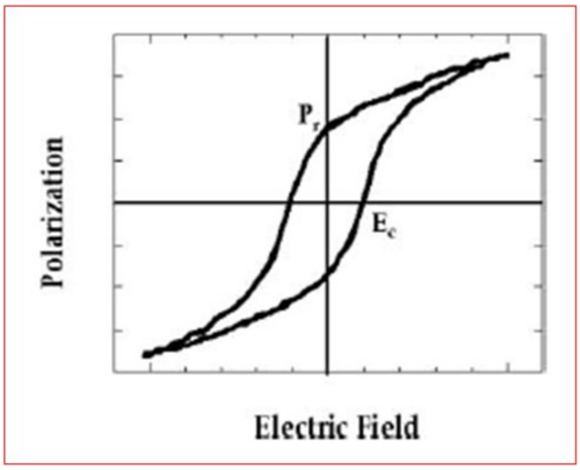

Figure 1.8: A schematic diagram showing a hysteresis loop in polarization versus electric field for a ferroelectric film. Reprinted from [Eshita2014].

ing them applicable in smartcards and identification tags[29]. The most common FeRAM materials are the perovskite structures, typified by the $(PbZr_xTi_{(1-x)}O_3$ (PZT), and layered structure, typified by either strontium-bismuth-tantalite $(Sr_{(1-y)}Bi_{(2-x)}Ta_2O_9$ (SBT) or lanthanum substituted-bismuth-titanite $Bi_{(4-x)}La_xTi_3O_{12}$ (BLT)[30]. A typical polarization versus electric field (P-E) hysteresis loop for a ferroelectric film is given in Fig. 1.8. The parameters P_r and E_C are respectively, the remnant polarization (the value of P at $E = 0$) and the coercive field (the reverse field needed to bring the polarization to zero). Just like DRAMs, FeRAM suffer scalability challenges which limits their applicability in future electronic devices

1.2.2 Phase change random access memory (PCRAM)

Phase-change RAMs utilize a material capable of having two resistive states, i.e., a high resistive state (HRS) and a low resistive state (LRS). The unique thing about the PCRAMs is that these resistive states are associated with material phases. Therefore, phase change materials can undergo a reversible

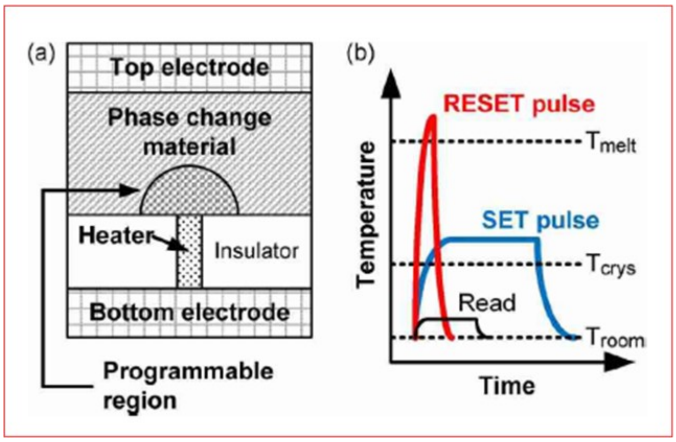

Figure 1.9: A schematic diagram showing (a) the basic design of a phase change memory cell and (b) the temperature versus time for a conventional PRAM. Reprinted from [Wong2010].

structural transition between the crystalline and amorphous forms. The crystalline state has low resistivity (LRS), and the amorphous state has high resistivity (HRS)[31]. The first observation of this phenomenon was made in 1968 by Stanford R. Ovshinsky[32]. This behaviour is observed mainly in chalcogenide glass, which has an amorphous ground state and contains group VI elements such as, S, Se, and Te[11]. The structural phase change may also be accompanied with a change in optical properties, such as reflectance in some materials, for example, $Ge_2Sb_2Te_5$ (GST). This reversible change in reflectance has been exploited for years in storing information in optical discs such as rewritable CDs and DVDs[11]. In the context of RAM fabrication, change in the resistive state can be used, not reflectance. The resistive change in PCRAM is induced by either Joule heating or laser heating[33]. A schematic diagram of a PCRAM is shown in Fig. 1.9(a). The phase change material is initially in the crystalline phase, and the semicircular region in Fig. 1.9(a) represents the programmable region made of a phase change material. During the RESET process, i.e., change from LRS-to-HRS, a large- but short-duration current pulse is applied to the heater;

this melts the programmable layer and leaves it in the amorphous state of high resistance. Because this programmable region in the amorphous state is in series with any phase change material area, the entire cell is in the HRS. Similarly, a medium electric current is applied to anneal the programmable region at a temperature between the crystallization temperature and the melting temperature until crystallization is complete[34]; this induces the SET process (change from HRS-to-LRS). Figure 1.9(b) shows a temperature versus time graph depicting the "RESET" and "SET" processes. The shortcoming of PRAM is that even though the filament size can be reduced, there is a limit to how small the 'mushroom', i.e., the phase change area, can be, thus limiting the cell size.

1.2.3 Magnetic random-access memories (MRAMs)

Magnetic memories are classified into three main types, i.e., Magnetoresistive random-access memory (MRAM), spin-transfer torque random-access memory (STT-RAM), and racetrack memory. MRAMs are developed based on the magnetic tunnelling junction (MTJ) made with two ferromagnetic (FM) layers separated by a thin barrier made by an insulator, with an architecture composed of one transistor and one resistor (1T1R). According to the quantum tunnelling theory, an electric current flows between the two FM layers and tunnels through the junction. The magnitude of the tunnel current depends on the magnetisation's relative orientation in the two FM layers[11]. Such that when the magnetization in the two FM layers is aligned parallel, the device is in the low-resistive state (LRS), denoted as R_p, and the high resistive (HRS) state is achieved with the antiparallel alignment, denoted as R_{ap}. The tunneling magneto-resistance (TMR) is the given as:

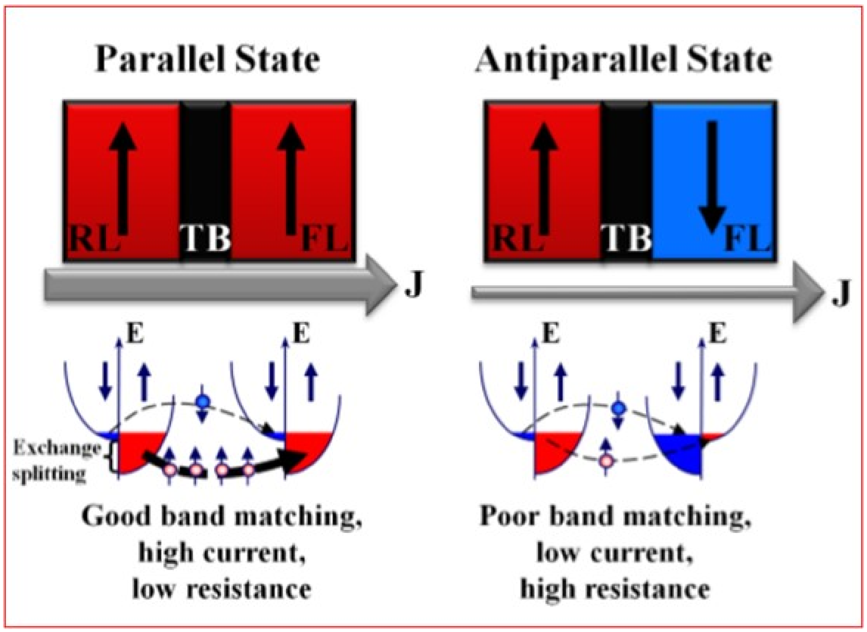

Figure 1.10: A schematic diagram showing the low and high resistive states for an MTJ MRAM. Reprinted form [Apalkov2016].

$$\frac{\Delta R}{R} = \frac{R_{ap} - R_p}{R_p} \tag{1.1}$$

The commercial success of MRAMs has been hindered by their limited memory density of not more than 4 $Mbit$[35]. Figure 1.10 shows a schematic diagram for a magnetic tunnelling junction (MTJ) MRAM, with ferromagnetic layers (red), e.g., CoFe based alloy; and the tannel barrier (blak), e.g., MgO of about 1 nm thick. One can see that when the magnetization (shown by the arrows) in the RL (reference layer) and the FL (free layer) are parallel, the high current pass through the TB (tunnel barrier), signifying a low resistive state (LRS); and when the magnetization is anti-parallel, low current pass, meaning a high resistive state (HRS)[36].

1.2.4 Resistive switching memory (ReRAM)

ReRAM basics

Resistive switching memories (ReRAMs) are emerging capacitor-like NVMs which uses a resistive switching material sandwiched between two electrodes, i.e., a top electrode (TE) and a bottom electrode (BE)[37]. In the early 1960s, Hickmott first observed the resistive switching phenomenon in metal oxide film[38]. Hickmott observed that the application of voltage stress caused a reversible change in the resistance of a metal-oxide-metal system[38]. Currently, this phenomenon has become the operating principle in ReRAMs. Figure 1.11 is a schematic diagram depicting the basic design of a single ReRAM cell. Unlike other memories, a ReRAM does not require a driving transistor; thus, ReRAM modules have a scaling advantage. Each ReRAM cell takes on two distinct resistive states, i.e., a high resistive state (HRS) called the "OFF" state and a low resistive state (LRS) called the "ON" state. An externally applied electric field is used to cause a resistive switch from HRS to LRS during the "SET" or "write" operation, and LRS to the HRS, during the "RESET" or "erase" operation[39]. These two resistive states resemble the logic "0" and "1"[40]. An as-fabricated ReRAM cell is in a very high resistance state associated with the insulating state of the active layer[37]. A strong voltage applied at the electrodes may

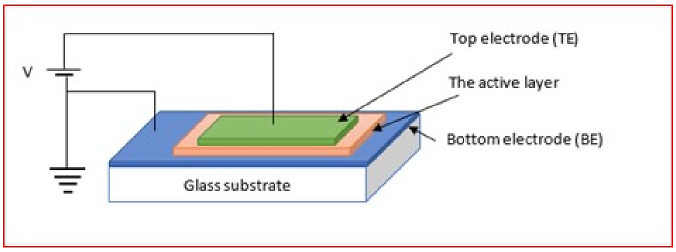

Figure 1.11: A diagram showing a basic design of a ReRAM cell

result in a drastic decrease in resistance called the electroforming or simply 'forming' process[41]. The application of a threshold voltage, V_{RESET} takes the cell back to the HRS having a resistance comparably lower than of the as-fabricated sample. After the forming operation is performed, the as-fabricated resistive state is not regained, and the cell remains in the new state called the as-electroformed state[42]. ReRAMs retain their ON- and OFF-states even when the power is withdrawn, making them candidates for NVM. Additionally, suppose the switching is repeatable for many cycles. In that case, the device can be used to create a RAM, and if the device is switchable only once, it can be used as a write-once read many times memory (WORM). ReRAMs draw their appeal from their high density (comparable to the DRAM), high speed (relative to the SRAM), and architecture simplicity which does not involve the use of a transistor[11]. Their newest integration of organic and organic-inorganic hybrid active layers[43] adds biodegradability and compatibility with flexible electronics. ReRAMs also have excellent compatibility with complementary metal-oxide-

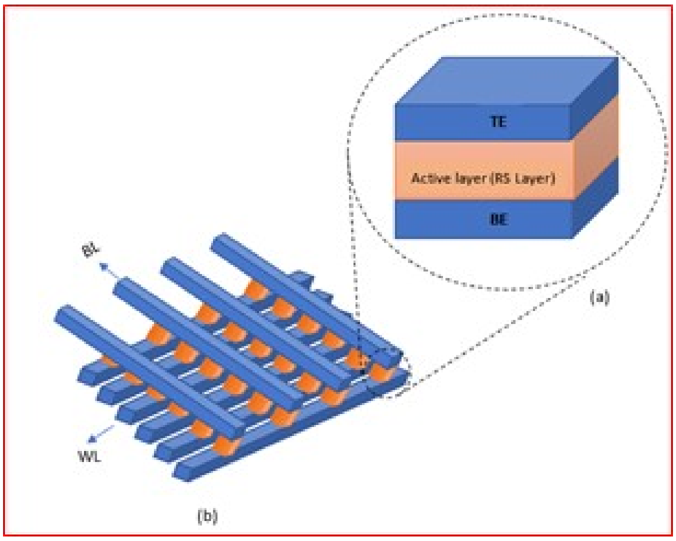

Figure 1.12: A basic schematic diagram of a typical ReRAM (a) cell and (b) a configuration of a crossbar array of a ReRAM memory.

Table 1.1: Comparative summary of device characteristics mainstream and emerging memory[Yu2016].

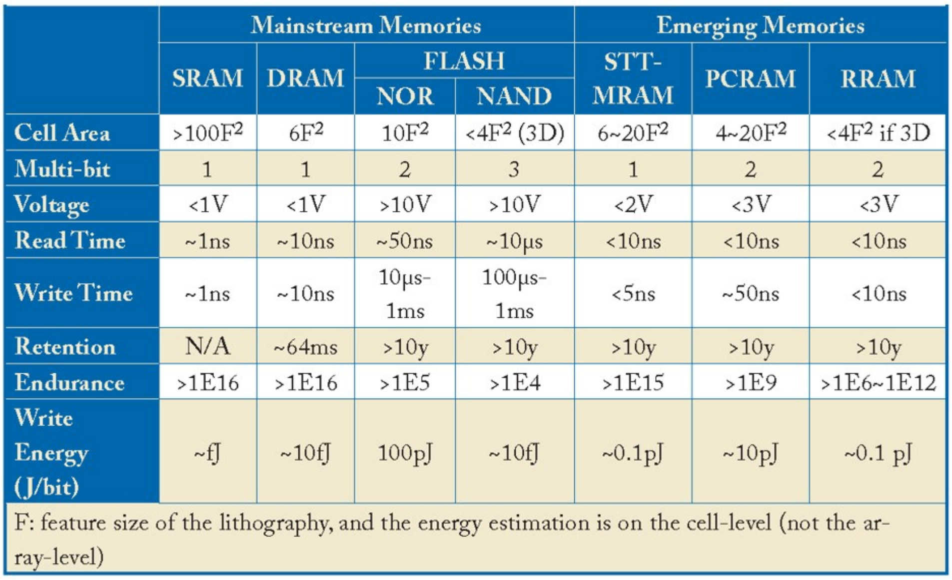

	Mainstream Memories				Emerging Memories		
	SRAM	DRAM	FLASH		STT-MRAM	PCRAM	RRAM
			NOR	NAND			
Cell Area	>100F^2	6F^2	10F^2	<4F^2 (3D)	6~20F^2	4~20F^2	<4F^2 if 3D
Multi-bit	1	1	2	3	1	2	2
Voltage	<1V	<1V	>10V	>10V	<2V	<3V	<3V
Read Time	~1ns	~10ns	~50ns	~10μs	<10ns	<10ns	<10ns
Write Time	~1ns	~10ns	10μs-1ms	100μs-1ms	<5ns	~50ns	<10ns
Retention	N/A	~64ms	>10y	>10y	>10y	>10y	>10y
Endurance	>1E16	>1E16	>1E5	>1E4	>1E15	>1E9	>1E6~1E12
Write Energy (J/bit)	~fJ	~10fJ	100pJ	~10fJ	~0.1pJ	~10pJ	~0.1 pJ

F: feature size of the lithography, and the energy estimation is on the cell-level (not the array-level)

semiconductor (CMOS) processes, which allows for more applicability and mass production[40]. The crossbar array (Fig. 1.12b) which comes with excellent individual cell miniaturization potential down to $4F^2$, even further to $4F^2/n$ with vertical (3D) architecture (F is the minimum feature size, and n is the stalking layer number) is an added advantage for the practical applicability of ReRAMs[39]. Table 1.1 shows the device characteristics of ReRAMs and other memories.

Classification of resistive switching modes

The current-voltage (I-V) characteristics of different ReRAM systems can be classified into two, i.e., (1) unipolar RS, where the voltages, V_{SET} and V_{RESET} have the same polarity but different magnitudes, and (2) bipolar RS, where V_{SET} and V_{RESET} have opposite polarities, see Fig. 1.13. Asymmetric device structures, i.e., where the TE and the BE are of different

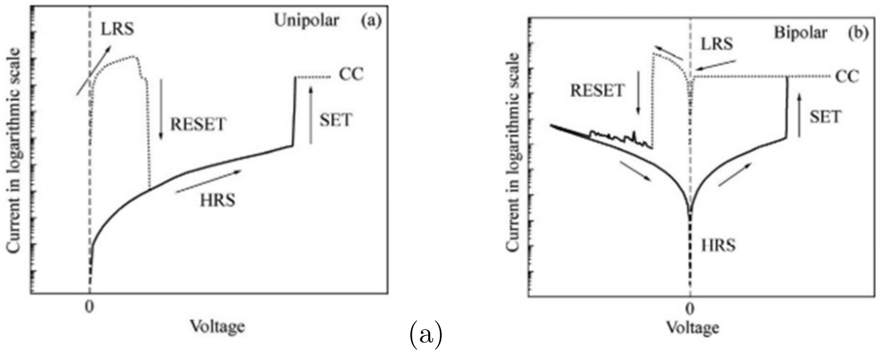

(a) (b)

Figure 1.13: Schematic diagrams showing dc current-voltage relationship for unipolar (a) and bipolar RS modes (b)[Pan2010a].

materials, are likely to have a bipolar RS mode. On the other hand, the symmetric devices are likely to have a unipolar RS mode[44]. Therefore, the electrode material significantly impacts the ReRAM switching mechanism and switching mode[39]. The I-V hysteresis for the bipolar RS mode can be classified into three types, i.e., O-type, N-type and S-type RS modes. The O-type RS mode is characterized by smooth homogeneous transitions from HRS to LRS, as shown in Fig. 1.14(a). O-type RS is sometimes referred to as analog, and others refer to it as interfacial RS. On the other hand, the N-type and S-type RS modes are considered digital memories. Figure 1.14(b) shows a typical N-type RS. This switching mode is characterized by a sudden increase in current happening at threshold voltage (V_t) during the SET, and a sudden decrease in current during the RESET process. The S-type switching mode is characterized by a sudden jump and a sudden drop in current happening at V_{SET} and V_{RESET}. If the RESET transition is happening at 0 V, a symmetric S-type RS is obtained, as shown in Fig. 1.14(c), while in asymmetric S-type RS the VSET and VRESET have opposite polarities as shown in Fig. 1.14(d)[45].

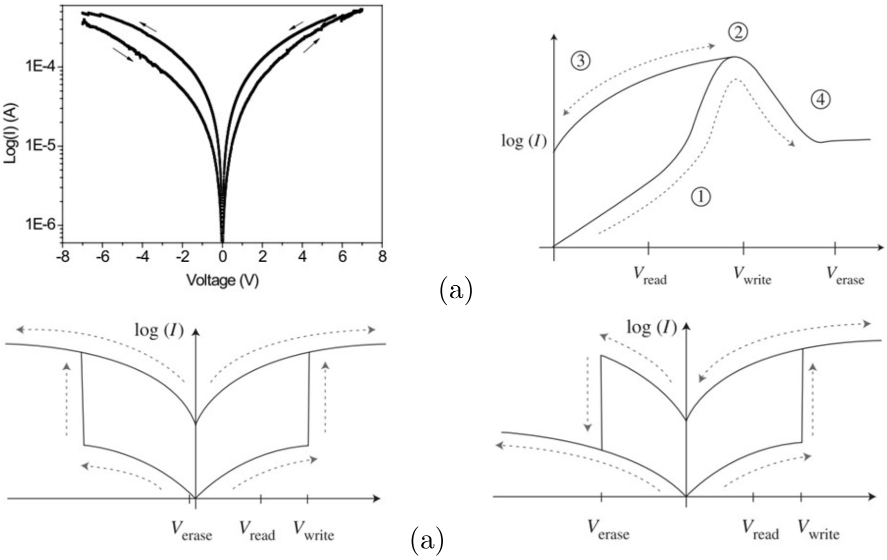

(a) (b)

(a) (b)

Figure 1.14: I-V hysteresis showing O-type RS mode[48], (b) N-type, as well as (c) symmetric and asymmetric S-type RS modes (d)[Prime2009]

Mechanisms of resistive switching

Understanding the resistive switching phenomenon is an important step towards the commercialization of ReRAMs. Currently, there is no consensus understanding of the exact origin of RS due to its random nature. That is, different switching mechanisms drive unipolar or bipolar switching modes. The I-V hysteresis in any mode usually follows the Ohmic (linear) relationship in LRS, and in the HRS, however, it usually follows one of the following relationships: (i) the Poole-Frenkel emission), (ii) the Schottky emission) or (iii) the space charge limited currents (SCLC), i.e., the Ohmic relationship in the low voltage regime, followed by the Child's square law in the high voltage regime[41]. These electrical conduction are facilitated by either the formation and rapture of a conduction filament, i.e., conduction filament dependent mechanism, or charge trapping, i.e., non-filament/interface conduction mechanism[46, 47]. CF and interfacial mechanisms manifest them-

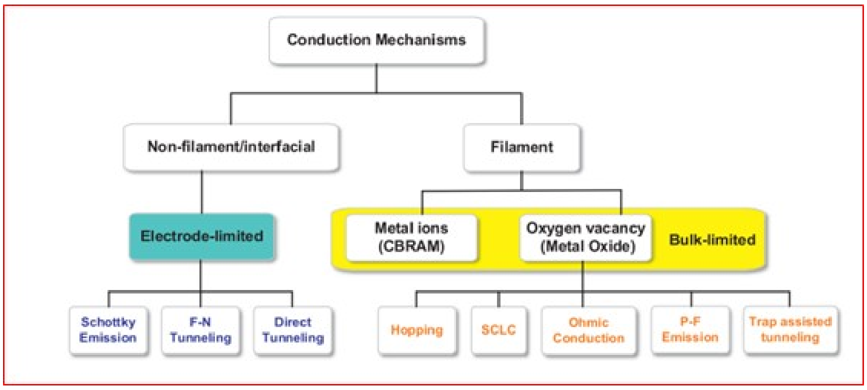

Figure 1.15: Classification of resistive switching mechanisms. Reprinted from[Wang2018a].

selves based on the resistance dependence on the cell size, i.e., in the CF mechanism, the HRS has no cell-size-dependence, whereas, in interfacial resistive switching, the HRS has a strong dependence on the size of the cell. Figure 1.15 shows the classification of conduction mechanisms into filament and non-filament. We shall provide a brief discussion of these classes of mechanisms in the next subsection.

Filament mechanisms

During the "forming process," a large voltage is applied to the cell. This voltage is so large that it induces a soft breaking of the dielectric (the insulating or semiconducting layer between the electrodes), leading to the formation of conduction filament (s) (CF), which short-circuits the cell and bring it to LRS. The application of voltages, V_{RESET} and V_{SET}, induce the rupture and reformation of the CF taking the cell to the HRS and LRS, respectively[48–50], as illustrated in Fig. 1.16. Thermal redox and/or anodization near the interface between the metal electrode and the oxide is extensively considered to be the mechanism behind the formation and rup-

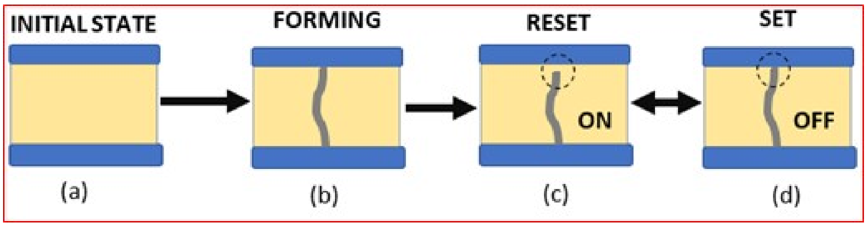

Figure 1.16: A schematic diagram showing a series of events in a filament type conduction mechanism. (a) a fresh sample, (b) the presence of a conduction filament after the forming process, (c), and (d) the partial rupture and reformation of the conduction filament, respectively.

ture of the filaments in unipolar systems. In contrast, the electrochemical migration of oxygen ions is the driving mechanism for bipolar switching[37]. Therefore, there are two types CF-ReRAMs: redox reaction induced metallic filament, i.e., electrochemical metallization (ECM) cell (also known as conduction bridging (CB) cell or programmable metallization cell (PMC)), and oxygen ions defects (V_O^{2+}) composed conduction filaments[44]. Conduction bridge ReRAMs (CBRAMs) generally consist of an electrochemically active electrode, e.g., Ag or Cu, and an inert electrode, e.g., Pt, Au or W. When a positive voltage is applied to the electrochemically active electrode and a negative voltage to the inert electrode, the active electrode is oxidized at the interface. The oxidation of the electrode can be represented as

$$A(s) \rightarrow A^{z+}(aq) + ze^- \tag{1.2}$$

(A and A^{z+}(aq) represent the metal atom and cation, respectively). The A^{z+} ions migrate through the RS layer towards the cathode (inert) electrode where they become reduced, i.e.,

$$A^{z+}(aq) + ze^- \rightarrow A(s), \tag{1.3}$$

as shown in Fig. 1.17. The deposition of A(s) atoms on the surface of the inert electrode result in the formation of a pile of A atoms, which

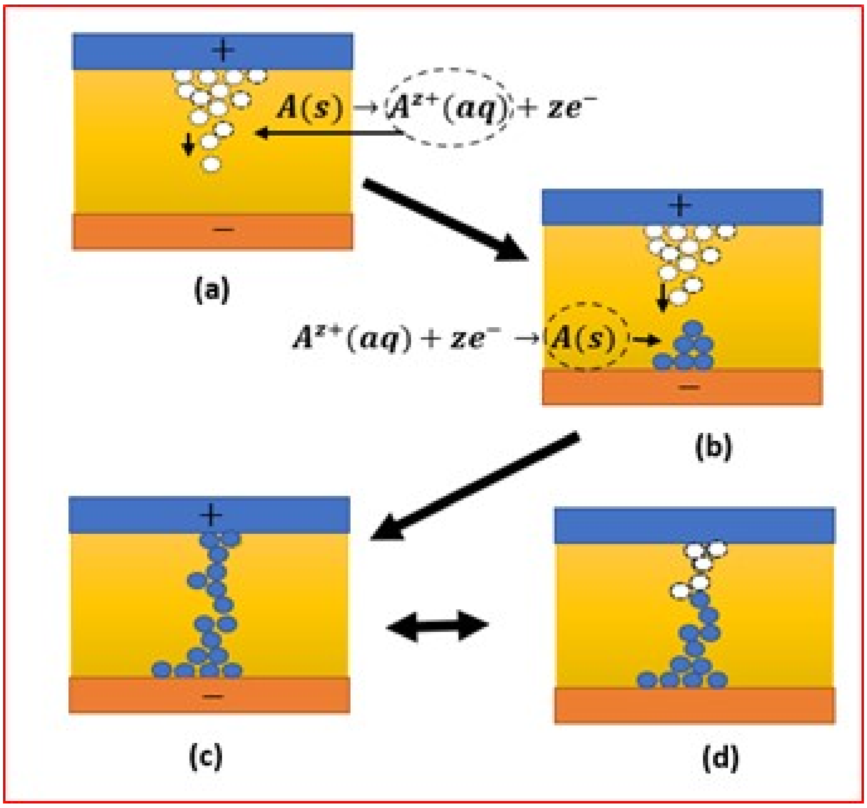

Figure 1.17: Formation and rapture of conduction filaments using oxidation and reduction of the electrodes.

grows towards the electrically active electrode, thus forming a CF. These CF can be dissolved by applying a voltage of opposite polarity, i.e., a negative voltage to the electroactive electrode and a positive voltage to the inert electrode, in bipolar mode, or by melting of its thin parts through Joule heating, in unipolar.

In metal oxides ReRAMs, the application of a positive voltage ($V_{FORMING}$) causes the oxygen (O^{2-}) to break off from their lattice, leaving behind an oxygen vacancy (V_O^-). These oxygen ions migrate towards the positive electrode, where they become oxidized to form oxygen atoms, i.e.,

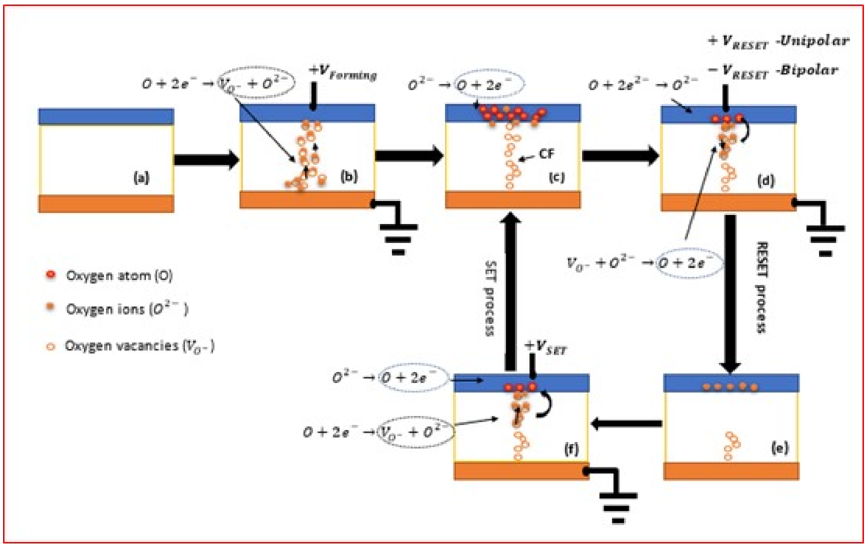

Figure 1.18: A schematic diagram showing the formation of virtual CF using oxygen vacancies.

$$O^{2-} \rightarrow O + 2e^-, \tag{1.4}$$

see Figure 1.18. This leaves behind vacancy formed CF in the metal oxide (MO) layer, which puts the cell in the LRS. The application of $-V_{RESET}$ (bipolar) results to reduction of the oxygen atoms back to O^{2-} ions, i.e.,

$$O + 2e^- \rightarrow O^{2-}, \tag{1.5}$$

Which are driven back to fill the vacancies resulting in the rupture of the CF. In the case of the unipolar mode, a $+V_{RESET}$ results to Joule heating resulting in thermally activated O^{2-} diffusion around the CF due to the concentration gradient, resulting in the rupture of the filament.

Nonfilament (or interfacial) mechanism

Non-filament/interfacial conduction is classified into three mechanisms, i.e., the Schottky emission, the Fowler-Nordheim (F-N) tunnelling, and the direct tunnelling mechanism. These mechanisms depend on the electrode characteristics, such as the energy barrier height between the electrode and the active layer (e.g., the metal oxide layer) interface. In addition, several models have been proposed for the driving mechanism in resistive switching involving an interface-type conducting path, such as electrochemical migration of oxygen vacancies, trapping of charge carriers (hole or electron), and a Mott transition induced by carriers doped at the interface.

1.2.5 Materials for ReRAM devices

Various materials, i.e., oxides, chalcogenides, carbon-based, and others, have shown resistive switching[23]. However, resistive switching materials are categorized mainly as inorganic and organic materials[51].

Inorganic ReRAMs

Inorganic ReRAMs can be dated as far back as the 1960s[38]. This makes inorganic ReRAMs the most studied class of ReRAM systems. Loosely, we can classify the inorganic film as binary and ternary oxides[52]. The first binary oxide to show resistive switching was the TiO. The well known binary oxides functional materials are SiO_x, TiO_x, NiO_x, TaO_x and HfO_x, while ternary oxides are $SrTiO_3$, $La_{0.7}Sr_{0.3}MnO_3$, $BiFeO_3$, chalcogenides, such as Ag_2S, Ge_xSe_y, nitrides such as, AlN and SiN, and many more[46]. Generally, all inorganic ReRAMs show superior properties. Generally, the switching in inorganic ReRAMs is facilitated by the rupture and reformation of conducting filaments[39]. Findings show that binary oxides typically have excellent ReRAM properties compared to the other members of inorganic ReRAMs[46]. Hafnium dioxide (HfO_2), however, shows to be the most promising properties for commercial RAMs, as it shows great scalability down to 10 $nm \times 10$ nm, large (10^9 cycles) endurance, nanoseconds switching speed, as well as low ($\sim$ 0.1 pJ) power consumption accompanied with compatible to complementary metal-oxide semiconductor (CMOS)[49, 51, 52].

Organic ReRAMs

Resistive switching in organic material is important for the environment. Organic ReRAMs are biodegradable and fabrication cost-effective. Organic ReRAMs offer high mechanical flexibility suitable for foldable and wearable electronics[39, 49], as shown in Fig. 1.19. Resistive switching memory based on polymeric materials was first discovered in the 1970s[53]. Since then many polymers and organic materials such as aloe vera[54], chitosan[55], pectin[56], protein[57], eggshell[47], egg albumen[47], graphene oxide[43], gelatine[58], and others have been used as active layers in organic ReRAMs. Figure 1.20 shows the classification of biodegradable materials for ReRAMs[50]. Organic ReRAMs have shown promising properties. However, it is noteworthy that no one material has shown all the optimal properties needed for commercial memory. Research has shown that high ($> 5 \times 10^9$) ON/OFF ratio, fast (< 5 ns) operating speed and high ($> 7.2 \times 10^7$ cycles) endurance have been shown in Poly(9-vinyl carbazole)(PVK), graphene oxide and Rose Bengal, respectively[46]. Research is underway to discover an organic ReRAM that will show all these properties. Ooi *et al.*[59] replaced metallic electrodes with flexible inorganic polymer polymethylsilsesquioxane (PMSSQ) in a graphene quantum dots organic ReRAMs. This resulted in

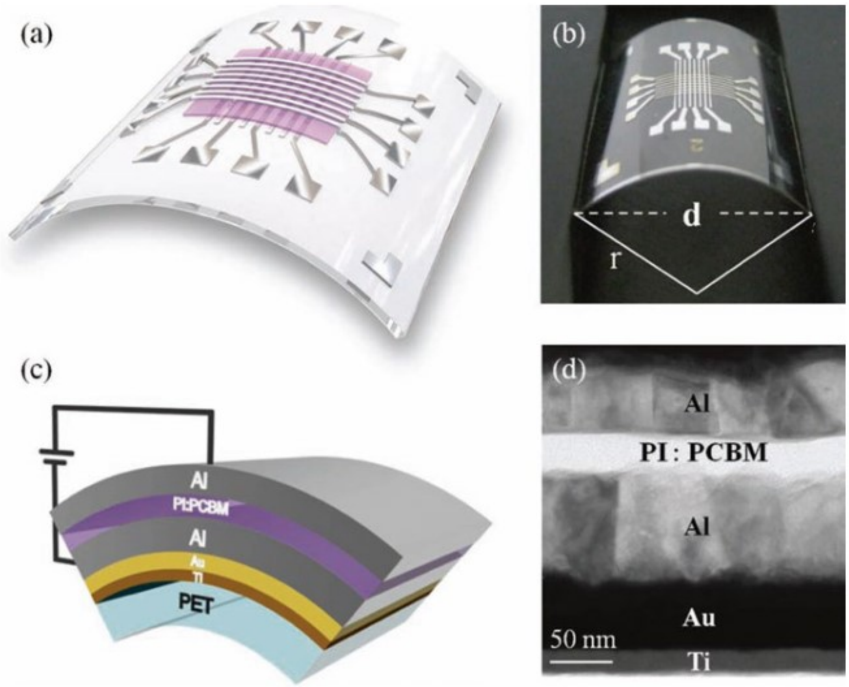

Figure 1.19: This image shows an 8 × 8 array Ti/Au/Al/Pi: PCBM/Al flexible organic memory. (a) a schematic and (b) optical images. (c) and (d) respectively show the schematic diagram and the SEM micrograph of the cross-section of the device. This image is taken from[Ouyang2016].

a device with increased flexibility, high (10^4) ON/OFF ratio, as well as a high 10^4 retention time. Apart from flexibility, organic ReRAMs have also shown transient properties. Ji *et al.*[60] reported a total transient ReRAM device that uses silk fibroin sandwiched between tungsten and magnesium electrodes. Transient memory devices are good for biomedical devices. In addition to mechanical properties of organic material-based ReRAMs, Qin *et al.*[61] reperted voltage induced multilevel switching in DNA molecule based device which uses Au electrodes. Multilevel switching is important multibit data storage. Even though the mechanism of resistive switching in ReRAMs is still a research topic, most organic ReRAMs have shown filament mechanism, driven by either electrochemical metallization (ECM)[60] or space-charge limited conduction (SCLC)[50, 59, 60] and can be fabricated with two-terminal or three-terminal configurations[11].

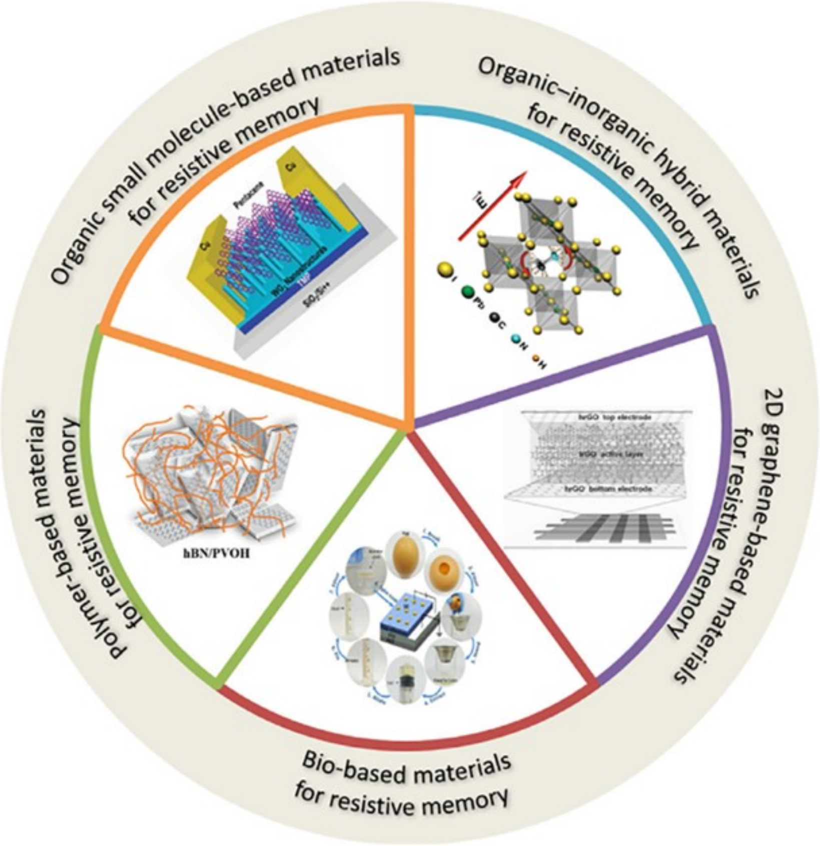

Figure 1.20: The classification of organic materials for ReRAM active layers. This image is taken from[Li2020].

1.3 Identification of research problem

1.3.1 Problem statement

The performance of any modern computer depends on its ability to access and run applications at a convenient speed. Memory devices are role players in storing (writing) and giving (reading) access to these applications. Memory devices used in modern computers include static random-access memory (SRAM), dynamic random-access (DRAM), and Flash memories. SRAMs are used for their high speed, up to 100 ns and low power consumption; DRAMs for their high density, and Flash for their nonvolatility, therefore suitable for use as SSD. All these memory devices have inevitable limitations, i.e., large cell size ($50 - 120\ F^2$) of SRAM, accompanied by current leakage; high operating voltages of 3 V and up to 6 V for DRAM and NOR Flash respectively; DRAM capacity needs to sustain enough charges (there is a limit to how small the DRAM capacity can be) and Flash need novel array structure. There is a demand for a next-generation RAM with fast read and write speed of SRAM, density and cost-benefit of DRAM, nonvolatility of Flash and unlimited endurance.

1.3.2 Aim/Purpose of the study

This research aims to conduct an intensive study of electrical conduction and resistive switching in various systems fabricated from biodegradable polymers and polymer composites. These systems are characterised and tested for their candidacy biodegradable resistive switching random-access memory (ReRAM).

1.3.3 Research objectives

The main objectives for this work were to:

- understand the electrical conduction mechanism in different organic polymers and their composites.
- optimize and obtain the best resistive switching memory parameters

in various organic polymers and nanocomposites.

- develop a resistive switching random access memory devices using biodegradable materials.
- develop understanding of resistive switching mechanisms in resistive switching memory devices fabricated using various organic polymers.

1.4 Thesis Outline

This dissertation consists of eight chapters. Chapter 1 gives a brief introduction and literature survey on different types of memory devices while focusing on ReRAMs. Chapter 2 discusses techniques used for the fabrication and characterization of the devices reported in this study. Chapter 3-7 are results chapters. In chapter the results of resistive switching in the ReRAM device that uses chitosan dispersed with CdTe/CdSe core-shell quantum dots fabricated using the spin coat and drop cast methods are discussed in chapter three and chapter four, respectively. Chapter five discusses the results of resistive switching in ReRAM devices that use polyvinylpyrrolidone/molybdenum disulfide composite as an active layer having different molybdenum disulfide weight percentages. Chapter six discusses the results of resistive switching in ReRAM that uses chitosan and polyvinylpyrrolidone composite as an active layer. Chapter seven discusses the first ReRAM device to use raw cow milk as the active layer. In chapter 8, we conclude based on all the material studied and the results obtained in this study. Lastly, we provide the bibliography for all the literature cited in this thesis.

Chapter 2

Fabrication, characterization and experiment techniques of memory devices

2.1 Introduction

This chapter provides a brief overview of the materials used, their preparation, and characterization techniques used in this study. This study used materials such as chitosan, polyvinylpyrrolidone (PVP), and cow milk as host materials. Even though PVP is a synthetic polymer, both chitosan and PVP are non-toxic and biodegradable polymers, thus adding vital advantages to our fabricated devices[62–64]. Figure 2.1. shows the chemical structures of chitosan (a) and PVP (b).

Conductive dispersants such as molybdenum disulfide (MoS_2), CdTe/CdSe co-capped core-shell quantum dots (CdTe/CdSe QDs), selenium (Se) and more were used to increase the conductivity of the host materials. Aluminum (Al), indium doped tin oxide coated polyethylene terephthalate (PET-ITO), and silver (Ag) were used as electrodes. Table 2.1 provides the summary of these materials, their suppliers and product numbers. In the following subsections, we shall discuss the different ways of preparing the active layers,

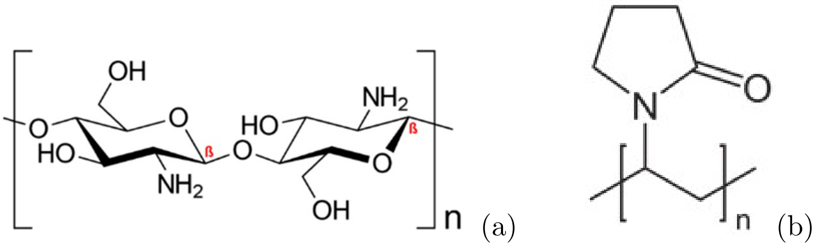

Figure 2.1: Molecular diagram of (a) chitosan and (b) PVP polymers (Images are taken from wikiwand.com.)

their characterization techniques such as atomic force microscopy (AFM), scanning electron microscopy (SEM), energy dispersive X-ray spectrometer (EDS) and Keysight source/measure unit (SMU) all available at UNISA department of physics.

Table 2.1: The summary of materials used in this study and their suppliers.

Material	**Supplier**	**Product number**height
Host materials		
Chitosan	Sigma Aldrich	419419
PVP	Sigma Aldrich	PVP40
Cow milk	-	n/a
Dispersants		
MoS_2	Sigma Aldrich	234842
CdTe/CdSe Core-shell	Synthesized	n/a
Se	Sigma Aldrich	229865
Substrates and electroded		
Al sheets	Sigma Aldrich	266957
PET-ITO	Sigma Aldrich	749729-1EA
Ag paste	Sigma Aldrich	735825height

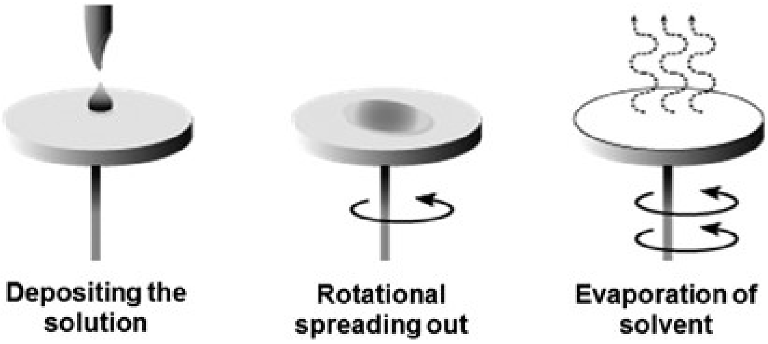

Figure 2.2: Schematic diagram depicting the steps involved in the spin-coating method.

2.2 Thin-film deposition and device fabrication

Host polymers such as chitosan and PVP were first dissolved in water or a solvent such as isopropyl alcohol. The completely dissolved polymer may be dispersed with conductive particles to make a composite depending on the targeted material. Next, the substrates were cleaned thoroughly using the sonication method. The composite was then deposited on a precleaned substrate using the drop cast or spin coating method. The polymer composite solution is directly poured on the substrate and left to dry to form a film in the drop cast method. Whereas deposition using the spin coating method is performed by placing a small polymer composite solution on the substrate placed inside the spin coating machine and then spinning until a thin uniform thin film was formed[65, 66]. Figure 2.2 shows the schematic diagram summarizing the spin coating method, while Fig. 2.3 shows the actual spin cleating machine available at UNISA. Compared to the drop cast coating method, spin coating is fast, produces a uniform film, and has a large coating area[66].

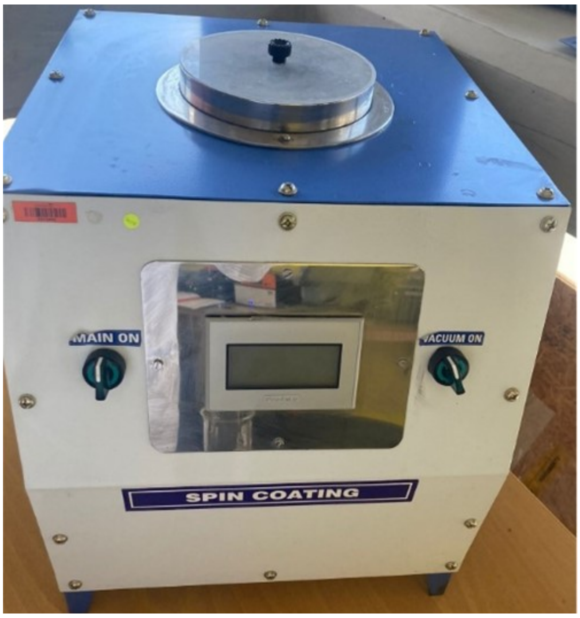

Figure 2.3: The photograph of a spin coating machine available at UNISA

2.3 Characterization

2.3.1 Topography and Morphology study

Atomic Force Microscope

Atomic force microscopy (AFM) is a common technique used to study the topography of a nanoscale material[67]. AFM offer outstanding resolution on the order of a fraction of nanometer, making them 1000 times better than the optical diffraction limit[68]. The first AFM was developed by Binning *et al.* in 1986[69]. Many different AFM makes and models are currently available in the market. Figure 2.4(a) shows the photograph of the Nanosurf FlexAFM used at UNISA. While Fig. 2.4(b) shows a simplified diagram depicting the operating principle of a typical AFM. As shown in the sketch, the AFM uses a tip attached to a spring cantilever usually made of silicon nitride to

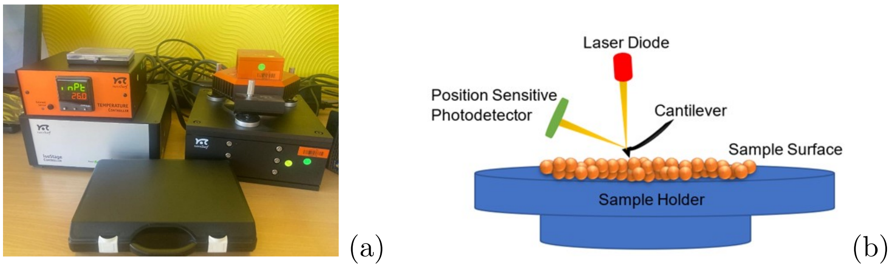

(a) (b)

Figure 2.4: A photograph of a Nanosurf FlexAFM available at UNISA, and (b) a schematic diagram showing the working principle of a typical AFM.

approach the sample at a subatomic distance to acquire the image. A laser beam is shone onto the cantilever tip and reflected towards a photodetector, which detects the tip's deflection caused by the interaction with the sample surface. Different modes, such as contact and non-contact modes, are used to map the sample's topography.

Scanning electron microscope and EDS

A scanning electron microscope (SEM) is a type of microscope that use a beam of electrons to scan the surface of a material. Different SEM makes and models are available on the market. These SEM architectures are different based on the electron gun used to generate the beam of electrons used for scanning the sample. For example, thermionic-emission gun (TEG), field-emission gun (FEG) and Schottky-emission gun (SEG) are used in different SEM systems[70]. Figure 2.5(a) shows the photograph of a JEOL JSM-7800F field-emission gun scanning electron microscope (FEG-SEM) available at UNISA. On the other hand, Fig. 2.5(b) shows the simplified diagram of the essential components of a typical SEM. Electron beam, also called electron probe generated by the electron gun, is passed through a focusing lens to the surface of a specimen. Upon interacting with the sample, secondary electrons, backscattered electrons, transmitted electrons, charac-

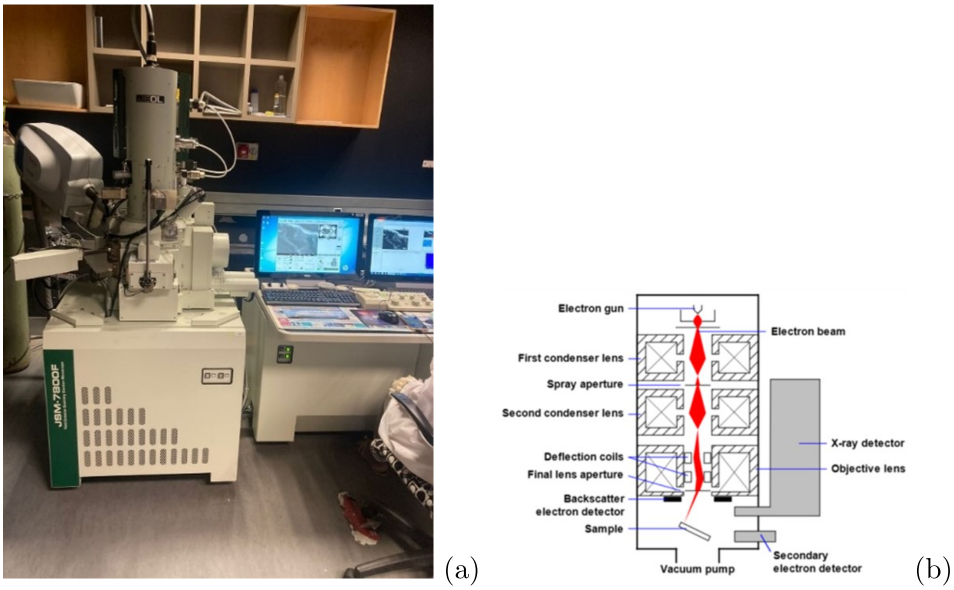

(a) (b)

Figure 2.5: (a) the photograph of a JEOL JSM FE-SEM available at UNISA labs, and (b) a typical SEM schematic diagram. Image is taken from[NanoScienceinstruments2018].

teristic X-ray and auger electrons are emitted from the sample, as shown in Fig. 2.6[71]. These signals are used to obtain information about the morphology and topography of a sample. Additionally, other SEM attachments such as energy dispersive spectrometer (EDS) can be coupled with the SEM system to obtain element analysis of the sample. The JEOL JSM-7800F FEG-SEM used at UNISA is coupled with the ThermoFisher EDS instrument.

2.3.2 Electrical transport study using the Keysight SMU

Figure 2.7 is a photograph of the Keysight precision source/measure unit (SMU), B2901A model, available at UNISA. This SMU is one of the most accurate and flexible SMUs available on the market. SMUs allow the user to do current measurements against varying voltage or voltage measurements

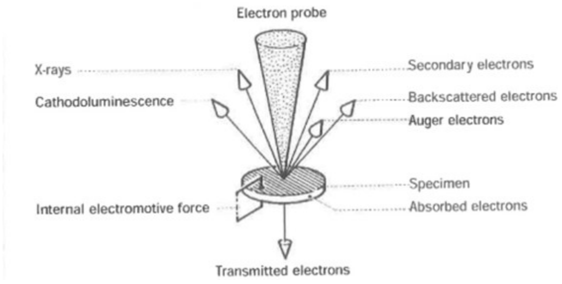

(a)

Figure 2.6: Schematic diagram showing different signals obtained from a FEG-SEM specimen. Image is taken from[JeolManual].

against the varying current at excellent precision of a minimum 10 $fA/100\,nV$. The B2901A model offers broad voltage range (210 V) and current (3 A DC and 10.5 A pulsed) sourcing capability allowing wide voltage or current scan.

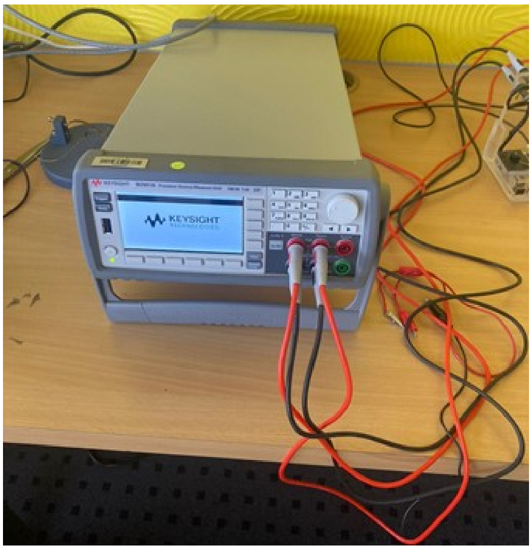

Figure 2.7: A photograph of the Keysight precision source/measure unit (SMU) B2901A available at UNISA.

Chapter 3

Resistive Switching in CdTe/CdSe core-shell quantum dots embedded Chitosan-based Memory devices

3.1 Introduction

Electroactive organic materials and composites have revolutionized the modern electronics industry by showing applicability in the fabrication of devices such as organic light-emitting diodes (OLED)[72, 73], organic photovoltaic (OPV) cells[74], organic transistors[75, 76], and many more. Organic materials have advantages such as biodegradability, low fabrication costs, and some may even offer properties for futuristic electronics such as transparency and flexibility[77–79]. Organic materials have also been widely explored to fabricate emerging memory devices called resistive switching memory (ReRAM or RRAM)[11, 43, 47, 49, 63, 80–82]. ReRAM is a two-terminal device with an active layer, e.g., a thin film sandwiched between two electrodes[11]. Each ReRAM cell has two distinctive resistive states, i.e., a high resistive state (HRS), also known as the OFF state, and a low resistive state (LRS), also known as the ON state, corresponding to logic “0” and “1”, respectively.

These resistive states are selectable through the write voltage, i.e., V_{SET} or erase voltage, i.e., V_{RESET} by applying either of these two voltages at the electrodes to switch the resistance of the cell from HRS-to-LRS, or LRS-to-HRS, respectively[39]. ReRAMs have advantages such as nonvolatility, low operating voltage, short write/erase time (100 ns/10 ns), almost limitless cell miniaturization, long retention time ($> 10^5\ s$), and high endurance ($> 10^5$ Cycles). These properties qualify them as potential candidates to replace the current memory giants, i.e., dynamic random access memory (DRAM) and Flash memory. Chitosan is among the most studied biopolymer for ReRAM application. The precursor of chitosan, chitin is a naturally occurring and abundant polymer. Chitosan itself is a cationic polymer obtained by deacetylation of chitin[55, 62, 83]. Chitosan possesses strong biding affinity for proteins and lipids such as fats and cholesterol[62]. Several chitosan-based ReRAMs have been reported[63, 84], with bipolar switching being dominant. Multi-switching behaviour has also been observed for the graphene oxide incorporated chitosan having indium doped tin oxide (ITO) and nickel (Ni) electrodes[84]. Hosseini *et al.* [55, 63] demonstrated the electrode dependence of the resistive switching mechanisms and overall device performance in silver (Ag) incorporated chitosan system with variety of electrodes system.

Quantum dots (QDs) are regarded as typical semiconductor nanoparticles reported in various studies due to their optical and photophysical properties, allowing them to find applications in diverse electronics engineering areas such as as biosensors and bio-imaging photovoltaic devices, and others[80, 85–87]. A typical example of QDs reported in the literature is cadmium telluride (CdTe) QDs[88, 89]. The coating of QDs surfaces with other semiconductor nanoparticles materials to produce core-shells is generally used to enhance the fluorescence properties, photo-stability, and bio-compatibility of the QDs[90–93]. Various examples of core-shells such as CdTe/CdS, CdTe/CdSe, CdTe/ZnS, CdTe/ZnSe have been reported and used in various applications such as fabrication of memory devices. Resistive switching in gelatin dispersed with CdTe QDs[58], PMMA with InP/ZnSe/ZnS core multi-shell[94], TiO_2 with CdS[95], CdSe/CdS core-shell[96] have all been reported. As far as we can ascertain there is no report of memory behaviour has been reported in a device that uses chitosan with CdTe/CdSe core-shell composite. Therefore, we herein report a study of resistive switching memory in ReRAM devices consisting of MPA-TGA-co-capped-CdTe/CdSe core-shell QDs embedded chitosan composites as active layers sandwiched between (1) Al and Ag and (2) ITO and Ag electrodes.

3.2 Experimental details

3.2.1 Materials and methods

Daramola and coworkers have previously reported the preparation, optical properties, and structural characterization of the CdTe/CdSe core-Shell QDs used in this study. [97] Here the freshly prepared sample of the core-shell QDs was supplied by Dalamora et al. with an estimated average particle size of 4.92 nm at 2.4 mg/ml.[98] High molecular weight chitosan in a powder form was purchased from Sigma Aldrich (310000-375000 Da, Prod. No. 419419) and used in this study. Preliminary experiments were conducted to optimize the mass ratio of the QDs to chitosan, yielding the 0.32 $wt\%$ of QDs to chitosan as the optimal combination. 1 ml CdTe/CdSe core-shell solution was first diluted into 50 ml ultra-purified water and stirred. 0.75 g chitosan was then added in the diluted QD solution and stirred. Two drops of acetic acid were added to the stirring chitosan solution and stirred further at room temperature for at least 4 hours until homogeneous chitosan solution was obtained.

3.2.2 Memory device fabrication

Metal-active/functional-layer-metal structured ReRAM devices were prepared with Al and ITO acting as bottom electrodes. A 1.00 mm thick Aluminium (Al) sheet (Prod. No. 266957) and polyethene terephthalate (PET) coated with 0.1 μm thick indium tin oxide (ITO) (Prod. No. 749729-1EA), both purchased from Sigma Aldrich, were cut and pre-cleaned by sonication (in acetone for 5 min, ethanol for 5 min, and finally using ultra-distilled water for 5 min in that order). Active layers were prepared by spin coating few drops of chitosan+QDs composite solution on a pre-cleaned Al or ITO, and span initially at 2000 rpm, 1800 rpm, 800 rpm and lastly 200 rpm, each instance the duration of the spin was 30 sec, with intervals of 30 sec between each spin rate. The deposited films were dried at room temperature for 24 $hours$. A silver (Ag) paste (Sigma Aldrich, Prod. No. 735825) was applied on each film as the top electrode and dried at room temperature for 48 hours. Figure 3.1 shows the schematic diagram of a typical ReRAM device fabricated with Al and Ag electrodes.

3.2.3 Characterization

Field emission gun scanning electron microscope (FEG-SEM) (ZEISS Ulta Plus) and atomic force microscope (AFM) (Anton Paar Tosca 400) were used to study the morphology and surface properties, and to estimate the thickness of the active layers. Electrical conduction and switching were probed using the Keysignt B2901 Source/Measure Unit (SMU).

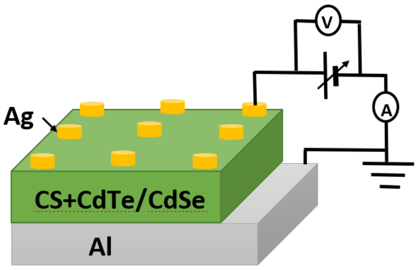

Figure 3.1: This figure shows a schematic diagram of the memory device fabricated on Al substrate, also showing is the simplified circuit of the current-voltage studies

3.3 Results and discussion

3.3.1 Topography study and thickness study

Figure 3.2(a) shows a 1 $\mu m \times 1$ μm FEG-SEM image. This image shows the morphology of a typical thin film consisting of the chitosan+QDs with 0.32 $wt\%$ QDs to chitosan. The image shows an even distribution of QDs NP in the chitosan medium and some clusters of QDs in areas shown by the arrows. Figure 3.2(b) shows a 1 $\mu m \times 1$ μm AFM phase trace image of the chitosan+QDs thin film. The image also reveals QDs NP clusters on the thin film surface. The size of QDs NP clusters are estimated to be in the range 28 $nm - 120$ nm. It is noteworthy to mention that the formation of CdTe/CdSe QDs NP clusters has been reported before.[98] Figure 3.2(c) is a 5 $\mu m \times 5$ μm AFM height trace image of the chitosan+QDs composite thin film. This topography image reveals a fairly smooth surface with mean roughness of 3.79 μm averaged over the entire area, with peaks of up to ~ 75 nm. As can be seen in Fig. 3.2(b), surrounding every QDs NP cluster, there appears to be a high density of chitosan. This high concentration of chitosan around the QDs NP site may be due to electrostatic interaction between the carboxylic group at the surface of the CdTe/CdSe QDs and the amino group at the surface of the chitosan[99].

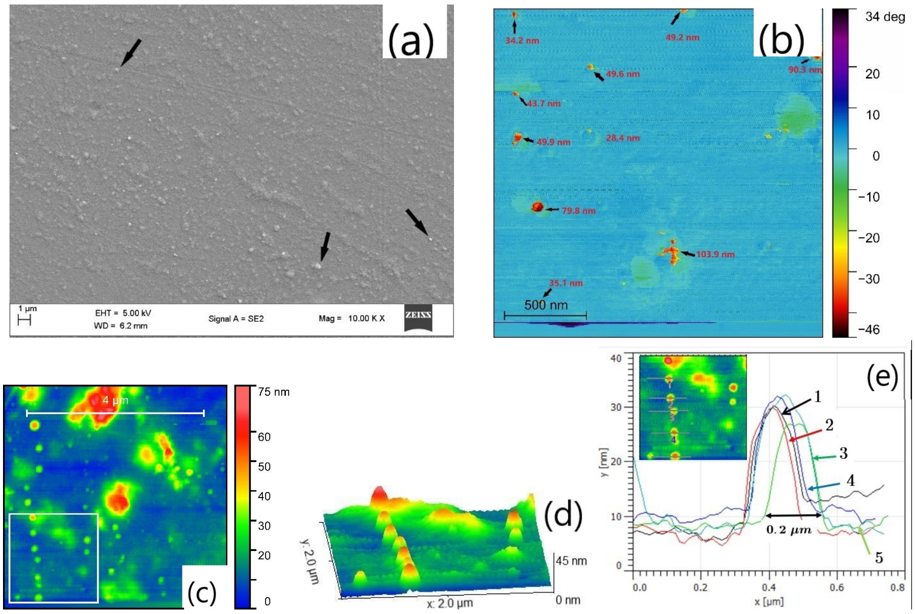

Figure 3.2: This image shows a 1 $\mu m \times 1 \mu m$ (a)FEG-SEM and (b) AFM phase trace images showing the distribution of QDs in the chitosan medium. (c) is a 5 μm AFM height trace image, while (d) is a 3D plot of the height trace image of the selected area in (c). (e) shows the line profiles constructed over the area selected in (c).

A small area in Fig. 3.2(c) was selected and plotted in 3D to produce a clearer visualisation of the chitosan and QDs interactions, as shown in Fig. 3.2(d). The line profile drawn over each interaction site shows an almost identical profile indicating diameters ranging about 0.2 μm as depicted in Fig. 3.2(e). From these FEG-SEM and AFM results, clusters of QDs may result in more electrostatic interaction with chitosan particles.

In Fig. 3.3, the results are shown for the measurement of thickness by the AFM step method. The topography image taken over the edge of the

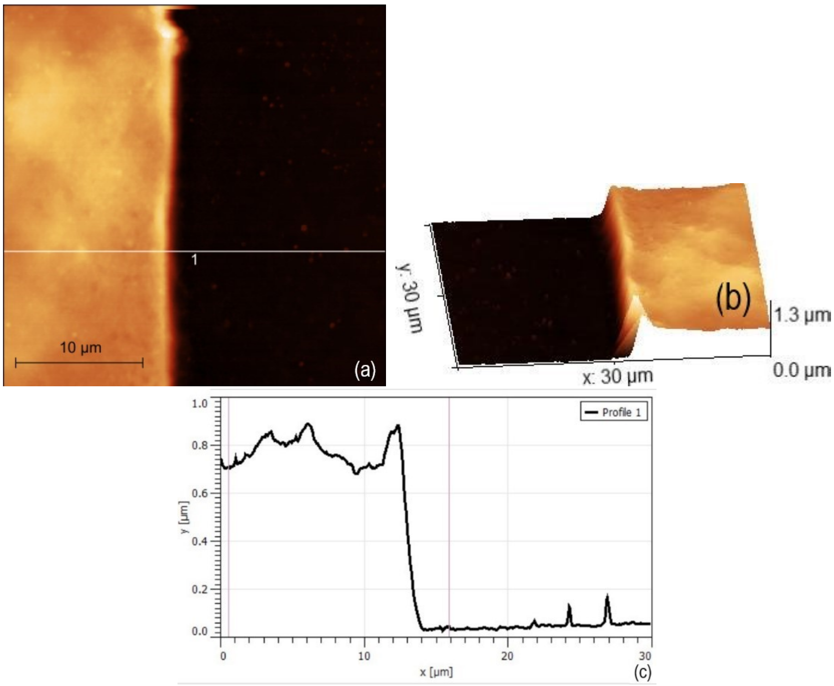

Figure 3.3: This image shows the thickness measurements of the active layers using step method. (a) shows the topography scan taken over the edge of the sample, and (b) is the corresponding 3D chart view.(d) shows the point-to-point estimation of the thickness.

film is shown in Fig. 3.3(a), and a clear step was obtained as shown in the 3D plot of in Fig. 3.3(b). Finally, point-to-point measurement was performed as shown in Fig. 3.3(c) to yield an estimated thickness of $\sim 661\ nm$.

3.3.2 Conduction and memory study

Electrical conduction and memory studies reported herein were all conducted at room temperature. Figure 3.1 shows a simplified diagram of the device connected to the Keysight SMU instrument. A bias voltage was applied at the top electrode (TE), i.e., Ag, while the bottom electrode (BE), i.e., Al or ITO, was grounded. The electroforming processes were induced by

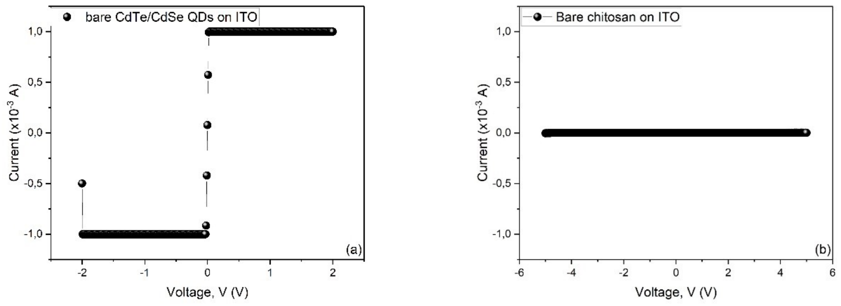

Figure 3.4: Typical I-V curve showing electrical characteristics of the ReRAM devices that use (a) bare CdTe/CdSe QDs and (b) bare chitosan as active layers sandwiched between ITO and Ag electrodes.

increasing the applied voltage from 0 by 10 mV steps with 25 ms delay, while simultaneously measuring the current in the device, until a sharp increase in current was observed. The memory behaviour of our devices was studied by sweeping the voltage from $0 \rightarrow +V_{max} \rightarrow -V_{max} \rightarrow 0$ while measuring the current through the device. A compliance current (I_{CC}) of 100 μA was used to protect our devices against permanent dielectric damage. Memory behaviour in raw chitosan and raw QDs was investigated, and no memory behaviour was observed, as shown in Fig. 3.4(a and b).

Figure 3.5(a-d) shows the I-V variation for the Al/Chitosan+QDs/Ag device. Figure 3.5(a) shows the electroforming I-V curve. The current is almost constant (slope $= 5.9 \times 10^{-7}\ \Omega^{-1}$) for an applied voltage in the $0 - 0.56\ V$ regime. A jump in the current (by $> 10^2$ orders of magnitude) was observed at 0.56 V, indicating electroforming. A linear current variation follows this electroforming process but with a higher slope ($1.0 \times 10^{-4}\ \Omega^{-1}$) at voltage beyond 0.56 V. Figure 3.5(b) shows the first voltage sweep cycle depicting memory behaviour of the Al/Chitosan+QDs/Ag device. From the I-V graph, one can see that the current increases with increase in the applied voltage, and a jump in current is observed at $V_{SET} = +1.32\ V$, where the

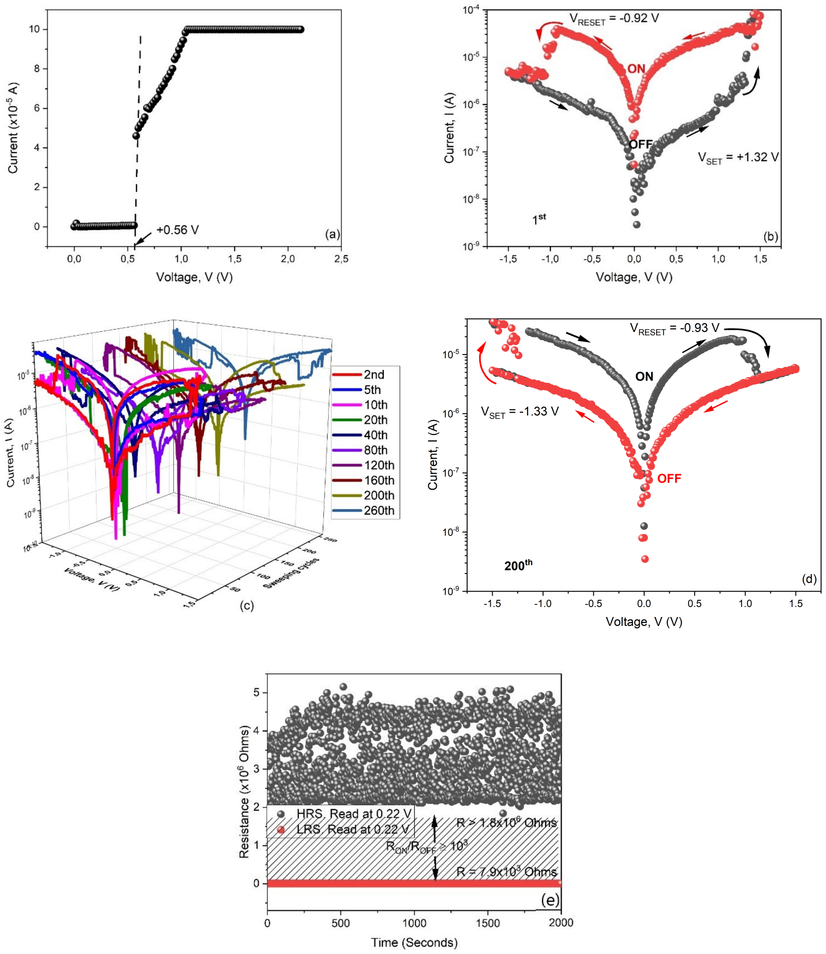

Figure 3.5: Typical I-V curves showing electrical characteristics of the Al/Chitosan+QDs/Ag device. (a) is the I-V curve for the electroforming process. (b) is the semi-log curves showing the memory behaviour during the 1st voltage sweeping cycle. (c) is the semi-log curves showing the memory behaviour during 260 voltage sweeping cycles, while (d) shows the 200th cycle showing interchanged V_{SET} and V_{RESET} polarities. (e) is resistance versus time graph showing the retention properties of the Al/chitosan+QDs/Ag device within the 2000 s.

device switches from the high resistive state (HRS), called the OFF-state, to the low resistive state (LRS), called the ON-state. This switching process is called the SET process. Upon decreasing the applied voltage back to zero, the current decreases without retrace its previous path, indicating a typical memory behaviour. When the applied voltage is increased in the negative voltage bias, the current increases until it sharply decreases at $V_{RESET} = -0.92\ V$, and the device switched from LRS to HRS, this is called the RESET process. Because of the sharp increase and decrease in current, as well as the absence of voltage-controlled negative resistance (VCNR) we can classified this behaviour asymmetric 'S-type' bipolar memory behaviour.[45] For this system, a reasonable large memory window, i.e., $ON/OFF \geq 10^3$, is obtained. Figure 3.5(c) shows the first 260 sweeping cycles performed for this device. This figure shows that the device has sustainable memory behaviour, making it applicable as a nonvolatile memory. It is interesting to notice that as the number of sweeping cycles increases, the polarities of V_{SET} and V_{RESET} become interchanged. Figure 3.5(d) shows the 200th cycle for this device. It is clear from the I-V data that even though the V_{SET} and V_{RESET} values are virtually unchanged, the polarities are changed. This is a unique ReRAM behaviour, observed and reported for the first time. In Fig. 3.5(e) we show the retention time of the ON- and OFF-state resistance of the Al/Chitosan+QDs/Ag device. In the regime $0 - 2000\ s$, our data shows stable ON-state resistance, while the OFF-state resistance fluctuates significantly within the 10^3 order range. This may be due to frustration in the system, that is happening just before switching. Beyond 2000 s, the OFF-state resistance fluctuated uncontrollably even between positive and negative magnitudes, making it hard to show that section in the plot.

The ReRAM device consisting of ITO BE, namely PET-ITO/Chitosan+QDs/Ag, shows a different behaviour than the Al/Chitosan+QDs/Ag device. Fig-

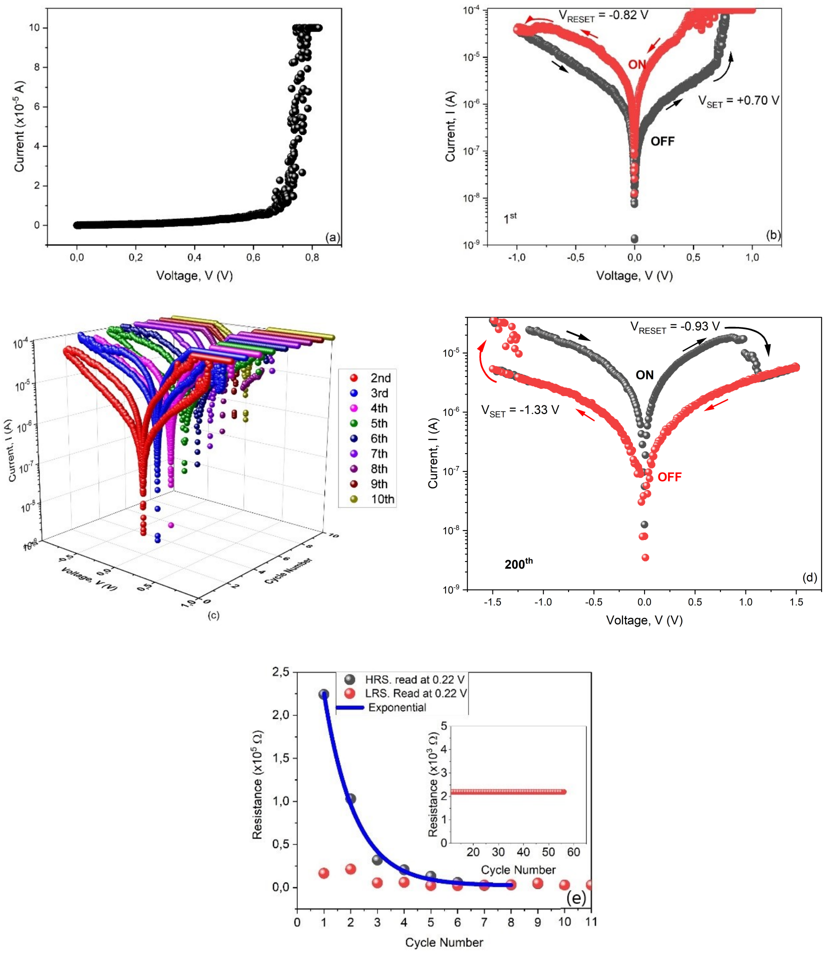

Figure 3.6: Typical I-V curves showing electrical characteristics of the PET-ITO/Chitosan+QDs/Ag device. (a) is the I-V curve for the electroforming process. (b) is the semi-log curves showing the memory behaviour during the 1st voltage sweeping cycle. (c) is the semi-log curves showing the memory behaviour during 10 voltage sweeping cycles, while (d) shows the 11th cycle showing that the device has lost its memory behaviour. (e) shows the ON- and OFF- state resistance against sweeping cycles showing endurance of the PET-ITO/chitosan+QDs/Ag device under 11 consecutive voltage sweeping cycles. The inset shows loss of memory beyond the 6th cycle.

ure 3.6(a-d) shows the electroforming and the variation of current with applied voltage for this device. From Fig. 3.6(a), the current varies linearly (Slope= $6.60 \times 10^{-6}\ \Omega^{-1}$) with applied voltage in the regime $0 - 0.58\ V$, following this state, the current diverts from linear and follows a parabolic relationship with applied voltage. Beyond the $0.70\ V$ the current rises steeply (Slope= $1.33 \times 10^{-3}\ \Omega^{-1}$) indicating somewhat electroforming process. Figure 3.6(b) shows the first voltage sweep cycle for this device. The $I - V$ variation shows that this device also exhibits a weak asymmetric 'S-Type' bipolar memory behaviour with $V_{SET} = +0.70\ V$ and $V_{RESET} = -0.82\ V$. Figure 3.6(c) shows I-V variation for the first 10 cycles. Our data shows that even though the device shows a nonvolatile memory behaviour, the memory behaviour vanishes with increase in the number of sweeping cycles, such that by the 11th cycle, the memory behaviour is totally lost, as shown in Fig. 3.6(d). Figure 3.6(e) (main and inset) is the ON- and OFF-state resistance plotted against the number of sweeping cycles. Our data shows that the OFF- state resistance decreases exponentially with number of sweeping cycle such that, by the 6th cycle, the two resistive states begin to coincide, indicating loss of memory behaviour.

3.3.3 Conduction and resistive switching mechanisms

Even though conduction mechanism in functional layers made of dielectric materials embedded with varieties of nanoparticles is still a search topic, several mechanisms such as Schottky emission, Fowler-Nordheim (F-N) tunnelling, direct tunnelling, thermionic-field emission, Poole-Frenkel (P-F) emission, hopping conduction, Ohmic conduction, space-charge-limited conduction (SCLC), ionic conduction, and grain-boundary-limited conduction have been reported[11, 44, 48]. In ReRAM devices that use organic material-based active media, SCLC formed conduction filaments (CF) is the most reported mechanism[44]. It is known that when a voltage is applied at one electrode while the other electrode is grounded, a current density, charge carriers may pass through the dielectric material, such that the current density (J) relates to the voltage (V) across the dielectric as, $J \propto V^n$. The constant n carries information about the possible mechanism, therefore n must be estimated from experimental data, by replotting the I-V data on log-log scale, i.e., $InJ - InV$ to determine the slope. For the Al/chitosan+QDs/Ag device, we replotted Fig. 3.5(b) and Fig. 3.5(d) on log-log scale as shown in Fig. 3.7(a and b) and Fig. 3.7(c and d), respectively. For the PET-ITO/chitosan+QDs/Ag device the log-log plots (of Fig. 3.6(b) appear in Fig. 3.8(a and b). The ON-state current in both Al/chitosan+QDs/Ag and PET-ITO/chitosan+QDs/Ag devices follow a linear variation with the applied voltage, with $n \sim 1$. This implies Ohmic conduction, i.e., $J \propto V$, with J the current density given by the expression[100]:

$$J = \frac{n_0 q \mu}{D} V. \tag{3.1}$$

The observed Ohmic behaviour implies that thermally activated carries with density, n_0, mobility μ, and travelling across a thickness, D dominate the current in the ON-state.

The OFF-state current in the Al/chitosan+QDs/Ag and PET-ITO/chitosan+QDs/Ag devices does not follow the same mechanism. Our data shows yet another linear current-voltage variation for the Al/chitosan + QDs/Ag device, but with low conductivity in both the positive and negative voltage bias. An Ohmic behaviour in both the OFF- and the ON- state can be attributed to the well-known filament conduction[22, 44, 54, 100, 101]. In the filament conduction there is a minimum of one nano-scale metallic filament bridging the BE and TE. The rapture and reformation of conduction filaments (CF) are the driving mechanism for the RESET and SET processes, respectively. Such a ReRAM is called conduction bridge ReRAM (CBReRAM). It is known that when a voltage is applied in a device, electrochemically active electrodes such as Ag or Cu; their ions, i.e., Ag^+ or Cu^{2+} ions can diffuse through the insulator layer and form CFs[44]. However, since no memory behaviour was observed in devices that use bare chitosan, even though the Ag electrode was used, we believe that our data rules out the possibility of formation of CF due to diffusion of Ag^+ ions. We believe that the CF suggested by our data might have been formed due to reduction ($M^{n+} + ne^- \rightarrow M$) of other cations, i.e., Cadmium constituents of the QDs, already present in the composite. Figure 3.7(c and d) show that even though the polarity of V_{SET} and V_{RESET} are interchanged, the device is still following the same RS mechanism, i.e., CBReRAM.

The OFF- state data shown in Fig. 3.8(a and b) for the PET-ITO/chitosan+QDs/Ag device reveal two distinctive regions of different slopes. In the low voltage region the slope ($n = 1$) increases to $n \approx 2$ at higher voltages. This observation suggests that the current density varies as the square of the applied voltage, which suggests the Mott-Gurney law ($J \propto V^2$)[100]:

$$J = \frac{9\epsilon\epsilon_0\mu V^2}{8D^3} \tag{3.2}$$

Here, all symbols have their usual meanings. Observation of Ohmic in the low voltage regime, followed by Mott-Gurney behaviour in the high voltage regime in the OFF-state, indicates that space-charge limited conduction (SCLC) mechanism[100] with threshold voltage, $V_T = 0.34\ V$ and $0.45\ V$ separating the linear and power regions in the SET and RESET processes respectively. SCLC driven filament mechanism in chitosan ReRAM device having ITO BE has been reported by others[63].

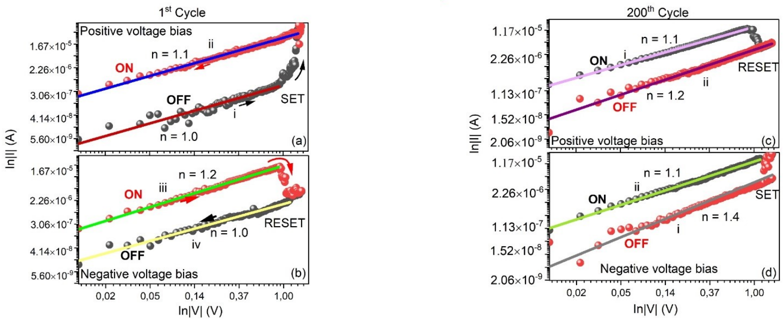

Figure 3.7: log-log fitting results of the conduction mechanism for the Al/Chitosan+QDs/Ag device. (a) and (b) show the positive and negative voltage bias region for the first sweeping cycle, while (c) and (d) is for the 200th sweeping cycle.

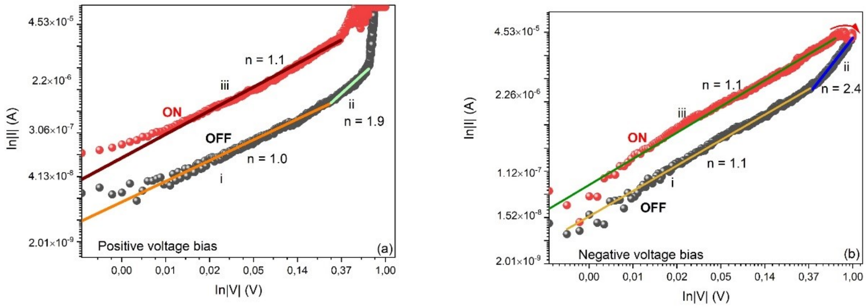

Figure 3.8: Log-log fitting results of the conduction mechanism for the PET-ITO/Chitosan+QDs/Ag device. (a) shows the positive voltage bias region, while (b) shows the negative voltage bias region.

Different switching mechanisms exhibited by the Al/chitosan+QDs/Ag and ITO/chitosan+QDs/Ag devices is a result of different BE, i.e., Al and ITO used. This conclusion is supported by other similar experiments conducted by other groups[63, 101–103]. Al and ITO have almost similar work functions ($\sim 4.2\ eV$)[104, 105]. However, several factors affect the work functions of a material, viz., the purity of the metal or samples used, the crystallographic face being observed, i.e. 100, 010 or 001[104, 105]. Therefore, the work function of the ITO used in this study might be different from 4.2 eV. Different work functions may result in interfaces, i.e., Al/chitosan+QD and ITO/chitosan +QDs, having different Schottky barriers (SB) height (estimated as the difference between the work function of Al (or ITO), and the electron affinity of the chitosan+QDs composite)[103]. If the work function of ITO used in this experiment is less than that of Al, the ITO/chitosan+QDs interface will have a small SB height. In such a case, electrons can be injected from the ITO through the SB into the composite where they interact with the features of the composite and the QDs nanoparticles, giving the features of SCLC. Similarly, if Al/chitosan+QDs has a higher SB height, the cell will rely on diffusion of M^+ ions than the electrons injection through the barrier. This could result with the electrode dependent RS features revealed by our experimental results.

3.4 Conclusion

In summary, we investigated resistive switching memory behaviour and conduction mechanisms in ReRAM cells that use CdTe/CdSe core-shell quantum dots embedded chitosan composite as active layers and Al and ITO bottom electrodes. Both Al- and ITO-based devices showed bipolar memory behaviour with switching voltage as low as 0.70 V, enabling the ReRAM to be operated at low powers. Furthermore, Al fabricated device showed conduction bridge-type resistive switching, while ITO fabricated device showed space-charge-limited driven conduction filament. Overall, our results demonstrate that CdTe/CdSe QDs embedded chitosan can be used as an active/functional layer for resistive switching memory. Our results significantly highlight the electrode's effect in electrical conduction and resistive switching in chitosan+QDs based devices. The reversal in polarity of V_{SET} and V_{RESET} in the Al-based device is an unknown phenomenon worthy of investigation in future studies.

Chapter 4

Conduction and Resistive Switching in Dropcast CdTe/CdSe Core-Shell Quantum Dots Embedded Chitosan Composite

4.1 Introduction

There is a need for biodegradable electronics to limit the steep rise in environmental pollution caused by the disposed-off electronics equipment. Thanks to their easy printability, low fabrication costs, abundance, and biodegradability, organic materials have shown properties which place them as candidates for modern electronics, such as organic LEDs[72, 77], photovoltaic cells[74] as well as organic transistors[75, 76]. In addition, organic materials have also demonstrated applicability in fabricating resistive switching memories (ReRAMs). ReRAM is an emerging sandwich-type memory device with an electrically interchangeable high resistive state (HRS), also known as the OFF-state, and low resistive state (LRS), also known as the ON-state[11, 40]. The resistive switching(RS) phenomenon was discovered in 1962 in devices consisting of metal-oxide active layers[38]. Recently, gelatin[58, 106], graphene[43, 107, 108], egg shell[47], egg albumin[109], pectin[56], aloe vera[54], and other biological materials[110, 111] have been used as active layers in various ReRAM modules. The commercialization of organic material based ReRAMs is hindered by several factors, the main one is that no device has shown all superior parameters. For example, the highest ON/OFF of $> 10^9$ was achieved in polyvinylcarbazole (PVK), while the highest endurance of ($> 7 \times 10^7$ cyles) was achieved using rose bengal[46]. Also, the lack of consensus on the single RS mechanism is another major obstacle in the development of commercial ReRAMs. Chitosan is one of the well studied biopolymers and is widely used for ReRAM application in the raw form[55], blended with other biopolymers[112–114], with nanoparticles[80], and as a substrate for flexible ReRAM devices[115]. As far as we can ascertain, there has not been any report on resistive switching in CdTe/CdSe core-shell quantum dots dispersed chitosan. We herein report on resistive switching based on CdTe/CdSe core-shell quantum dots embedded chitosan-based ReRAM devices sandwiched between ITO and Ag.

4.2 Experimental details

4.2.1 Materials and methods

A high molecular weight ((310000-375000 Da) chitosan powder/flakes were purchased from Sigma Aldrich ((Prod. No. 419419). In addition, a freshly prepared 2.4 $mg.ml^{-1}$ CdTe/CdSe core-shell quantum dots (QDs) was supplied by Daramola *et al.*[97]. Initially, 1 ml QDs stock was diluted to 50 ml, different masses of chitosan were added to each solution to make 0.96 $wt\%$ (S1), 0.48 $wt\%$ (S2), 0.32 $wt\%$ (S3), and 0.24 $wt\%$ (S4) of QDs to chitosan. Finally, a drop of acetic acid was added to the solution while stirring to facilitate a fast dissolution of chitosan. After 4 hours of stirring, homogeneous solutions were obtained.

4.2.2 ReRAM fabrication

Polyethene terephthalate (PET) coated with 0.1 μm thick indium tin oxide (ITO) (Sigma Aldrich, (Prod. No. 749729-1EA) was used as a substrate. The PET-ITO substrates were cut and pre-cleaned by sonication in acetone, ethanol and lastly in ultra distilled water each cleaning maintains 5 minutes. Next, each chitosan/QDs composite was drop cast on the substrate and allowed to dry at room temperature for over 24 hours. Lastly, a silver (Ag) paste was applied on each drop cast layer to serve as the electrode and allowed to dry for over 48 hours at room temperature. The ITO and Ag constituted the bottom electrode (BE) and the top electrode (TE), respectively. Four devices were fabricated, i.e., PET-ITO/chitosan/ QDs(S1)/Ag, PET-ITO/chitosan/ QDs(S2)/Ag, PET-ITO/chitosan/ QDs(S3)/Ag, and PET-ITO/chitosan/ QDs(S4)/Ag. Figure 4.1 shows the schematic diagram depicting the cross-section of the fabricated devices.

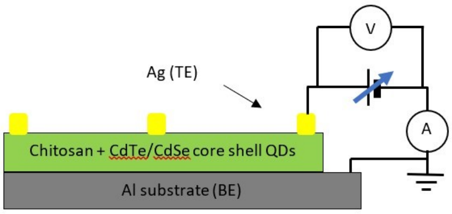

Figure 4.1: A schematic diagram depicting a cross-sectional are of a ReRAM device consisting of chitosan and CdTe/CdSe core shell QDs with Ag and Al electrodes. The circuit diagram shows a simplified experimental setup for current-voltage measurements

4.2.3 Characterization

Morphology and surface properties were studied using the ZEISS Ulta-Plus field emission gun scanning electron microscope (FEG-SEM) and Anton Paar Tosca 400 atomic force microscope (AFM). In addition, electrical conduction and switching were probed using the Keysignt B2901 Source/Measure Unit (SMU) connected as depicted in the simplified circuit in Fig. 4.1.

4.3 Results and discussion

4.3.1 Topography

Figure 4.2(a) is a FEG-SEM micrograph of the chitosan/CdTe/CdSe(S1) active layer. This micrograph reveals even dispensation of individual and clusters of CdTe/CdSe QDs nanoparticle in the chitosan medium. The formation of CdTe/CdSe QDs clusters has been reported in the literature before[98]. Figure 4.2(b) is an AFM topography image of the same chitosan/CdTe/CdSe(S1) active layer, while Fig. 4.2(c) is the corresponding 3D plot. These images reveal a virtually smooth surface with mean roughness of 8.85 nm and maximum pit-to-height distance of 180 nm. The particle-like patterns present in this micrograms may be sites of strong interaction between the CdTe/CdSe QDs clusters and chitosan, as reported by others[99].

4.3.2 Electrical study

The electrical conduction study was carried out by applying a potential at the top electrode(TE), while the bottom electrode (BE) was grounded.

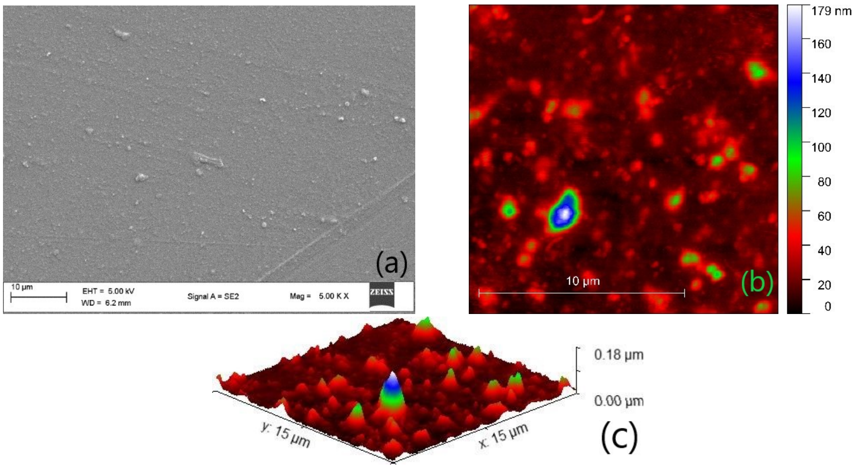

Figure 4.2: (a) FEG-SEM micrograph, and AFM height trace images of the chitosan/CdTe/CdSe active layer in (b) 2D and (c) 3D.

The potential was varied accordingly while recording current-voltage (I-V) variation. Firstly, each device were subjected to an electroforming process whereby voltage was increased from 0 to 15 V in steps of 10 mV with a time delay of 30 ms. The memory behaviour was also assessed using the same experimental parameters, but the voltage was swept to a complete cycle, i.e., $0 \rightarrow 15\ V \rightarrow 0 \rightarrow -15\ V \rightarrow 0$, while measuring the I-V variation. Figure 4.3(a) shows the electroforming I-V characteristics of the Al/chitosan/QDs(S1)/Ag device.

This I-V graph does not reveal any electroforming process. Instead, the current remains zero until the voltage reaches 2 V. After 2 V, a parabolic variation that gradually becoming more linear beyond 6 V is observed. The I-V characteristics showing the memory behaviour of this device is shown in Fig. 4.3(b). In this case, the current increases with the increase in applied voltage until the voltage reaches +2.44 V, marked as point A in the graph; at this voltage, the current seems to change its trajectory to follow a higher resistance path. In some ways, this behaviour resembles the RESET process, i.e., a change in current from low resistive state (LRS) to high resistive

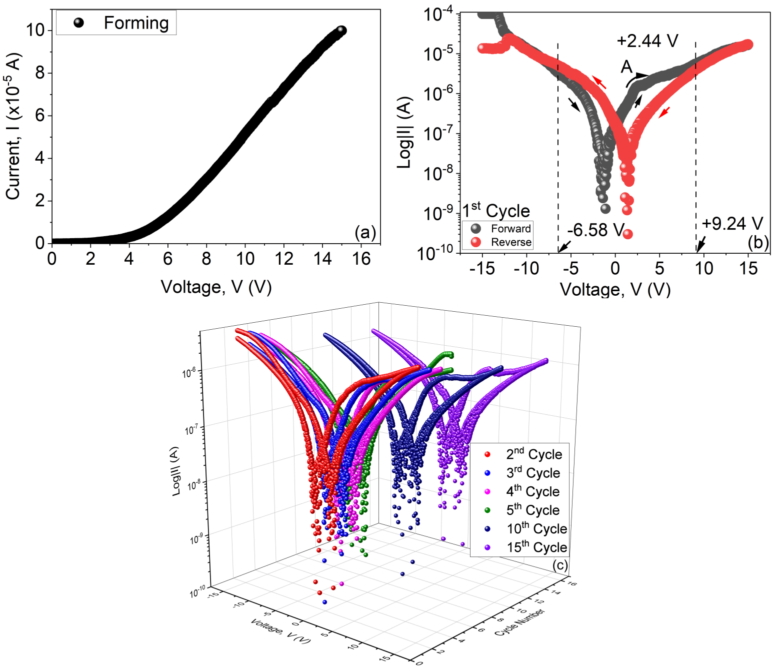

Figure 4.3: Electroforming I-V characteristics of the Al/chitosan/QDs(S1)/Ag device

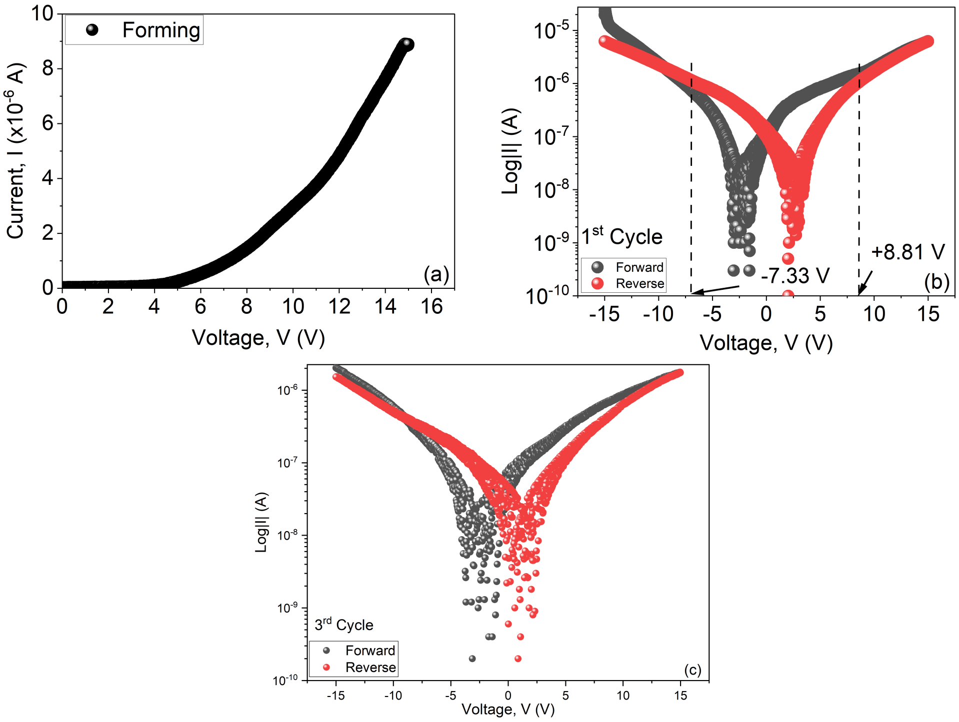

Figure 4.4: I-V characteristics of the Al/chitosan/QDs(S2)/Ag device, showing the electroforming curve.

state (HRS). Upon decreasing the voltage, the current does not retrace its original path. Thus, this creates a hysteresis. The I-V behaviour of this device in both positive and negative voltage bias is almost symmetrical. However, no obvious change in the current associated with the SET process, i.e., change from HRS to LRS, is observed in the negative voltage bias. Several hysteresis types, viz., 'N-Type', symmetric and asymmetric 'S-Type', and O-type' are associated with memory behaviour[45]. The I-V graph in Fig. 4.3(b) does not show any abrupt increase or decrease in current. Therefore we can categorize this memory behaviour as 'O-Type' memory behaviour. The 'O-Type' memory behaviour has been reported in other biological materials[49]. It is noteworthy that even though 'O-Type' memory behaviour is not unusual, our device's current-voltage variation shows that when the voltage is swept in the forward direction, the current follows a low resistance path, whereas, a high resistance path is followed when sweeping the voltage in the reverse direction. Such hysteresis characteristics has been observed in the Ag/keratin/ITO device and has been categorised as unipolar memory behaviour[116]. This behaviour is different from the one reported in the literature for the gelatin-graphene oxide system[49]. For the current voltage cycle, the 'O' shape hysteresis lies between $-6.58\ V$ and $+9.62\ V$. Figure 4.3(c) shows the I-V characteristics for the first 15 consecutive cycles of this device. Our data shows that despite significant signal noise, at voltage closer to $0\ V$, this device shows sustainable memory behaviour.

Figures 4.4(a-c) show the I-V characteristics of the Al/chitosan/QDs(S2)/Ag device. As depicted in Fig. 4.4(a), this device also does not show any electroforming. The current remains zero until the voltage reaches $4\ V$. Following this, the current seems to follow a parabolic path. This behaviour is different from that of the Al/chitosan/QDs(S1)/Ag device. The memory behaviour of this device appears in Fig. 4.4(b). The I-V data reveal yet another 'O-Type' memory behaviour, and the 'O" shape is found between $-7.33\ V$ and

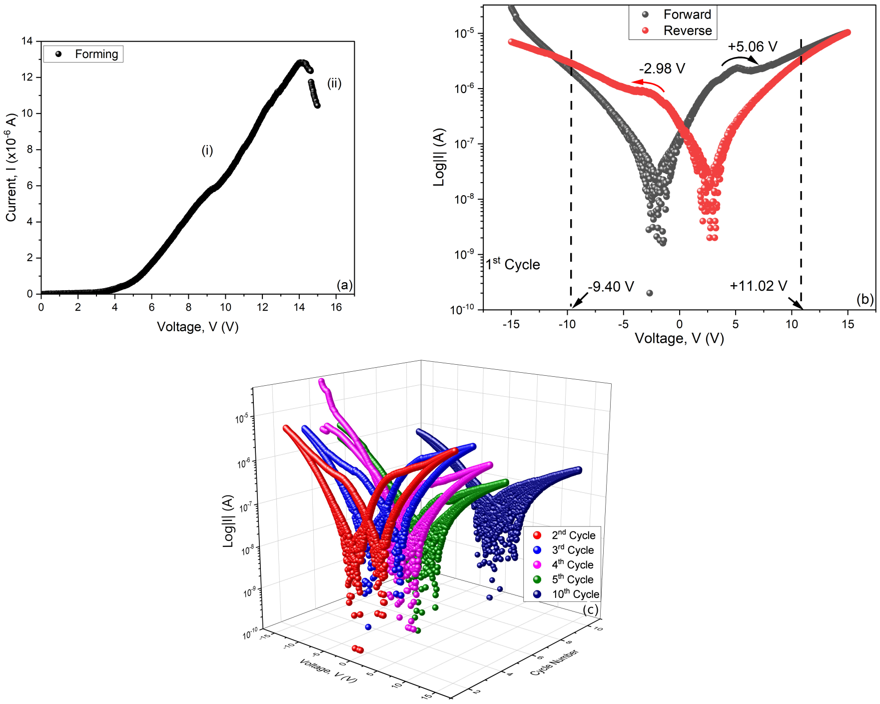

Figure 4.5: I-V characteristics of the Al/chitosan/QDs(S3)/Ag device showing the electroforming curve.

+8.81 V. For this device, the hysteresis curve is more homogeneous. However, there is intense signal noise occurring in the ±5 V range. Sweeping the voltage for the second time resulted in a significant increase in the noise and reduction of hysteresis, as shown in Fig. 4.4(c). This, we believe indicates rapid degradation of memory behaviour.

The data for the Al/chitosan/QDs(S3)/Ag device is shown in Fig. 4.5(a-c). Figure 4.5(a) shows the electroforming I-V graph. The data reveal slightly different I-V characteristics than those of the previous two devices. Here, as the voltage increases, the current emerges at 4 V and follows a parabolic path following a linear path in the region marked (i). However, a phenomenon called voltage-controlled negative resistance (VCNR)[45] is observed beyond 14 V, i.e., region (ii). Figure 4.5(b) shows the first I-V

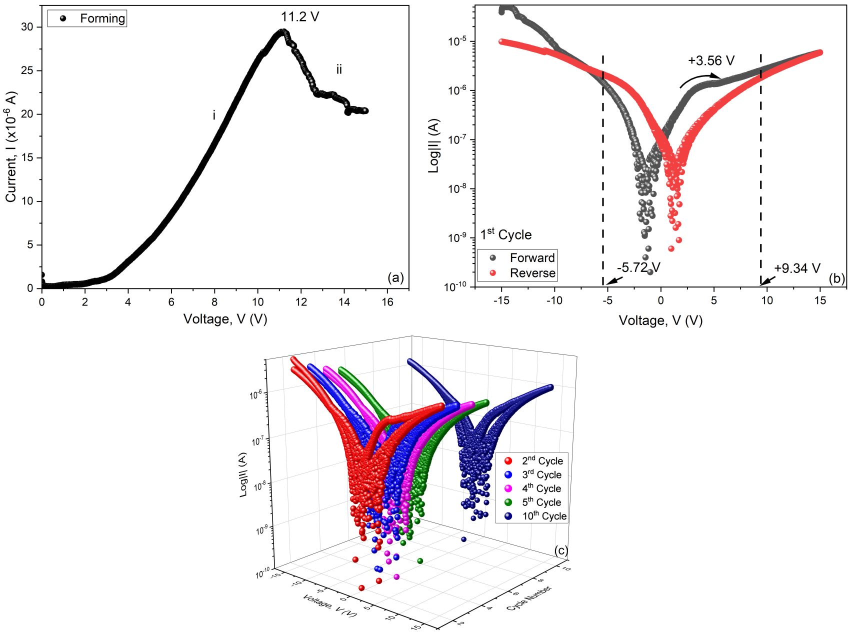

Figure 4.6: I-V characteristics of the Al/chitosan/QDs(S4)/Ag device, showing the first cycle.

variation of the first sweeping cycle. The data shows a relatively clearer hysteresis revealing yet another 'O-Type' memory behaviour, with the 'O' shape located at $-9.40\ V$ and $+11.02\ V$. However, there are indications of somewhat RESET processes taking place at $-2.96\ V$ and $+5.06\ V$. This device also shows strong signal noise at $\pm 5\ V$ range. Figure 4.5(c) shows first 10 sweeping cycles for this device. In this case, the data reveal increasing noise accompanied by a rapid decrease in conductivity and thus degradation of memory behaviour.

In the final set of diagrams, Fig. 4.6(a-c). Figure 4.6(a) show the I-V characteristics of Al/chitosan/QDs(S4)/Ag device. In Fig 4.6(a) we show the I-V characteristics of the electroforming process. Our data shows no evidence of electroforming in this device, the current remains zero until the voltage reaches about 3 V. Any further increase in voltage increases the current until at 10 V when current suddenly drops indicating the VCNR phenomenon. Figure 4.6(b) shows the ‘O-Type” memory behaviour, which also shows fast degradation of memory behaviour and increased noise as the number of cycles increases, as shown in Fig. 4.6(c).

4.3.3 Conduction mechanism discussion

Electrode dependent (Schottky emission, Fowler-Nordheim, direct tunnelling, and thermionic-field emission) and bulk dependent (Hopping conduction, Poole-Frenkel emission, Ohmic conduction, ionic conduction, space-charge-limited conduction, and grain boundary-limited) conduction mechanisms have been proposed for various ReRAM systems[99]. Our devices’ I-V characteristics show a homogeneous gradually increasing/decreasing current with applied voltage, and no abrupt SET and RESET processes. This indicates interfacial resistive switching. Therefore we shall narrow our search to bulk-dependent conduction mechanisms. In Fig. 4.7(a-d), we show the I-V variation fitting of the positive voltage bias of (a) Al/chitosan/QDs(S1)/Ag, (b) Al/chitosan/QDs(S2)/Ag, (c) Al/chitosan/ QDs(S3)/Ag and (d) Al/chitosan/ QDs(S4)/Ag devices. We shall first analyze the ON-state current behaviour in all devices. Our data shows that the ON-state current’s behaviour in all these devices is not the same. In the Al/chitosan/QDs(S1)/Ag device, the current remains almost zero ($n = 0.22 \approx 0$) in the $0 - 0.70$ V regime. After that, the current follows a linear ($n \approx 1$) behaviour, as shown in Figure 4.7(a)(Main figures). The relationship, $I \propto V^n$, with $n = 1$ which indicates that the dominant mechanism of the ON-state is Ohmic behaviour [117]. Ohmic conduction is given as[118]:

$$J_{Ohm} = q\mu N_C E \exp\left[\frac{-(E_C - E_F)}{kT}\right] \qquad (4.1)$$

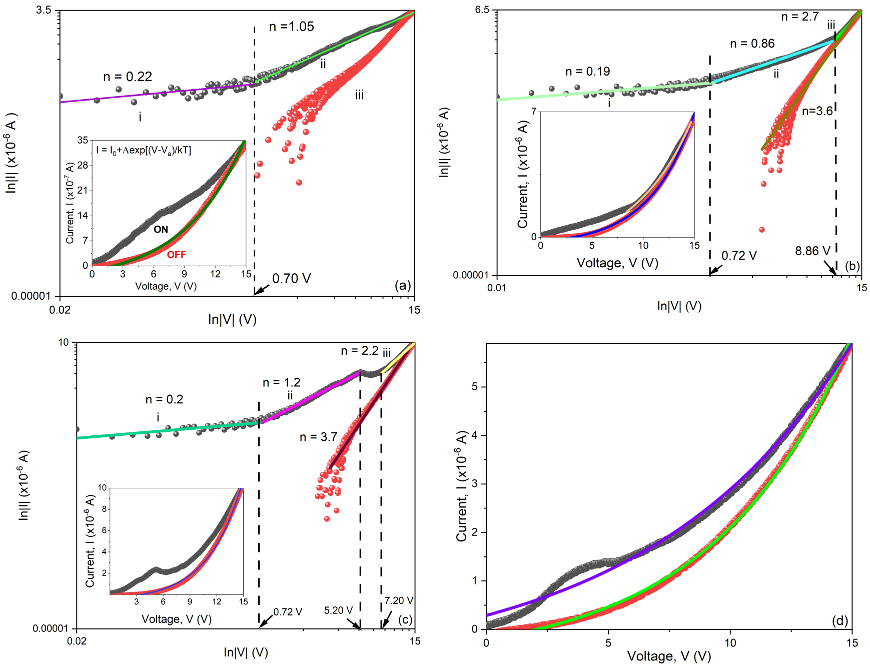

Figure 4.7: Figures a-d show the $\ln I - \ln V$ linear fitting, while the insets show the exponential function fitting of the I-V data for the (a) Al/chitosan/QDs(S1)/Ag, (b) Al/chitosan/QDs(S2)/Ag and (c) Al/chitosan/QDs(S3)/Ag devices. (d) shows the exponential fitting of the I-V data for the Al/chitosan/QDs(S4)/Ag device.

According to Lim and Ismail [118], μ is the electron mobility, N_C is the effective density of state of the conduction band, E_C and E_F are respectively the conduction band energy and the Fermi energy level, k is the Boltzmann constant, and T is the temperature in Kelvin. Ohmic behaviour of the ON-state has been associated with the formation of nanoscale conductive filament(CF)[119].

In the Al/chitosan/QDs(S2)/Ag device shown in Figure 4.7(b), the ON-state current behaviour is also shows zero current followed by Ohmnic behaviour in the low voltage regime ($0 - 0.70\ V$) and intermediate region ($0.70\ V - 8.86\ V$, respectively. In the high voltage region, i.e., beyond

8.86 V the current behaviour suddenly changes to a power behaviour with $n = 2.7$. A combination of these two consecutive regions, i.e., Ohmic and power, with $n > 2$, rules out the space-charge limited conduction mechanism. We re-plotted this high voltage region (see the inset) and noticed that this region could be fit perfectly with the exponential function, which may indicate a hopping conduction mechanism[49, 120]. According to Vallabhapurapu et al. [49] hopping mechanism equation is given as:

$$I = I_0 + A \exp\left[\frac{(V - V_a)}{kT}\right] \tag{4.2}$$

Here, I_0 is the residual current, $A = qan\nu$, is the product of electronic charge, mean hopping distance, number of electrons and thermal vibration frequency of electrons at the trap, V_a, is the characteristic voltage, k is the Boltzmann constant, and T is the temperature in Kelvin [49]. The Al/chitosan/QDs(S3)/Ag device follows the same behaviour as the The Al/chitosan/QDs(S2)/Ag device, except that in the high voltage regime, the exponent n was found to be $2.2 \approx 2$, indicating the possibility of the Mott-Gurney law. The combination of these two regions, i.e., Ohmic and then Mott-Gurney law, may indicate that the dominant mechanism is the space-charge limited conduction mechanism[100]. The Mott-Gurney equation is given as[100]:

$$J = \frac{9\epsilon\epsilon_0\mu V^2}{8D^3} \tag{4.3}$$

Here, D is the thickness of the active layer. All other symbols have their usual meanings. On the other hand, Al/chitosan/QDs(S4)/Ag device data fit perfectly with the exponential function. This indicates that the OFF-state current follows a single mechanism, i.e., hopping conduction.

The OFF-state current data of all the devices fit perfectly with the exponential function as shown in Fig. 4.7(a-c)(inset) and (d), indicating hopping conduction mechanism. Because the OFF-state current does not follow linear behaviour, this rules out the possibility of Ag diffusing into Ag^+ and for CF. Instead, we think that charge carriers hopes from the bottom electrode to the QDs particles, QDs particles to the next QDs particles and QDs particles to the top electrode. And that the different ON-state current behaviour is due to the different amount of QDs particles dispersed in the active layer.

4.4 Conclusion

In conclusion, electrical conduction and resistive switching in ReRAM devices that use CdTe/CdSe quantum dots nanoparticles dispersed chitosan as active layers were studied. 'O-Type' memory behaviour was observed in devices consisting of 0.96 wt%, 0.48 wt%, 0.32 wt% and 0.24 wt% CdTe/CdSe QDs to chitosan active layers deposited using the drop cast method on ITO surface. The increase in QDs nanoparticles dispersed in the chitosan resulted in different ON-state current behaviour, while the OFF-state current was driven by hopping conduction mechanism. We conclude that the memory behaviour and conduction mechanism in drop cast devices consisting of chitosan with CdTe/CdSe core-shell QDs dispersants can be manipulated by controlling the amount of QDs in the composite.

Chapter 5

Resistive Switching in Polyvinylpyrrolidone/ Molybdenum disulfide composite-based Memory devices.

5.1 Introduction

There is a significant increase in data and cloud computing during the fourth industrial revolution[121]. As a result, the current memory technology is under serious challenge as ultrafast and high-density memory devices are needed to meet the demand. Furthermore, the current memory technology must reduce its contribution to the rising ICT energy consumption, currently over 3% of the world's electricity consumption[122]. A total transformation in memory device technology is needed to meet these demands. Resistive switching memories (ReRAMs) are emerging memories comprising an active layer having two electrically switchable resistive states[38], i.e., a high resistive state (HRS) and a low resistive state (LRS). The active layer is sandwiched between the top electrode (TE) and the bottom electrode (BE) to make a complete memory cell[22, 123]. ReRAMs have advantages such as nonvolatility, low operating voltages, and high endurance, thus placing them at the centre of focus of emerging memory technologies. Additionally, ReRAMs can be designed from several materials, allowing them to be compatible with biodegradable[43, 55, 124–126], transparent[124, 125], flexible[55, 80, 126], and lightweight electronics[57].

Molybdenum disulfide (MoS_2) is a graphene-like 2D transition metal dichalcogenide compound with a layered structure comprising Mo-atom at the centre of a trigonal prism with two sulfur atoms[127]. MoS_2 has two variances, i.e., a metallic $1T$ with octahedral structure and a semiconducting $2H$ with trigonal prismatic structure[128]. The $2H$ phase has an energy gap of $\sim 1.9\ eV$[129], thus suitable for switching memory devices, transistors, and solar cells[128]. The electronic properties of MoS_2 have been well studied. Ohmic behaviour in pressed pellet form[127], bipolar memory switching in bare MoS_2 system with Cu and W_2N electrodes[130], and three different switching types, i.e., bipolar, asymmetric bipolar, and threshold switching (TS), in the same sample of MoS_2 and polyvinyl pyrrolidone (PVP) with Al and indium doped tin oxide (ITO) electrodes[131] have been reported. Wu *et al.*[132] have also showed that the energy consumption in the Pt/MoS_2 + PVP/ITO ReRAM can be significantly lowered by doping MoS_2 with nitrogen. This reveals the unpredictability of MoS_2 in different forms and different systems. In this work, we present a systematic study of resistive switching (RS) in devices with an active layer comprising (a) bare PVP, (b) bare MoS_2 (c) PVP/MoS_2 bilayer, and (d) PVP+MoS_2 nanocomposite with different MoS_2 $wt.\%$ viz., $10 - 40\ wt.\%$. All devices were fabricated with Al and Ag as BE and TE, respectively.

5.2 Experimental details

5.2.1 Solution preparation

The PVP (Sigma Aldrich, Prod. No. PVP40) and the MoS_2 (Sigma Aldrich, Prod. No. 234842) powders with $< 2\ \mu m$ particle size were separately dissolved in isopropyl alcohol (IPA) to produce 2.5 $w/v\%$ and 1 $w/v\%$ PVP and MoS_2 solution, respectively. Both solutions were stirred for 4 hours at room temperature.

5.2.2 Device Fabrication

Al sheet (Sigma Aldrich) was cut and pasted on a glass microscope slide and pre-cleaned by sonication (in acetone, then IPA, and lastly in ultra distilled water, each for 5 min). Active layers consisting of (1) 1.4 μm thick MoS_2 (device A), (2) 1.01 μm thick PVP(device B), (3) 1.2 μm thick PVP on 1.36 μm thick MoS_2 bilayer (device C) and (4) $\sim$ 1.50 μm thick PVP+MoS_2 nanocomposites with 10 $wt\%$ (device D), 20 $wt\%$(device E), 30 $wt\%$ (device F) and 40 $wt\%$ (device G) MoS_2 into PVP were spin-coated on the Al BE. Ag paste (Sigma Aldrich, Prod No. 735825) was applied on the top of the active layer as TE. Table 5.1 contains the notation used to describe all the devices fabricated.

5.2.3 Device characterization

Atomic force microscope (AFM, Nanosurf FlexAFM), and Field-effect scanning electron microscopy (FEG-SEM, JEOL JSM-7800F) equipped with an energy dispersive X-ray spectrometer (EDS, Oxford Aztoec 350 X-Max80)

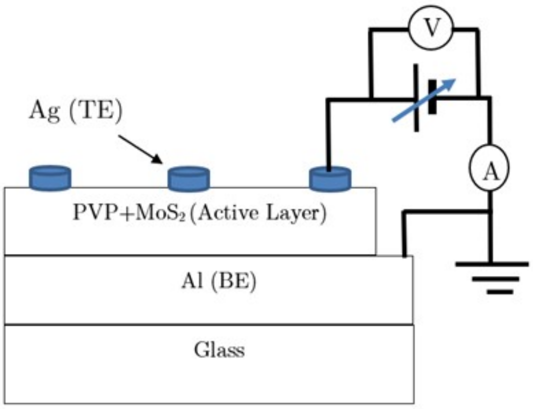

Figure 5.1: A schematic diagram showing the cross-section of a typical ReRAM cell and the I-V measurement scheme.

were used to estimate the thickness, study morphology and to estimate the chemical composition of the active layers, respectively. In addition, electrical studies were conducted using Precision Source/Measure Unit (SMU, Keysight B2901A), connected as shown in Fig. 5.1.

5.3 Results and discussion

5.3.1 Topology and composition

Figure 5.2(a and b) are high-resolution FEG-SEM micrographs of devices C and G, respectively. To acquire an image a highly energetic electron beam from the SEM's field emission gun was incident on the samples. Because of the high energy of this electron beam, the sample can be penetrated to some length, allowing the reconstruction of a 3D image of the sample from the back-scattered electrons. Our SEM results reveal that in both samples MoS_2 appeared in the form of agglomerates of different sizes. In device C where the MoS_2 bottom layer is under the PVP layer, the SEM would

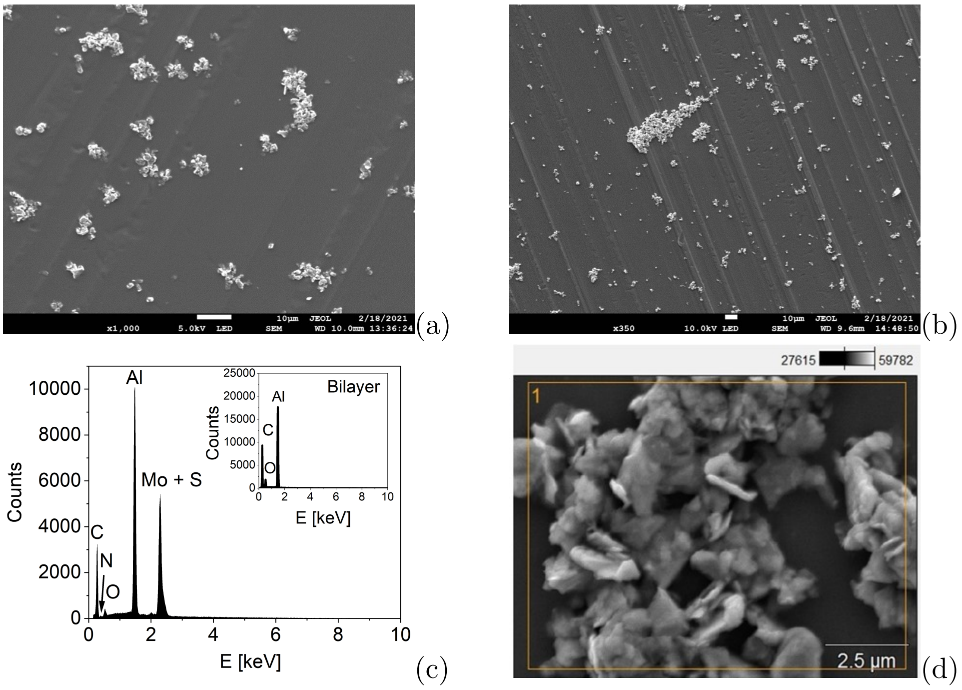

Figure 5.2: (a) and (b) are FEG-SEM micrographs of the active layer of device C and device G, respectively. (c) is the EDS spectrum of device G (main graph) and device C (inset). Lastly, (d) is the magnified FEG-SEM micrograph of the MoS_2 agglomerate inside a PVP polymer.

only study the PVP layer. However, our results reveal that the large MoS_2 agglomerates from the bottom layer penetrated the PVP top layer and were detected by the SEM. In device G, however, our SEM results show even dispensation of MoS_2 particles, such that even agglomerates having a small size are visible in the micrograph as expected. Figure 5.2(c) shows the EDS results taken from the surface of device G (Main figure) and device C (Inset). As expected MoS_2 traces were found only on the composite film. Lastly, Fig. 5.2(d) depicts the magnified SEM image of a MoS_2 particle cluster, which reveals that the MoS_2 used in this study had flakes like, i.e., 2D form.

5.3.2 Electrical studies

Current-voltage (I-V) data of device A with a single MoS_2 active layer and device B with a single PVP as the active layer did not show any resistive switching. Figure 5.3 shows the semi-logarithmic I-V characteristics of (a) device C, and (b) device G. The I-V characteristics of both devices reveal symmetric 'S-type' bipolar memory behaviour[45, 133] with $ON/OFF \geq 10^2$, and very low operating voltages ($V_{SET} = -0.50\ V$ and $V_{RESET} = +0.40\ V$ for device C, and $V_{SET} = +0.56\ V$ and $V_{RESET} = -0.70\ V$ for device G). Furthermore, in device C, a TS is observed (with $V_{hold} = +0.54\ V$ while $V_{th} = +0.80\ V$) beyond $+0.40\ V$. This TS is not observed for negative voltage bias in this device. Even though a TS behaviour in ReRAMs is expected when a high compliance current (I_{CC}) is applied, the presence of this TS in only one voltage polarity is an uncommon behaviour.

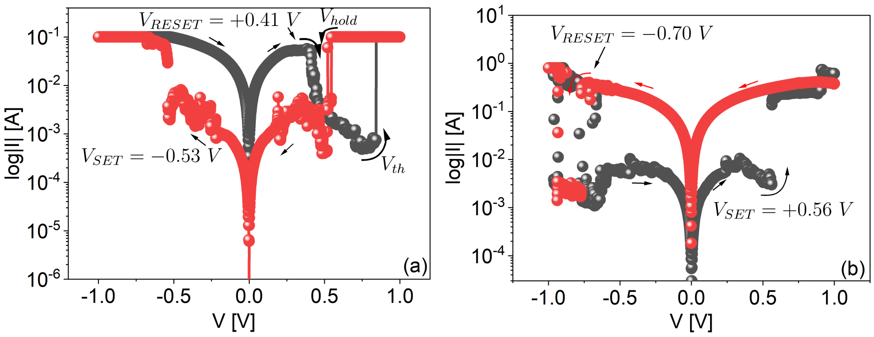

Figure 5.3: I-V characteristics of (a) device C and (b) device G in semi-logarithmic scale.

In contrast, no TS was observed in device G, despite large ($0.8\ A$) I_{CC} used. Instead, somewhat multiple switching is observed only in the positive voltage polarity. The change in RS due to manipulation of active layers

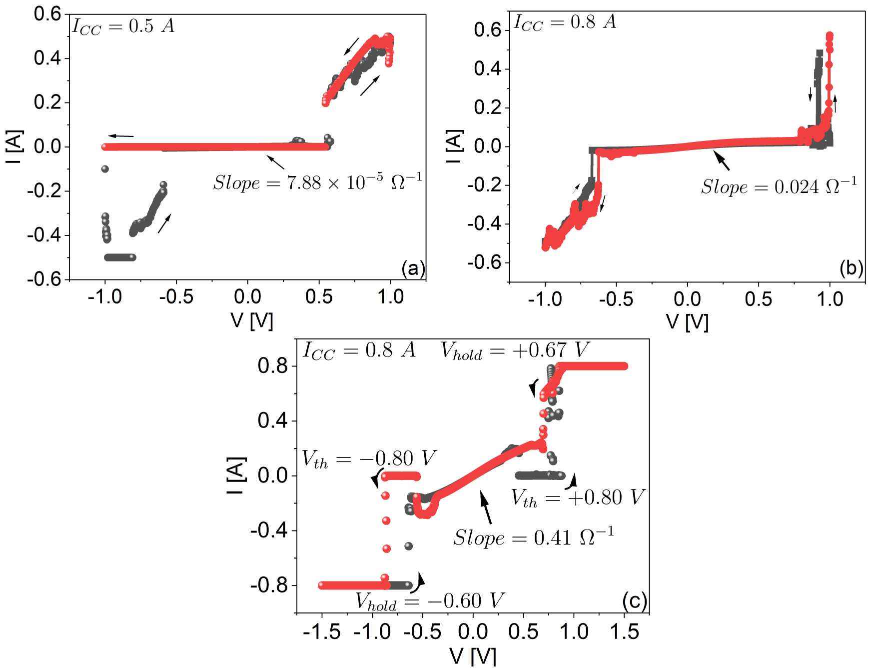

Figure 5.4: The I-V characteristics of (a) device D, (b) device E, and (c) device F.

has been reported by Sun *et al.*[134]. Their results showed asymmetric TS in $Al/TiO_2/Pt$, symmetric bipolar RS in Al/DNA/Pt, asymmetric bipolar RS in $Al/TiO_2 - DNA/Pt$ bilayer and multiple switching in $Al/TiO_2 - Graphene - DNA/Pt$[134]. These results show that stalking different layers as the active layer significantly changes the electric transport and switching in the device. This difference in the RS behaviour of devices C and G may arise because of the unique nature of active layers used in the two devices.

Figure 5.4 shows the I-V characteristic of (a) device D, (b) device E, and (c) device F, respectively. All three figures show a linear variation in current with the applied voltage before switching. Linear fits to these graphs yield slopes of $7.89 \times 10^{-5}\ \Omega^{-1}$, $2.4 \times 10^{-2}\ \Omega^{-1}$, and $4.1 \times 10^{-1}\ \Omega^{-1}$, respectively. This increase in slope may signify an increase in electrical conductivity with increasing MoS_2 content in the nanocomposite layer. RS in these devices occurs at low voltages of about ±0.60 V. Though devices D and E exhibit a jump from HRS to LRS, the current retraces its path by changing voltage sweep direction showing no significant hysteresis. Such behaviour signifies a non-memory-like character of the device. On the other hand, device F exhibits a TS for voltages greater than ±0.6 V with V_{hold} and V_{th} of ±0.60 V and ±0.80 V, respectively. Thus, it appears that the memory behaviour in PVP+MoS_2 nanocomposite devices can be controlled by controlling the amount of MoS_2. In the following subsection, we shall analyze device C and G's conduction mechanism, as these devices exhibited optimal memory behaviour.

5.3.3 Conduction mechanisms and RS in devices C and G

To understand the conduction mechanism leading to the RS in ReRAM devices, one can estimate the value of n for the current density and voltage relationship, i.e., $J \propto V^n$ [49, 117, 135]. Figure 5.5(a and b) shows the $\ln|I|$ vs $\ln|V|$ plots corresponding to device C, while Fig. 5.6 is for device G. The $\ln|I| - \ln|V|$ graphs for both device C and G show that $n \sim 1$, in the ON-state, indicative of Ohmic behaviour, i.e., $J \sim V$[120]. This Ohmic behaviour in the ON-state current suggests the presence of conduction filaments (CFs). To understand the mechanism of the formation of these CFs in both systems, an analysis of the OFF-state current must be done. The OFF-state current variation of device C shows two distinct regions, namely, region i and ii, as shown in Fig. 5.5(a). In region i, the current variation is very clear without any noise and is fitted very well with the linear fit ($n = 1$) with a very small (0.0023) standard error. In region ii, however, we see large fluctuation, which we believe that the active layer is now preparing itself for the resistive switch. As such any fit in this region is ambiguous. After trying different fits, linear fit with $n \sim 1.8$, was our best fit with $R^2 = 0.698$

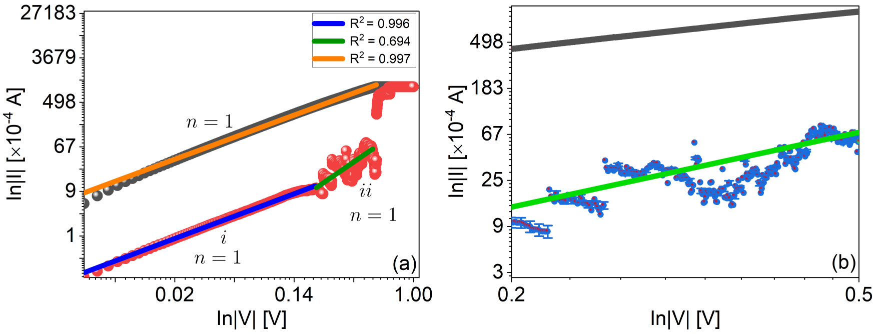

Figure 5.5: ln(I) versus ln(V) plots of device C, showing the entire forward and reverse sweep of the negative voltage bias (a) and the magnified graph of region ii.

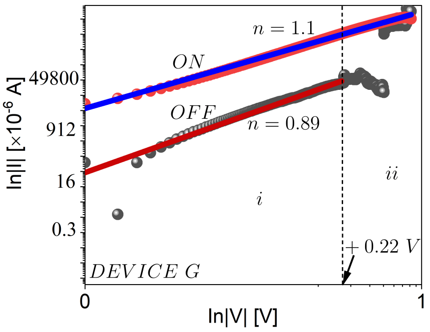

Figure 5.6: ln(I) versus ln(V) plots of device G.

and standard error of 0.070. Figure 5.5(b) is a magnified graph of region ii. This graph reveal that, even though linear fit is weak, one can notice that despite the noise, the current seem to take a trajectory with larger (> 1) n value compared to region i. The $n = 1.8$ value obtained in this region weakly gives a trend pointing towards the possibility of the M-Gurney law ($J \propto V^2$)[120], viz.,

$$J = \frac{9\varepsilon\varepsilon_0\mu V^2}{8D^3} \tag{5.1}$$

Here D is the thickness of the dielectric, and all other symbols have their usual meanings.

The occurrence of $J \propto V$ and $J \propto V^2$ in two consecutive regions implies that the possible mechanism taking place in device C is space-charge limited conduction (SCLC)[11, 136], with transition voltage, $V_{tr} = 0.24\ V$. The TS observed in positive voltage bias is not understood. However, others have reported that a large I_{CC} can cause the TS[137] or be caused by other unidentified reasons[120, 136]. Large I_{CC} used in our measurements provides room for TS to occur because of Joule heating[138]. The conduction mechanism in device G differs from that of device C. The OFF-state current of device G follows a linear behaviour ($n = 0.89\ approx 1$) in the low voltage regime, i.e., region i ($0\ V - 0.22\ V$). Beyond this voltage, i.e., region ii, a decrease followed by an abrupt increase in current occurs, taking the device to LRS. This behaviour deviates from the SCLC behaviour displayed by device C. We shall attempt to explain this behaviour.

When a potential is applied, say at the Ag electrode, there is electron accumulation at the Al electrode, while the Ag has electron deficiency. These electrons can tunnel through the Al/PVP+MoS_2 interface into the active layer containing the MoS_2 particles, resulting in the trend seen in region i[138]. According to Shinde *et al.*[139], this charge can be trapped because of the low energy level or quantum confinement effect in the MoS_2 system, which can explain the trend observed in region ii. When the voltage is sufficiently high, electrons gain enough energy and jump to the conduction band of the MoS_2 in the nanocomposite[140], resulting in high conductivity and hence HRS-to-LRS switching. Conduction behaviour observed in our devices differs from that reported for the $Al/MoS_2 + PVP/ITO$[131], ITO/N-doped MoS_2-PVP/Pt[132], and Ag/ MoS_2 -PVP/Ag[140] devices. This comparison shows that the type of electrodes, nanocomposite constitution, and composition play essential roles in conduction mechanisms in these polymeric ReRAMs.

Table 5.1: Details of the active layers of various devices and resistive switching characteristics.

NAME	ACTIVE LAYER	SWITCHING TYPE
	TYPE I: REFERENCE DEVICES	
Device A	Bare MoS_2	None
Device B	Bare PVP	None
	TYPE II: BILAYER DEVICE	
Device C	MoS_2 and PVP Bilayer	Bipolar and threshold switching
	TYPE III: COMPOSITE DEVICES	
Device D	PVP with MoS_2 (10 $wt\%$)	Non-memory
Device E	PVP with MoS_2 (20 $wt\%$)	Non-memory
Device F	PVP with MoS_2 (30 $wt\%$)	Threshold switching
Device G	PVP with MoS_2 (40 $wt\%$)	Bipolar switching

5.4 Conclusion

Resistive switching at voltages as low as 0.56 V has been achieved in MoS_2 embedded PVP nanocomposite films of micrometre thickness, and much lower ($< 0.56\ V$) switching voltages could be achieved in micrometre-thick PVP/MoS_2 bilayers. Ultra low voltage resistive switching is essential for low power consumption ReRAMs and futuristic energy-efficient computers. We then showed different conduction and resistive switching behaviour for ReRAM devices characterized by different active layers, namely (a) MoS_2 embedded PVP nanocomposite films and (b) bilayer system of MoS_2 and PVP micron layers. These studies reveal the variety of resistive switching and conduction mechanisms achievable by manipulating the active layer consisting of PVP and MoS_2 for the same set of electrodes. We can conclude that memory behaviour can be induced and manipulated by controlling the nature of the active layer and the amount of MoS_2 dispersed in the PVP nanocomposite.

Chapter 6

Resistive switching memory based on chitosan/ polyvinyl pyrrolidone blend as active layers

6.1 Introduction

Blending polymers is one of the easiest and cost-effective way to tailor the properties of materials. Polymer blends offer good mechanical and electrical properties which are useful in the fabrication of batteries[141–144], fuel cells[145], electrochromic devices[146], and many more. Furthermore, polymer blends are beginning to make their mark in the memory device industry, i.e., in fabricating emerging, computer memory devices called resistive switching memory (ReRAM or RRAM)[147–149]. ReRAMs are memory devices that operate based on the resistive switching principle, first reported by Hickmott in 1962[38]. ReRAMs are fundamentally two-dimensional conductor/active layer/conductor structured devices capable of having two distinct electrically switchable resistive states, i.e., the high resistive state (HRS) and low resistive state (LRS). These resistive states resemble logic “0” and “1”, respectively. Realizing resistive switching (RS) in raw organic/biological materials and their blends can offer ReRAMs some added advantages such as metal-free, flexible, biodegradable, and even transparent memory devices, which are vital for achieving futuristic electronics i.e., green electronics and green computing goals[150]. Several organic materials such as gelatin[43, 106, 107, 123, 151], graphene[43], graphene/gelatin blend[43], chitosan[80, 117], and many more have been used as active layers in various ReRAM modules.

Polyvinylpyrrolidone (PVP) and chitosan are among the widely studied polymers. PVP is a synthetic polymer consisting of 1-vinyl-2-pyrrolidone monomers[64], having and bonds of different lengths[152]. PVP has exciting properties such as solubility in water and other polar solvents[152] and interactive ability with metal ions[153]. On the other hand, chitosan is a biological polymer derived from skeletal structures, such as chitin[62]. Chitosan is a cationic polymer with a good binding affinity with metal ions and other materials such as protein [62]. Both PVP and chitosan are biodegradable and contain less toxins enabling them to find applications in cosmetic, food, medicine industries[62, 64]. PVP blends complexed with other materials have been reported recently in fabricating ReRAMs. Poonguzhali *et al.*[154] demonstrated that chitosan/PVP blends with a $1:1$ chitosan to PVP ratio has superior mechanical properties, and they also showed that increasing the PVP mass in the blend increases the crystallinity. Yeh et al.[155] conducted an FTIR and ^{13}C NMR analysis of the PVP/chitosan blend. Their results showed a shift in pick for the 1:1 PVP/chitosan mass ratio, which suggests chemical bonding, i.e., formation of hydrogen bond between PVP and chitosan. This results in decreased viscosity and hence increased crystallinity. Reaction between chitosan and PVP was confirmed by Grant *et al.* through XPS and Raman analysis[156]. To our knowledge, there has not been any report on resistive switching (RS) in chitosan and PVP blends. Instead, this polymer blend has been used by others to make a substrate for biodegradable ReRAM devices[115]. A study of electrical conduction and RS in chitosan/PVP blend will lead to the discovery of even more chitosan/PVP blend applications. Herein, we report the study of resistive switching in ReRAM devices consisting of chitosan/polyvinylpyrrolidone biocomposite as active layers. The reported ReRAM devices consist of chitosan/PVP blend active layers of chitosan/PVP$= 1 : 3$, $1 : 1$, and $3 : 1$ mass of chitosan to PVP. The active layers are sandwiched between Al and Ag electrodes.

6.2 Experimental details

6.2.1 Solution Preparation

Polyvinylpyrrolidone and chitosan with a combined mass of 1 g were dissolved in 100 ml ultra-purified water to make a solution with 1 $w/v\%$. Three 1 $w/v\%$ solutions, with different chitosan to PVP mass ratios, i.e., 0.25 g chitosan and 0.75 g PVP (1:3), 0.5 g chitosan and 0.5 g PVP (1:1), and lastly 0.75 g chitosan and 0.25 g PVP (3:1) were prepared. One drop of acetic acid was added to each solution to facilitate a fast dissolution of chitosan. All solutions were stirred for about 3 hours at room temperature until homogeneous solutions were obtained.

6.2.2 Device fabrication

We fabricated two sets of sandwich-type devices, i.e., three on aluminium (Al) and three on indium tin oxide (ITO) substrates. A 1.00 mm thick aluminium (Al) sheet (Sigma Aldrich, Prod. No. 266957) and polyethene terephthalate (PET) coated with 0.1 μm thick ITO (Sigma Aldrich, Prod. No. 749729-1EA) were cut and pre-cleaned by sonication (first in acetone for 5 min, then isopropyl alcohol for 5 min, and lastly ultra distilled water for 5 *min*) and used as the substrates. The prepared solutions were each spin-coated on the substrates. The spin coat was programmed for rotation at 2000 *rpm*, then 1800 *rpm*, then 800 *rpm* and lastly, 200 *rpm*. Each spin had a duration of 30 *sec* with 30 *sec* off time between successive spins. After drying at room temperature for at least 24 *hours*, thin films with thickness averaged at $\sim 0.2\ \mu m$ were obtained. Finally, a silver (Ag) paste was applied on the respective active layers to make top electrodes (TE) and dried at room temperature for 48 hours. Six devices classified as Al-based devices, i.e., Al/chitosan+PVP(1:3)/Ag, Al/chitosan+PVP(1:1)Ag, and Al/chitosan+PVP(3:1)Ag, and ITO-based devices, i.e., ITO/chitosan+PVP(1:3)Ag, ITO/chitosan+PVP(1:1)Ag and ITO/chitosan+PVP(3:1)Ag were fabricated.

6.2.3 Device characterization

Atomic force microscope (AFM, Nanosurf FlexAFM) was used to study the surface properties and estimate the active layers' thicknesses using the AFM-step method. Field-emission scanning electron microscope (FESEM, JEOL JSM-7800F) coupled with Energy Dispersive Spectrometer (EDS, Oxford Aztec 350 X-Max80) were used to study morphology and estimate the chemical composition of the composite, respectively. Lastly, the Keysight Source/Measure Unit, (SMU, Keysight B2901), was used to study our fabricated devices' electrical conduction and resistive switching.

6.3 Results and discussion

6.3.1 Morphology characterization

Figure 6.1(a) is a FESEM micrograph (scale= 10 μm) taken for the chitosan/PVP thin film consisting of 1:1 chitosan to PVP. This micrograph shows a possible miscibility between chitosan and PVP solutions, resulting in even effect. Minimal traces of undissolved polymer are also revealed in this micrograph. The corresponding AFM height trace image for this film is shown in Fig. 6.1(b). This image shows a slightly uneven surface with pits and heights up to 6 nm and 7 nm, respectively, while the estimated mean roughness was 0.69 nm indicating fairly smooth surface.

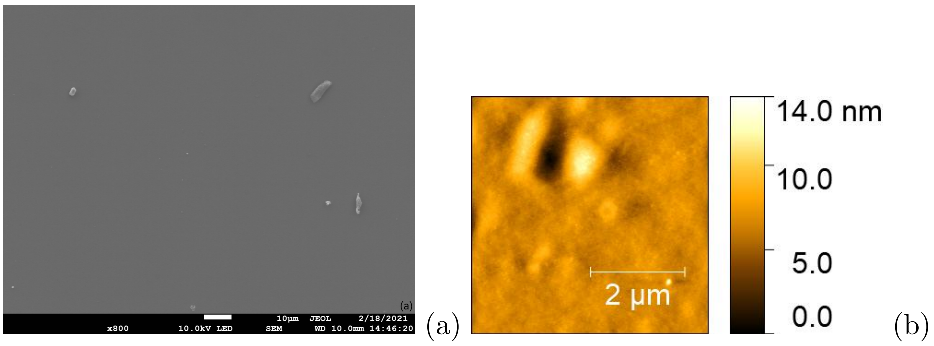

Figure 6.1: (a) the FEG-SEM micrograph and (b) AFM image of the active layer consisting of 1:1 chitosan to PVP ratio.

6.3.2 Electrical conduction and Memory behaviour

Electrical characterization was performed by applying a potential at the top electrode (TE) while the bottom electrode (BE) was grounded. The forming process of each device was studied by increasing the applied voltage from

$0\ V$(using $10\ mV$ steps with $25\ ms$ delay time) while measuring the current in the device until an abrupt increase in current indicating forming occurs. On the other hand, current-voltage (I-V) hysteresis were obtained by full cycle scan, i.e., $0 \to V_{max} \to 0 \to -V_{max} \to 0$, to understand the memory behaviour of the devices. During the measurements, a compliance current, $I_{CC} = 100\ \mu A$ was programmed to protect the device from permanent damage. Electrical and memory behaviour of Al- and ITO- based devices are separately presented in the next subsections.

Al-based devices

Figure 6.2(a-c) shows the I-V curve for the forming process of device Al/ chitosan + PVP(1:3)/Ag (a), Al/chitosan + PVP (1:1)/Ag (b) and Al/chitosan+ PVP(3:1)/ Ag (c). For the Al/chitosan +PVP (1:3)/Ag device, there is no forming observed. Instead, the current remains almost zero, and a slight rise up to about a hundred nano-Ampere begins when the bias voltage reaches $3\ V$ (see inset), accompanied by strong signal noise. For the Al/chitosan+PVP(1:1)/Ag device, the I-V characteristic shows that the current remains zero until the applied voltage reaches $0.7\ V$, where a sudden jump (by $> 10^{-4}\ A$) in current occurs indicating electroforming.

The electroforming I-V characteristic of the Al/chitosan+ PVP(3:1)/Ag ReRAM device is somewhat different. For this device, a weak but linearly increasing current (slope $= 2.87 \times 10^{-6}\ \Omega^{-1}$) is observed in the region $0\ V - 1.08\ V$. Following this, a jump in the current by ten orders of magnitude occurs, and a new linear region with a relatively higher slope ($1.05 \times 10^{-4}\ \Omega^{-1}$) begins. This indicates some kind of electroforming. Our results show that chitosan to PVP mass ratio variation brings about different electroforming process behaviours in our devices.

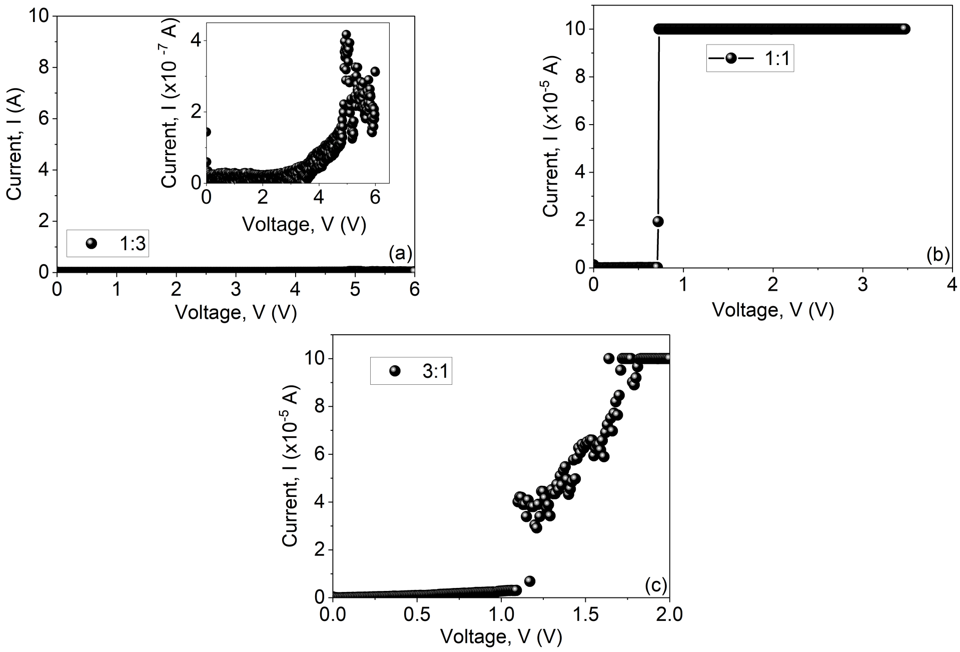

Figure 6.2: Current-voltage curves, showing different electroforming behaviour of the Al/chitosan+PVP/Ag devices consisting of 1:3(a), 1:1(b), and 3:1(c) chitosan to PVP.

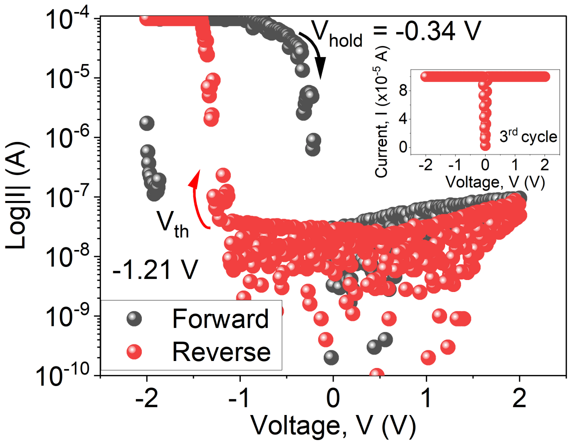

Figure 6.3: Current-voltage characteristics of the Al/chitosan+PVP/Ag ReRAMs with 1:3 chitosan to PVP

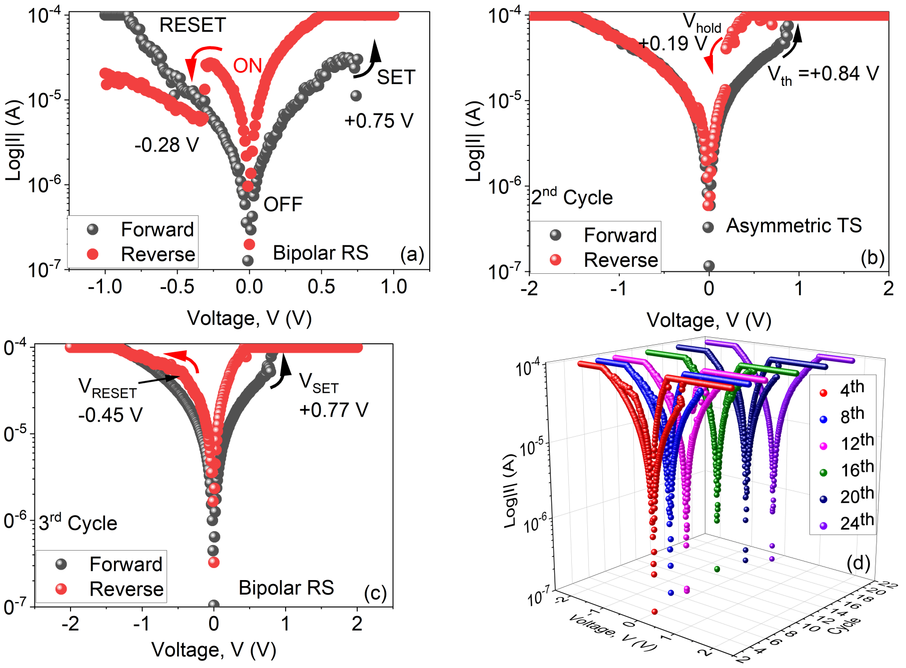

Figure 6.4: Current-voltage characteristics of the Al/chitosan+PVP/Ag ReRAMs with 1:1 chitosan to PVP, showing the first sweeping cycle(a), the second(b), the third(c) and the 4th-24th cycles(d).

Figure 6.3 shows the semi-logarithm I-V graph for the Al/chitosan+PVP (1:3)/Ag device. For this device's first cycle (main image), our data show that in the positive voltage bias, in both the forward and reverse sweeping direction, there is a very weak I-V dependence with significant noise in the current data. In the negative voltage bias, the current still has noise, but clear hysteresis is observed, indicating an asymmetric threshold switching (TS) behaviour with $V_{th} = -1.21\ V$ and $V_{hold} = -0.34\ V$. This device showed an $ON/OFF > 10^3$, which lasted for the first two cycles. Swiping this device for the third cycle (inset) revealed no switching and no hysteresis, indicating loss of memory behaviour.

Figure 6.4(a-d) shows the I-V characteristics of the Al/chitosan + PVP(1:1)/Ag device. In the first voltage sweep cycle(a), this device shows a typical

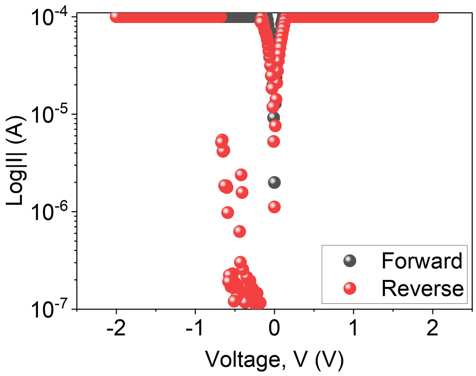

Figure 6.5: Current-voltage characteristics of the Al/chitosan+PVP/Ag ReRAMs with 3:1 chitosan to PVP.

bipolar memory behaviour with impressively low operating voltages, i.e., $V_{SET} = +0.75\ V$ and $V_{RESET} = -0.28\ V$ and an $ON/OFF \geq 10$. Upon sweeping for the second time(b), the I-V variation changed significantly, and an asymmetric TS with $V_{th} = +0.84\ V$ and $V_{hold} = +0.19\ V$ was observed only in the positive voltage bias. Upon sweeping the voltage for the third cycle (c), hysteresis re-emerged in the negative voltage bias, and the LRS-to-HRS switching in the positive reverse sweep direction was not observed for this sweeping cycle, implying that the switching mode has reverted to bipolar switching ($V_{SET} = +0.77\ V$ and $V_{RESET} = -0.45\ V$) with the same ON/OFF ratio. We tested the stability of this memory behaviour, and our data revealed that this bipolar memory behaviour was stable for at least 16 sweeping cycles, as shown in 6.4(d), suddenly the hysteresis degrades and disappears thereafter.

Figure 6.5 shows the I-V characteristics of the Al/chitosan+ PVP(3:1)/Ag device. This device did not show any memory behaviour. We consider the Al/chitosan+PVP(1:1)/Ag device as our optimal results, and thus we shall discuss its conduction mechanism in the section 6.4.

ITO-based devices

In Fig. 6.6, we show the electroforming I-V characteristics of the ITO/chitosan+PVP/Ag devices with (a) 1:3, (b) 1:1 and (c) 3:1 chitosan to PVP ratio. The current follows a linear variation with the applied voltage, indicating no electroforming in devices having 1:3 and 1:1 ratios. On the other hand, the device with a 3:1 chitosan to PVP ratio show electroforming at $V_{form} = 5.5\ V$. We analyzed the memory behaviour of these devices.

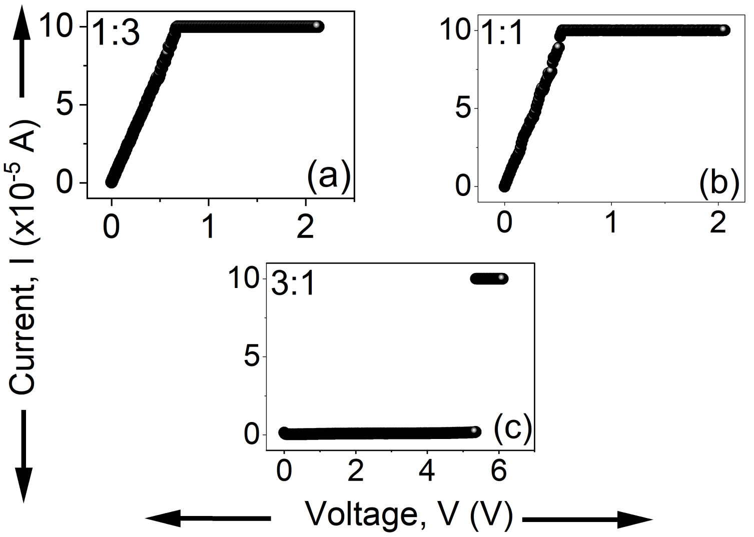

Figure 6.6: Current-voltage curves, showing different electroforming behaviour of the ITO/chitosan+PVP/Ag devices consisting of 1:3(a), 1:1(b), and 3:1(c) chitosan to PVP.

Figure 6.7 shows the log-log I-V graph of the ITO/chitosan+PVP(1:3)/Ag device. Our data do not reveal any hysteresis during the first voltage scan (see the main figure). We increased the I_{CC} and found a weak asymmetric hysteresis with $ON/OFF \approx 2$ when the I_{CC} was 0.005 A, as shown in the inset. This hysteresis is very weak, and therefore we conclude that this device does not have memory behaviour. We further analyzed the behaviour of this device by plotting the forward sweep current for the positive voltage

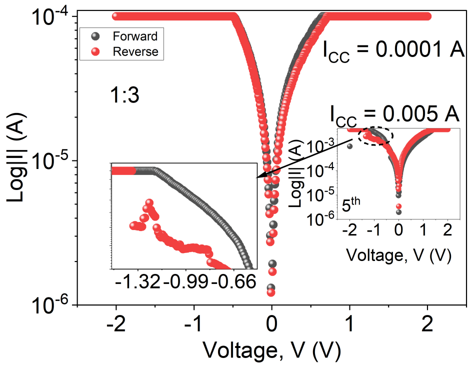

Figure 6.7: Current-voltage characteristics of the ITO/chitosan+PVP/Ag ReRAMs with 1:3 chitosan to PVP. The inset shows the 5^{th} scan cycle with $I_{CC} = 0.005\ A$.

bias, see Fig. 6.8. We swept the voltage twice for each I_{CC} value (0.0001 A, 0.0005 A, 0.001 A and 0.005 A). The I-V graphs obtained seem to be linear at low I_{CC} values, i.e., 0.0001 A, as shown in the inset. However, the current

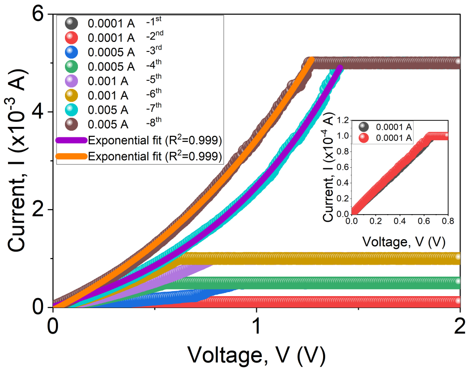

Figure 6.8: I-V graphs for the ITO/chitosan+PVP(1:3)/Ag device showing 1^{st} to 8^{th} voltage scans at increasing I_{CC}. The inset shows the 1^{st} and 2^{nd} cycles at 0.0001 A

.

trajectory deviates from linear and follows an exponential trajectory as the I_{CC} increases. We also noticed that the current during the first and second sweeps does not follow the same path, such that, during the second sweep at the same I_{CC} the system seem to have improved in conductivity. This is more prominent at high I_{CC} values. At high I_{CC}, the the data could be fitted well with the hopping conduction expression[49]:

$$I = I_0 + A \exp\left[(V - Va)/kT\right] \tag{6.1}$$

where I_o, A, V_a and k respectively the residual current, the product of mean hopping distance, number of electrons and thermal vibrational frequency of electrons at the trap and the characteristic voltage, which relates to the activation energy, and lastly the Boltzmann constant[49]. Therefore for this device, our data reveal two critical observations, i.e., (1) an increase in slope and (2) a transformation from linear to exponential behaviour of the I-V data. However, at this time, it is not clear if these two changes are I_{CC}- or voltage scan-dependent. Figure 6.9 (main figure) shows the semi-log graph for the ITO/chitosan+ PVP(1:1)/Ag device. Also, for this device, our data reveal no memory behaviour even after increasing the I_{CC} to 0.0005 A, as shown in the inset. Again, we analyzed the current behaviour of this device by plotting the I-V data on the log-log scale in Fig. 6.10 (a). This graph indicates Ohmic behaviour, $I \propto V$, as $n = 1$. Figure 6.10(b) shows the variation of slopes for the first three consecutive cycles. Again, a wide slope difference, i.e., 2.37×10^{-4} A and 9.60×10^{-4} A at different I_{CC} values, i.e., 0.0001 A and 0.0005 A, respectively. At the same time, our data shows slight increase in slopes, i.e., 9.60×10^{-4} A and 1.04×10^{-3} A at similar (0.0005 A) I_{CC} values. For this device, our results confirm that both the scanning act and I_{CC} play a role in increasing the slope. Likewise, the ITO/chitosan+ PVP(3:1)/Ag device did not show any significant hysteresis during the first cycle and even when the I_{CC} was increased up to 0.0005 A as shown in Fig. 6.11.

In comparison, our results show that all ITO-based devices do not have memory characteristics, while some Al-based devices have promising mem-

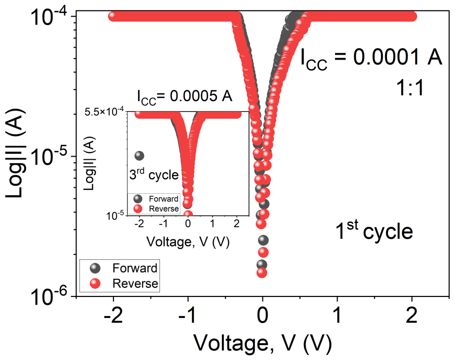

Figure 6.9: Current-voltage characteristics of the ITO/chitosan+PVP/Ag ReRAMs with 1:1 chitosan to PVP.The inset shows the 3^{rd} scan cycle with $I_{CC} = 0.0005\ A$.

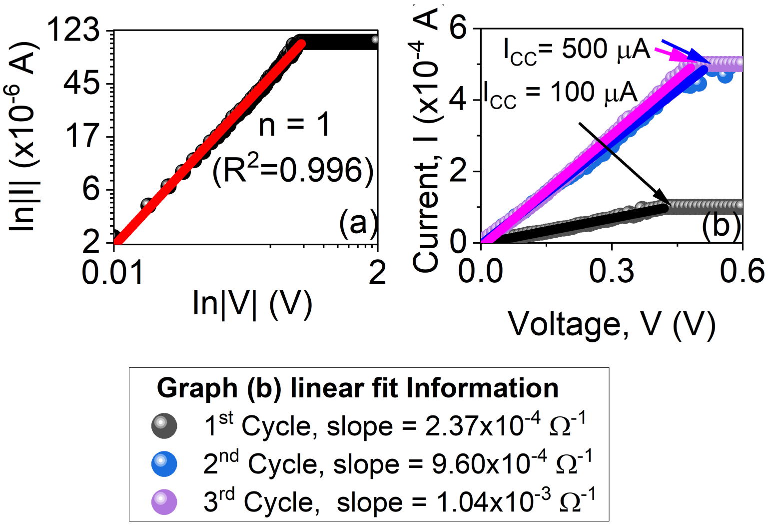

Figure 6.10: The I-V characteristics of the ITO/chitosan+PVP/Ag ReRAM with 1:1 chitosan to PVP ratio showing (a) the In—I—-In—V— curve fitting. (b) shows linear fitting of data for the first three consecutive scan cycles.

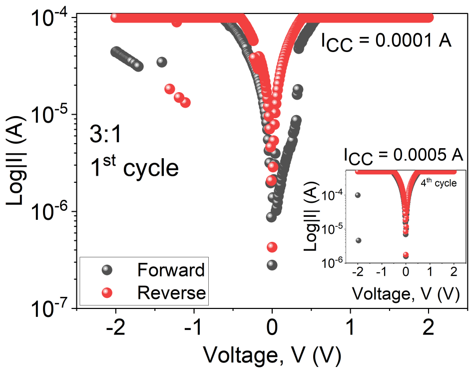

Figure 6.11: Current-voltage characteristics of the ITO/chitosan+PVP/Ag ReRAMs with 3:1 chitosan to PVP.The inset shows the 4^{th} scan cycle with $I_{CC} = 0.0005\ A$.

ory prospects. This observation reveals essential information about the role of the Al BE in this experiment. We argue that Al and ITO electrodes introduce electrode/active layer, i.e., Al/chitosan+PVP and ITO/chitosan+PVP interfaces having different properties in our systems. These interface properties strongly affect the switching in our devices. A similar observation has been reported in the literature. For example, Do *et al.* [157] reported a drastic change in switching behaviour in the $Al/TiO_2/Pt$ system when the electrodes are interchanged, i.e., when Al is used as BE $(Pt/TiO_2/Al)$. They attributed their results to a change in trapping/detrapping of charge due to the difference in the interface, which affects the redox reaction. Similarly, Ghosh et al. conducted an intensive study of $Pt/TaO_x/Pt$, $Cu/TaO_x/Ti$, $Cu/TaO_x/Ta$, $Ta/TaO_x/Pt$, and $Ti/TaO_x/Pt$ systems. They found the best performance with $Ti/TaO_x/Pt$ system. Similarly, Al-Mamun *et al.* proved that Ru showed better performant than Pt in the TaO_x based ReRAM. Recently, Dlamini *et al.*[117] reported a similar effect in the organic ReRAM system. They replaced the Al BE with ITO in ReRAM that used CdTe/CdSe core-shell quantum dots incorporated chitosan as an active layer. Their results demonstrated increasing conductivity, leading to exponentially diminishing I-V hysteresis in the ITO-based system, while the Al-based system showed sustainable memory behaviour[117]. The latter results are in agreement with our observation.

6.4 Switching mechanism in Al/chitosan+PVP(1:1) /Ag device

The switching mechanism in ReRAM devices is still a challenging topic as many systems show different switching characteristics. However, several switching mechanisms have been proposed and used to describe the switching behaviour in various systems. Typically, resistive switching mechanisms can be classified into interfacial, i.e., electrode dependent and filament, i.e., bulk limited mechanisms. Interfacial mechanisms include Schottky emission, Fowler-Nordheim tunnelling, Direct tunnelling, and Thermionic-field emission. In contrast, filament mechanisms are Poole-Frenkel mission, Hopping conduction, Ohmic conduction, Space-charge-limited conduction, Ionic conduction and Grain-boundary-limited conduction[41, 48, 120]. A critical analysis of the I-V data is needed to understand which mechanism is possible. One way is by replotting the I-V data on the log-log scale and determining the value of n, satisfying the relationship $J \propto V^n$. The value of n carries critical information pointing towards the possible mechanism. We re-plotted Fig. 6.4(c) on log-log scale as shown in Fig. 6.12. Figure 6.12 shows that the current in both OFF- and ON-states follows a linear ($n = 1$) variation with the applied voltage. Together with the forming behaviour of this system, these results point towards filament-driven switching, where the SET and RESET switching is due to the formation and rapture of nanoscale conductive filaments (CF). Different mechanisms may lead to the formation of CF in organic ReRAMs. In the case where an electrochem-

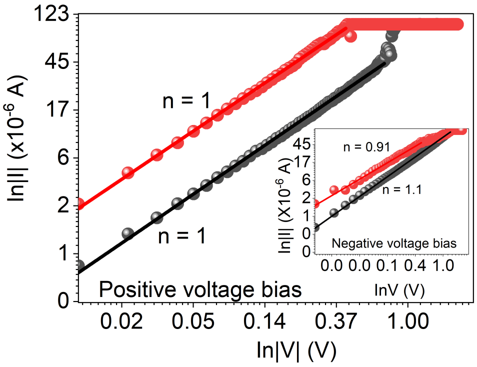

Figure 6.12: lnI againts *ln*V graph fitting of the Al/chitosan+PVP/Ag ReRAMs with 1:1 chitosan to PVP. This graph is a replot of Fig. 6.4c.

ically active electrode such as Ag (or Cu) is used, application of the voltage at the electrodes may cause oxidation of Ag ($Ag \rightarrow Ag^+ + e^-$) into Ag^+ ions[158]. A strong electric field can drive these Ag^+ ions through the active layer, leading to a current[158]. When the Ag^+ ions reach the other electrode, which has an excess of electrons, these ions may undergo reduction ($Ag^+ + e^- \rightarrow Ag$) and form a pile of Ag atoms, leading to nanoscale conduction filament (CF) that grows towards the TE and ultimately short-circuits the cell, leading to a high jump in current[159] during the electroforming process. The application of voltage with different polarities reverses or facilitates the redox reaction leading to partial rapture or reformation of the CFs during the RESET and SET processes, respectively. Likewise, CF in metal oxides can be formed by oxygen vacancies or oxygen ions migration through the active layer. Because our devices consist of organic active layer and the electroactive Ag TE, the formation of CF due to diffusion of Ag^+ ions is a strong possibility.

6.5 Conclusion

In summary, we investigated resistive switching in ReRAM devices that use chitosan and polyvinylpyrrolidone blend active layer sandwiched between aluminium and silver electrodes. First, bipolar, then asymmetric threshold switching, followed by bipolar memory behaviour, driven by formation and rupture of conductive filaments were observed in the same device consisting of chitosan/PVP with mass ratio 1:1, while no memory was demonstrated when chitosan/PVP ratios of 1:3, and 3:1 were used. We replaced the Al bottom electrode with indium doped tin oxide electrode and observed no switching. Instead we observed sweeping cycle- and compliance current- dependent decrease in resistance accompanied with change from linear to exponential current-voltage behaviour when compliance current is increased.

Chapter 7

Resistive Switching Memory-Based on Raw Cow Milk

7.1 Introduction

Environmentally friendly and low power computing devices are vital for the realization of the green computing world. Emerging memory technology based on the resistive switching (RS) principle can be fabricated using biodegradable materials, and they have low power consumption prospect[50]. These memory devices, known as resistive switching memories (ReRAMs or RRAMs), are fundamentally two-terminal and two-dimensional devices, consisting of an organic[43, 54, 80], organic-inorganic hybrid[21], metal oxide[96], or any suitable materials[40, 46, 48] sandwiched between a top electrode (TE) and a bottom electrode (BE)[46]. By applying an electric stimulus, the resistance of this device can be switched from a high resistive state (HRS) to a low resistive state (LRS) during the SET process, or from LRS-to-HRS, during the RESET process[22]. The HRS, often called the OFF-state and LRS, often called the ON-state, are analogous to binary codes ’0’ and ’1’, allowing ReRAMs to comply with digital technology. Furthermore, the architect's omission of a driving transistor gives ReRAMs advantages such as reduced cell size and reduced heavy metal footprint. In addition, ReRAMs fabricated using organic or biological materials may have reduced toxicity and superior mechanical properties for futuristic electronics such as flexibility, transparency, and lightweight[22, 58, 63, 160]. Although tremendous progress has been made in discovering and optimizing RS in various systems, understanding RS's driving conduction mechanism is still a research topic. Space-charge limited conduction (SCLC) mechanism is by far the most reported RS mechanism in organic materials, such as chitosan, Aloe vera, gelatin, graphene, and other complexed systems such as CH3NH3PbI3xClx[161]. As far as we can ascertain, there has not been any report of RS in raw cow milk, except our own preliminary results obtained using the spin coat fabrication method[162]. Here, we report the first resistive switching memory based on raw cow milk as active layers fabricated in an electrical and heat energy-free fabrication method.

7.2 Experimental Details

Our ReRAM devices were fabricated by the direct dipping (or dip coat) method. First, rectangular pieces of indium doped tin oxide coated polyethylene terephthalate (PET-ITO) (Sigma Aldrich, Prod. No. 749729) were used as the substrates. After pre-cleaning, the PET-ITO substrates were momentarily separately immersed into fat-free(S1), medium fat(S2) and full cream(S3) organic homogenized cow milk. Then, the substrates were gently taken out and carefully placed on a horizontal surface with the ITO sides facing up and left to dry at the ambience for 24 hours. Next, silver (Ag) paste (Sigma Aldrich, Prod. No. 735825) was applied on top of each milk film to form electrodes. The devices were left for further 48 hours at the ambience to allow the Ag paste to completely dry. Thus, complete devices have the notation: PET-ITO/Cow-milk(S1)/Ag, PET-ITO/Cow-milk(S2)/Ag and PET-ITO/Cow-milk(S3)/Ag. The ITO layer and Ag acted as bottom electrodes (BE) and top electrodes (TE), respectively. Figure 1(main figure) shows the schematic diagram typifying the fabricated devices, while the insets (a) and (b), respectively, show the actual photograph of one of the devices and the cross-sectional image showing the estimated thickness.

For characterization, a field emission gun scanning electron microscope (FEG-SEM) (ZEISS Ultra Plus) was used to study the morphology of the active layers. Next, the thickness and elemental composition were estimated using the field-effect scanning electron microscopy (FESEM, JEOL JSM-7800F) equipped with an energy-dispersive X-ray spectrometer (EDS, Oxford Aztoec 350 X-Max80). Finally, an atomic force microscope (Nanosurf, FlexAFM) was used to study the surface properties of the active layers. The electric transport and switching study on all devices were conducted at room temperature using the source/measure unit (SMU) (Keysight, B2901A series), connected as shown in the simplified circuit diagram in Fig. 7.1(Main figure).

7.3 Results and Discussion

7.3.1 Morphology and Topography

Our experiment showed that the cow milk film robustly binds with the ITO surface, forming a stable film even after bending, as shown in Fig.7.1 inset(a). The EDS results (Fig. 7.2) reveal the typical milk constituent elements, i.e., sodium (Na), magnesium (Mg), phosphorus (P), potassium (K), chlorine (Cl), and calcium (Ca) and no traces of contamination in the

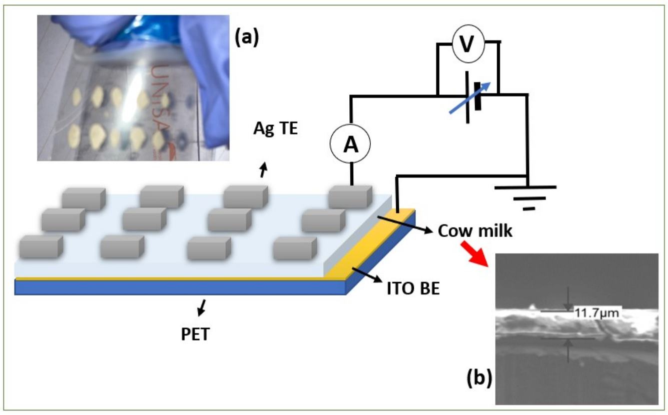

Figure 7.1: The main figure shows the schematic diagram of a typical PET-ITO/cow milk/Ag ReRAM device connected to a simplified current-voltage measurement circuit. The insets show (a) the actual photography of the PET-ITO/Cow milk(S2)/Ag ReRAM and (b) the cross-sectional FESEM micrograph of the S2 active layer.

films were found. Other elements such as carbon (C) and oxygen (O) might be due to the organic compound(s) contained in the milk, and the high peak of carbon is due to the carbon coating during the EDS sample preparation. The nitrogen atom detected might be due to the protein constituent of the milk or may have been absorbed from the sample chamber environment.

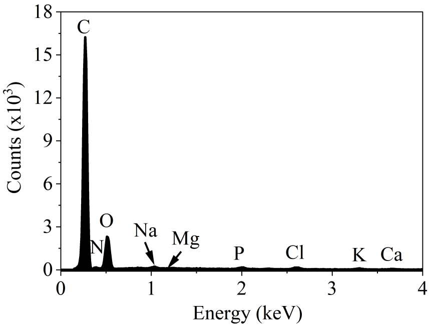

Figure 7.2: EDS spectrum of typical cow milk.

In Fig. 7.3(a, c and e) we show the 1 μm1 μm FEG-SEM microstructures of the fat-free, medium fat and full-cream cow milk films, respectively. These microstructures reveal small fat globules in the medium cream milk film and these fat globules are even more prominent in the full cream cow milk's micrograph. These fat microstructures are absent in fat-free cow milk; instead, tiny void spaces are visible. The AFM topography images for the fat-free, medium fat and full cream milk films are shown in Fig. 7.3(b, d and f), respectively. These AFM results reveal significantly different surface characteristics in each of these films. The fat-free film is more characterized with pits as deep as 0.54 μm found all over the surface. In contrast, the medium cream and full cream milk films show less visible pits. The estimation of roughness revealed mean roughness of 87.7 nm, 28 nm and 56 nm estimated for the fat-free, medium fat and full cream films. We believe that fat-free milk consists of high-water content than the other films. As such, when the film is dried, the water evaporates and leave behind voids which cause the high roughness as depicted by the AFM results. On the other hand, the full cream milk film consists of relatively high fat and low water content; when this film is dried, the fat remains and constitute the film's morphology. Similarly, the somewhat smoother surface of the medium cream cow milk film is attributed to the just-right amount of water and fat in the film. Lastly, the FEG-SEM measurement of the cross-section of the films revealed a thickness estimation of 11 μm.

7.3.2 Electrical Transport and Memory Study

Electrical measurements of all our devices were performed at room temperature by applying voltage stress at the Ag TE while the ITO BE was grounded. The voltage was varied while simultaneously measuring the current through the device. Electroforming behaviour was probed by increasing the voltage from 0 V using 10 mV steps with 25 ms delay until forming oc-

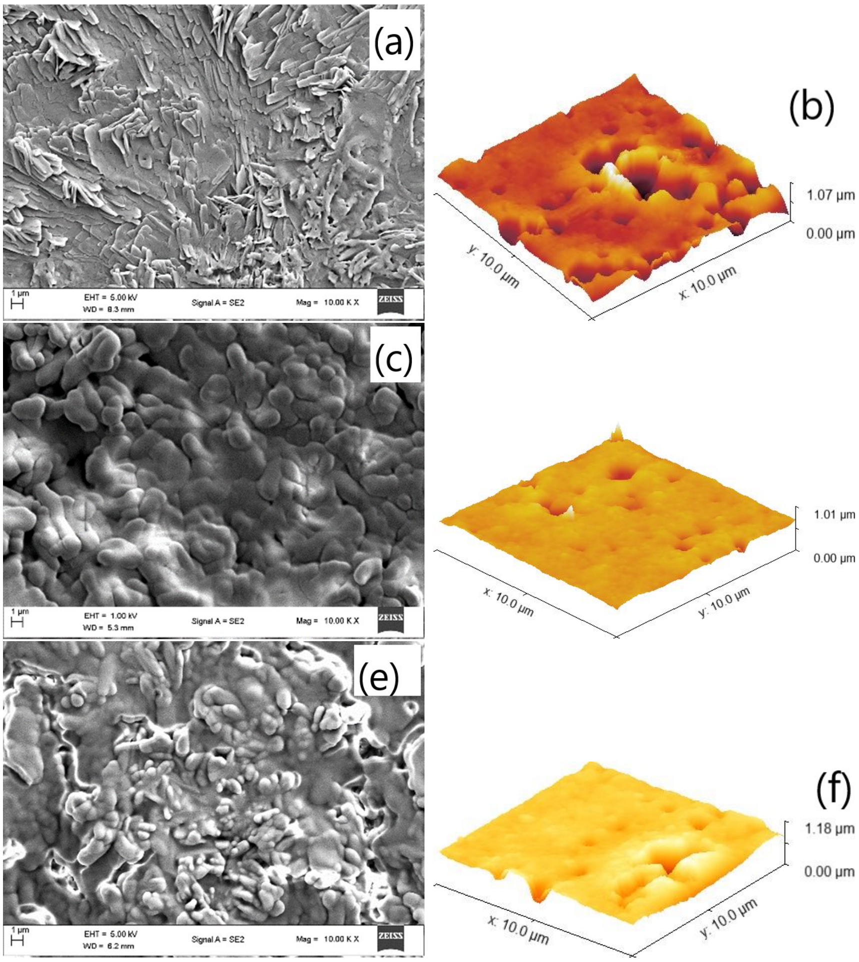

Figure 7.3: FEG-SEM micrographs of (a) fat-free (S1), (c) medium cream (S2), and (e) full-cream (S3) cow milk films. On the same image, (b), (d) and (f) show the AFM topography images of the fat-free, medium cream and full cream cow milk, respectively.

curs. The memory behaviour was investigated in the same way, but this time, a complete scan, i.e., $0 \rightarrow +V_{max} \rightarrow 0 \rightarrow -V_{max} \rightarrow 0$ was performed. A compliance current (I_{CC}) of 100 μA was applied to protect the devices from permanent damage[117]. The current-voltage (I-V) curve showing the forming process of the PET-ITO/cow-milk(S1)/Ag device is shown in Fig. 7.4(a). For this device, the current remains zero until the voltage reaches 8.22 V. At this voltage, the current jumps by $> 10^4$ orders of magnitude. This indicates that the device is undergoing electroforming. The full circle llog $|I| - V$ graph depicting the memory characteristics of this device is shown in Fig. 7.4(b). Here, the current does not follow the same paths during the forward and reverse voltage scans, thus creating a hysteresis. Different kinds of hysteresis are associated with memory, i.e., an 'N-type', 'S-type' and 'O-type' hysteresis[45]. The 'N-type' and 'S-type' hysteresis are characterized by a sharp increase and decrease in current at specific voltages. At the same time, smooth transitions from HRS-to-LRS and LRS-to-HRS represent the 'O-type' hysteresis. Therefore, even though there are jumps in current at points marked a-d, we classify this memory type as 'O-type' bipolar memory behaviour. Even though the memory behaviour in this device quickly vanished during the third sweeping cycle, as shown in Fig. 7.4(c), this device showed remarkably low (> 1 V) voltage switching and a reasonable ON/OFF ratio of $\geq 10^2$ making it suitable as a write-once read many (WORM) memory device[11].

In Fig. 7.5 we show the I-V characteristics of the PET-ITO/cow milk(S2)/ Ag device. The I-V graph for the forming curve is shown in Fig. 7.5(a). Our data shows that the current first follows a linear path and suddenly drops at 0.59 V. It stayed in the range of 2×10^{-5} A for the voltage range 0.59 $V - 0.93$ V, after which it abruptly jumps to $> 10^{-4}$ A. We believe that the event at 0.93 V is the forming process. The memory characteristics of this device shown in Fig. 7.5(b). From this graph, one can distinctively

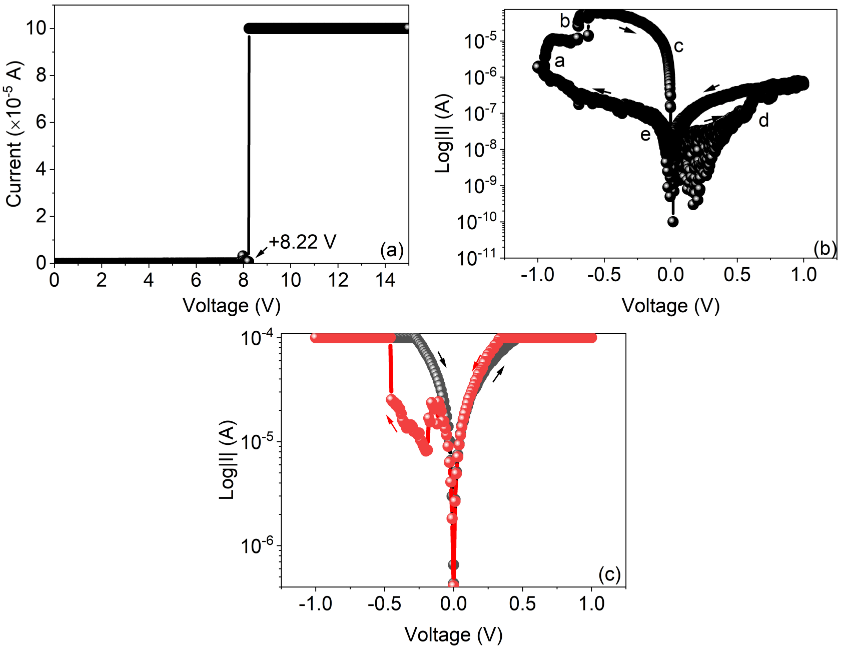

Figure 7.4: I-V characteristics of the PET-ITO/cow milk(S1)/Ag device, showing (a) the forming curve, (b) the first and (c) the third sweeping cycle.

identify points where the trajectory of the current change in both the positive and negative voltage bias. Thus we classify this memory behaviour as asymmetric 'S-type' bipolar memory behaviour[45]. These distinctive transitions occur at $V_{SET} = +0.48\ V$ and $V_{RESET} = -0.25\ V$. Additionally, the memory behaviour was sustainable for at least thirty write and read cycles, as shown in Fig. 7.5(c). Therefore, even though this device has a weak (≥ 10) ON/OFF ratio, it offers excellent low power device prospects and applicability as nonvolatile memory.

Lastly, Fig. 7.6 shows the I-V characteristics of the PET-ITO/cow milk(S3)/Ag device. The forming process I-V graph is shown in Fig. 7.6(a). Our data shows no forming, as the current follows an exponential trajectory and does not show any abrupt increase. The log—I—-V variation (Fig. 7.6b) showing the memory characteristics of this device reveals a typical 'O-type'

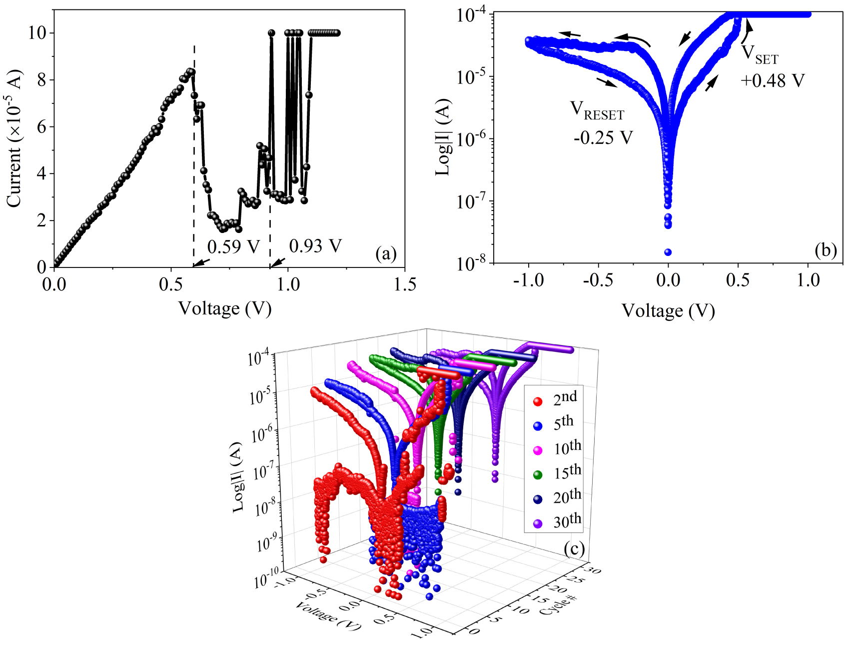

Figure 7.5: I-V characteristics of the PET-ITO/cow milk(S2)/Ag device, showing (a) the forming curve, (b) the first and (c) the first 30 sweeping cycles.

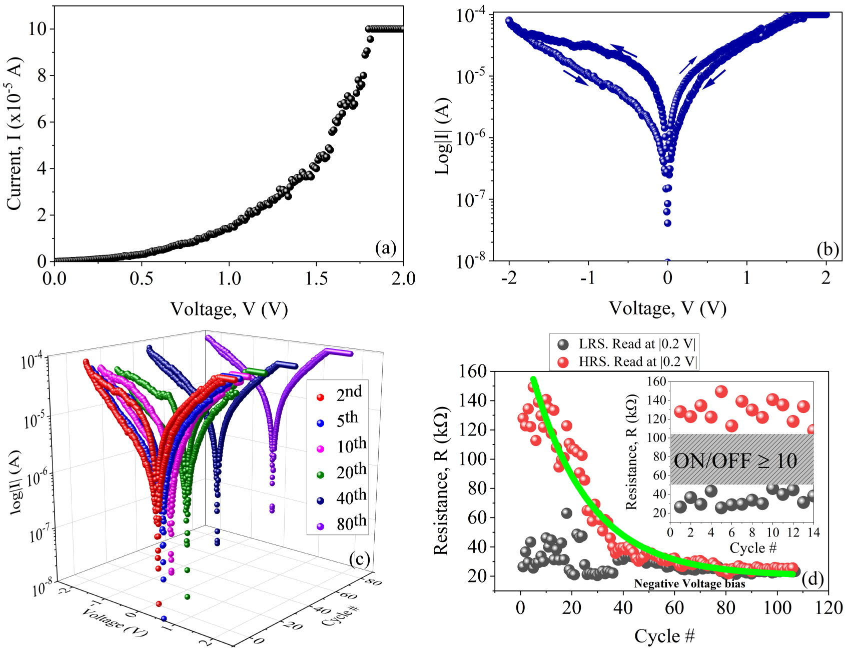

Figure 7.6: I-V characteristics of the PET-ITO/cow milk(S3)/Ag device, showing (a) the forming curve, (b) the first and (c) the first 80 sweeping cycles. (d), on the other hand, shows the resistance-number of sweeping cycle.

hysteresis[49], lying between $-1.70\ V$ and $+0.70\ V$. This 'O-type' memory behaviour has $ON/OFF \geq 10$ and was sustained for over 14 write/erase cycles as shown in Fig. 7.6(c and d). As shown in Fig. 7.6(d) after the 14th cycle, the resistance of the cell started to decrease exponentially, and the HRS and LRS states began to coincide at the 37th cycle. This decrease in ON/OFF ratio indicates diminishing memory behaviour.

Comparatively speaking, our data reveal different forming and memory behaviour in devices that use S1, S2 and S3 active layers. This may be attributed to the fat content or different weight percentages of the metallic ions in these active layers. In the following subsection, we shall analyze the conductive mechanism in all the devices.

7.4 Conduction Mechanism Analysis

Various conduction mechanisms classified as (1) electrode dependent, i.e., non-filament conduction: Schottky emission, Fowler-Nordheim (F-N) tunnelling and direct tunnelling, thermionic-field emission (2) bulk dependent, i.e., filament conduction: Ohmic, Poole-Frenkel (P-F) emission, the space-charge limited current (SCLC), hopping conduction and trap- assisted- tunnelling (TAT), ionic conduction and grain- boundary- limited conduction have been reported in the literature[41, 49, 51]. We shall analyze our results against these conduction mechanisms. Fig. 7.7(main figure) is the I-V curve fitting of the PET-ITO/cow-milk(S1)/Ag device. The LRS current (red graph) follows a linear variation (with $slope = 8.0 \times 10^-7\ \Omega^-1$) with the applied voltage. For this curve, we estimated the value of n satisfying the relationship $J \propto V^n$ by plotting the data in log-log scale as shown in the inset. The analysis of the slope shows that $n = 1$, which implied that the LRS follows Ohms law, $I \propto V^n$, $n = 1$[49]. It is common for the LRS current to follow the Ohmic behaviour[41] as this indicates the formation of conduction filaments (CF). However, different mechanisms may lead to the formation of the CF; therefore, a critical analysis of the HRS current is essential. The HRS current data (black curve) fitted well with the exponential function for the hopping conduction[49]:

$$I = I_0 + A \exp\left[\frac{(V - V_a)}{kT}\right] \tag{7.1}$$

Here, I_0 is the residual current, and according to Chiu[120], $A = qa\nu$ (a, n and ν are respectively the mean hopping distance, the electronic concentration in the conduction band of the dielectric, and the frequency of thermal vibration at trap sites). V_a is the characteristic voltage which re-

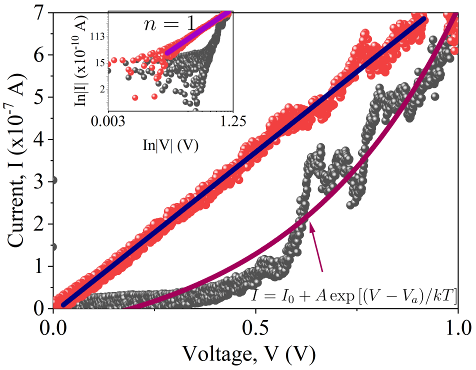

Figure 7.7: The I-V fitting (main figure) and lnI-lnV fitting (inset) of the PET-ITO/cow milk(S1)/Ag device.

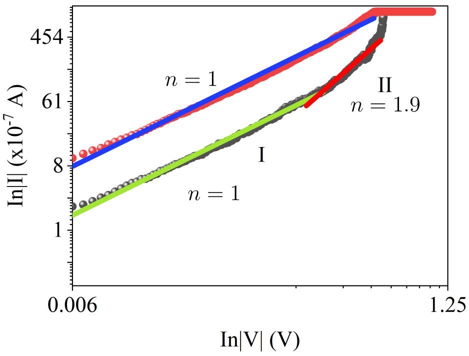

Figure 7.8: The lnI-lnV fitting of the PET-ITO/cow milk(S2)/Ag device.

lates to the activation energy, k is the Boltzmann constant and lastly, T is the temperature in Kelvin[49],

In Fig. 7.8 we show the $\ln I - \ln V$ fitting of the PET-ITO/cow-milk(S2)/Ag device. Here, the LRS current of this device also follows Ohmic conduction as deduced by estimating the value of $n = 1$. The HRS current, however, shows two distinctive regions with $n = 1$ (region I) and then $n = 1.9 \sim 2$ (region II). The current in region II, therefore, follows a power law given by the Mott-Guyner equation given by Eq. (2)[45, 117].

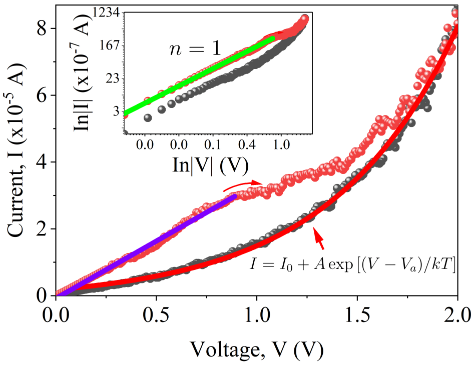

Figure 7.9: The I-V fitting (main figure) and InI-InV fitting (inset) of the PET-ITO/cow milk(S3)/Ag device.

$$J = \frac{9\mu\epsilon\theta V^2}{8D^3} \tag{7.2}$$

where μ is the mobility, is the permittivity of the active layer, θ is the ratio of the free and trapped charge, and D is the thickness of the active layer[118]. The occurrence of linear followed by power-law conduction indicates a well-known space-charge limited conduction mechanism (SCLCM). Therefore, SCLCM drives the formation of CF in this device.

Lastly, we analyze the conduction mechanism of the PET-ITO/cow-milk(S3)/Ag device. The I-V fitting of this device is shown in Fig. 7.9. The HRS current (main figure) fits well with the exponential function while the LRS before switching follows a linear path. This linear relationship is Ohmic ($n = 1$) as confirmed by the log-log plot shown in the inset. For this device, we can also conclude that hopping conduction is the driving mechanism for the formation of the CF.

All our devices use electrochemically active Ag TE. It is well known that when a strong voltage is applied at the Ag electrode, electric field-driven migration of Ag^+ ions takes place, thus generating the current. These ions can be reduced at the BE and create a pile of Ag atoms which ultimately form conductive filaments (CF) which short circuits the device, causing a switch from HRS to LRS during the SET process[163]. In our case, however, all our devices consist of Ag and ITO electrodes and yet behave differently. This suggests that the formation of CF is due to another mechanism other than Ag^+ ion migration. To get an insight into the possible transport mechanism, we critically compare the three active layers. In Tab. 1 we show the summary of the metallic elements found in the active layers used in this study. The table reveals that S2 has the highest weight percentage ($wt\%$) of metallic atoms, i.e., Na, Cl, K, Ca and Cu compared to S1 and S3, with S1 showing the absence of some elements such as K and Cu. Therefore, we believe that as we applied a positive voltage at Ag TE and a negative voltage at ITO BE, electron accumulation takes place at the ITO electrode. These electrons eventually gain enough energy to tunnel through the ITO/milk interface into the active layer and thus creating a current. Our data, however, show a strong dependence of current trajectory to the $wt\%$ of the metallic (M^{n+}) ions. Therefore, it is possible that in the active layer, which has a low $wt\%$ of M^{n+} ions, a strong electric field enables electrons to hop from the electrode to the nearest ion, from the ion to the following ion, and lastly from the ion to the Ag TE. While that is happening, electrons can be absorbed into the vacancies, thus turning ions into metal atoms in a reduction process ($M^{n+} + ne^- \rightarrow M$). This may result in formed metallic particles aligned in the electric field direction, thus acting as weak CF, which constitute the Ohmic behaviour observed in the LRS current in devices with S1 and S3. On the other hand, in the S2 system, where more metallic ions are present, a weak electric field may be sufficient to slightly drive the nearby M^{n+} ions towards the ITO electrode where these ions can be reduced to form metal atoms. This constitutes the linear current behaviour. High voltage creates an electric field that drives some electrons to pore into the active layer, thus creating a power increasing current given by Eq. (2). To compare our findings with the already reported results in the literature, we present (Tab. 2) a summary of the memory devices parameters achieved using some of the raw biological materials. Our Ag/cow milk(S2)/ITO device shows the lowest (0.25 V) switching voltage which surpasses the $< 0.6\ V$ of the lactose which also uses Ag and ITO electrodes[116], and gets near the 0.1 V record set by the $CH_3NH_3PbI_3$ organic ReRAM[158]. We attribute such low operating voltage to the already present metallic ions in the milk film. From the same table, we also show that the switching mechanism in these raw bio-ReRAM devices is mainly SCLCM.

7.5 Conclusion

In summary, we fabricated a resistive switching memory device using fat-free, medium cream and full cream raw organic cow milk as active layers. As for highlights to our results, we observed switching at voltages as low as 0.25 V, making our devices operate as low power memory devices. Low power devices are essential for futuristic and environmentally friendly electronics. Also, we demonstrated that different amount of fat and metallic elements content of cow milk plays a role in the morphology, transport and switching. A medium-fat cow milk device showed better morphology and memory behaviour than the fat-free and full cream milk-based devices. Lastly, hopping conduction driven conducting filaments were attributed to the electric transport mechanism in fat and full cream devices. In contrast, space-charge limited driven conductive filaments were attributed to the mechanism in medium-fat cow milk-based device. Our results further show that the cow milk-based ReRAM device's performance lies strongly on the intrinsic metallic ions found in the milk. Thus, for further optimization

Table 7.1: The comparative summary of metallic element content from the EDS data, switching type, and conduction mechanism of fat-free, medium fat and full ream raw cow milk-based active layers.

Active layer	Estimated element content ($wt\%$)					Switching type	Conduction mechanism
	Na	Cl	K	Ca	Cu		
Fat-free	0.44	0.51	-	0.67	-	'O-type'	Hopping conduction
Medium cream	2.37	4.72	7.42	5.07	1.08	'S-type'	SCLC
Full cream	0.31	0.88	1.13	0.91	0.42	'O-type'	Hopping conduction

Table 7.2: Summary of important memory device parameters of some bare organic/biological material based ReRAMs.(CBCM-Conductive-bridge filament conduction mechanism.)

Device	Operating Voltage (V)	ON/OFF Ratio	Retention (s)	Endurance (cycles)	mechanism	Ref
Ag/cow milk(S2)/ITO	0.25	~ 10	No report	¿30	SCLCM	This work
Ag/-lactose/ITO	0.6	No report	5000	100	SCLCM	[19]
Mg/albumen/W	1	10^2	10^3	10^2	SCLCM	[32]
Ag/eggshell/FTO	1.12	10^3	10^3	No report	SCLCM	[33]
Au/DNA/Au	0.73	10	10^6	10^2	SCLCM	[34]
Mg/gelatin/W	2.16	10^2	10^4	10^2	SCLCM	[35]
Ag/fibroin/Au	0.7	10^5	10^4	30	SCLCM	[36]
Au/starch/ITO	0.9	10^3	10^4	No report	SCLCM	[37]
Ag/Banyan leaves/Ti	1	50	10^3	No report	SCLCM	[38]
Ag/Lotus leaves/ITO	3	40	10^3	> 70	$CBCM$	[39]
Ag/Aloe Vera/ ITO	0.75	10^4	$> 10^4$	10^2	$CBCM$	[3]

conductive nanoparticles can be dispersed in the milk to tailor its applicability in ReRAM technology.

Chapter 8

Conclusion

In this dissertation, we have demonstrated the fabrication of emerging memory devices called resistive switching memory (ReRAM) using biodegradable materials such as chitosan, polyvinylpyrrolidone, and cow milk. Realization of memory application in these materials helps save the earth from the stip rise of environmental pollution. Additionally, our fabricated devices demonstrated low operating voltages, which is essential for low power devices as the world's demand for green electronics and green computing increases.

Chapter 3 reports on the resistive switching and conduction mechanisms in devices consisting of CdTe/CdSe core-shell quantum dots embedded chitosan composites active layer. Two devices with active layers sandwiched between (1) Al and Ag and (2) ITO and Ag electrodes were studied. Both devices exhibited bipolar memory behaviour with $V_{SET} = +1.32\ V$ and $V_{RESET} = -0.92\ V$, for the Al-based device, while $V_{SET} = +0.70\ V$ and $V_{RESET} = -0.82\ V$ were observed for the ITO based device, enabling both devices to be operated at low powers. However, the switching mechanisms of both devices were different, i.e., RS in the Al device was attributed to the Conductive bridge mechanism. In contrast, space-charge-limited driven conduction filament attributed the switching mechanism of the ITO device. Additionally, the Al-based device showed long retention ($> 10^3\ s$) and a reasonable large ($> 10^3$) ON/OFF ratio. Additionally, for this device, we also observed sweeping cycle induced reversal of voltage polarity of the V_{SET} and V_{RESET}. In contrast, we observed that increasing sweeping cycles resulted in an exponential decrease of the OFF-state resistance of the ITO based device.

Chapter 4 reports on conduction and resistive switching in devices consisting of chitosan dispersed with CdTe/CdSe core-shell quantum dots (QDs) active layers sandwiched between silver (Ag) and indium doped tin oxide (ITO) electrodes. Active layers consisting of 0.96 $wt\%$, 0.48 $wt\%$, 0.32 $wt\%$ and 0.24 $wt\%$ QDs to chitosan were deposited on the ITO surface using the cost-free drop cast method. The electrical study performed on all devices revealed ‘O-type’ memory behaviour with OFF-state current conduction mechanism attributed to hopping mechanism. On the other hand, the ON-state current in each device followed a unique mechanism, such that Ohmic behaviour was observed for the device with 0.96 $wt\%$, while linear then hopping, space-charge limited, and lastly, hopping conductions mechanisms were attributed to devices with 0.48 $wt\%$, 0.32 $wt\%$ and 0.24 $wt\%$, respectively. Our results show that these devices’ memory behaviour and conduction can be exploited by controlling the amount of CdTe/CdSe in the chitosan medium.

Chapter 5 reports four types of resistive random access memory (ReRAM) structures with an active layer comprising (1) MoS2 (device A), (2) PVP (device B), (3) PVP and MoS2 bilayer (device C), and (4) PVP + MoS2 nanocomposites with 10 $wt\%$ (device D), 20 $wt\%$ (device E), 30 $wt\%$ (device F) and 40 $wt\%$ (device G) MoS_2 fabricated with Al and Ag as bottom and top electrodes, respectively. A study of resistive switching and electrical conduction mechanisms of these ReRAM modules revealed that devices A and B did not exhibit switching characteristics. Device C showed a combination of bipolar and threshold switching with a low switching voltage of 0.40 V. Device G portrayed bipolar switching at 0.56 V. In Device C, space charge-limited conduction with transition voltage $V_{tr} = 0.24\ V$ was observed. On the other hand, Ohmic behaviour between 0 V and 0.22 V followed by trapping of charge in the 0.22 $V-0.56\ V$ regime before switching was noticed in device G. Both device C and G showed reasonably ($\geq 10^2$) ON/OFF ratio. In the nanocomposite devices, an increase in MoS2 content resulted in an increase in electrical conductivity in the Ohmic region, leading to threshold switching at 30 $wt\%$ (device F) and ultimately bipolar switching at 40 $wt\%$ (device G). These studies showed that both switching and conduction mechanisms are sensitive to the type and composition of the active layer in the devices studied.

Chapter 6 We report on resistive switching in ReRAM devices that uses chitosan/PVP composite as the active layers sandwiched between Al and Ag electrodes. ReRAMs with active layers consisting of 1:3, 1:1 and 3:1 chitosan to PVP ratio were studied. Asymmetric threshold switching with $V_{th} = -1.21\ V$ and $V_{hold} = -0.34\ V$ only in the negative voltage bias was obtained for the device with chitosan to PVP ratio of 1:3. The device with 1:1 chitosan to PVP ratio showed optimal memory behaviour with bipolar switching with $V_{SET} = +0.75\ V$ and $V_{RESET} = -0.28\ V$ in the first cycle, followed by asymmetric TS with $V_{th} = +0.84\ V$ and $V_{hold} = +0.19\ V$ during the second cycle and back to bipolar switching with $V_{SET} = +0.77\ V$ and $V_{RESET} = -0.45\ V$. No memory behaviour was observed for the 3:1 chitosan to PVP based device. Electrochemical conduction metalization was attributed to the switching mechanism in the device with 1:1 ratio of chitosan to PVP. Resistive switching based on organic polymers is essential for environmentally friendly devices. Our results reveal the applicability of chitosan and PVP blend in memory device fabrication and that both the memory and switching can be exploited by varying the ratio of chitosan to PVP in the composite.

Chapter 7 reports on resistive switching memory devices that use raw organic cow milk as active layers. Our devices comprised fat-free, medium cream and full cream raw cow milk active layers sandwiched between ITO and Ag. EDS analysis of all active layers reveals a relatively higher weight percentage of metallic ions in the medium fat milk film than fat-free and full-cream milk films. As such, an 'S-type' memory behaviour with switching at remarkably low $V_{SET} = 0.25\ V$ and $V_{RESET} = 0.45\ V$ was observed using the medium fat milk, making this device to be operated as low power memory. Both devices using fat-free and full-cream milk showed 'O-type' memory behaviour. The analysis of the transport mechanism showed that both fat-free and full cream milk-based devices' conduction and switching if due to hopping mechanism driven conductive filaments, while space-charge limited driven conducting filaments was attributed to the medium fat milk-based device.

8.0.1 Future research

This present work was concerned with discovering resistive switching in new materials such as cow milk and optimising both switching and memory behaviour in already known materials such as chitosan. Also to demonstrate that two organic polymers can be blended together to produce an optimised resistive switching. Therefore for future, more efforts should be put on blended polymers as that will minimise the use of conducting metals which pose threat to the environment. Also our discovery of resistive switching in cow milk provides new insight in the general field of ReRAM technology. We have already demonstrated that resistive switching in milk can be enhanced by introducing conductive particles. This will open more doors for research.

Bibliography

[1] Erik Spalvins, Brajesh Dubey, and Timothy Townsend. Impact of electronic waste disposal on lead concentrations in landfill leachate. *Environ. Sci. Technol.*, 42(19):7452–7458, 2008. ISSN 0013936X. doi: 10.1021/es8009277.

[2] Wenhui Li, Qian Liu, Yuniu Zhang, Chang'an Li, Zhenfei He, Wallace C.H. H. Choy, Paul J. Low, Prashant Sonar, and Aung Ko Ko Kyaw. Biodegradable Materials and Green Processing for Green Electronics. *Adv. Mater.*, 32(33):2001591, aug 2020. ISSN 15214095. doi: 10.1002/adma.202001591. URL `https://onlinelibrary.wiley.com/doi/10.1002/adma.202001591`.

[3] Mihai Irimia-Vladu. "Green" electronics: biodegradable and biocompatible materials and devices for sustainable future. *Chem. Soc. Rev.*, 43(2):588–610, 2014. ISSN 0306-0012. doi: 10.1039/C3CS60235D. URL `http://xlink.rsc.org/?DOI=C3CS60235D`.

[4] Mihai Irimia-Vladu, Eric D. Głowacki, Gundula Voss, Siegfried Bauer, and Niyazi Serdar Sariciftci. Green and biodegradable electronics, jul 2012. ISSN 13697021. URL `http://dx.doi.org/10.1016/S1369-7021(12)70139-6https://linkinghub.elsevier.com/retrieve/pii/S1369702112701396`.

[5] Betty Prince. *Semiconductor Memories: A handbook of Design, Man-*

ufacture, and Application. John Wiley and Sons, New York, second edi edition, 1991. ISBN 0471924652.

[6] Sung-Mo Kang and Yusuf Leblebici. *CMOS: Digital Integrated Circuits: Analysis and Design.* McGraw-Hill Companies Inc., 1996. ISBN 0071144234.

[7] Jan M Rabaey. *Digital Integrated Circuits: A Design Perspective.* Alan Apt, New Jersey, 1996. ISBN 0131786091.

[8] Ye Zhou, Su Ting Han, Prashant Sonar, and V. A.L. Roy. Nonvolatile multilevel data storage memory device from controlled ambipolar charge trapping mechanism. *Sci. Rep.*, 3:1–7, 2013. ISSN 20452322. doi: 10.1038/srep02319.

[9] Pengfei Hou, Zhanzhan Gao, and Kaikai Ni. Multilevel data storage memory based on polycrystalline SrTiO3 ultrathin film. *RSC Adv.*, 7 (78):49753–49758, 2017. ISSN 20462069. doi: 10.1039/c7ra09806e.

[10] Peter Haugen, John Whidden, Bret Sadler, and Ian Myers. Overview of Commonly Encountered types of Random Access Memory (RAM) By :. (Simoncelli), 2000.

[11] Sreedevi Vallabhapurapu, Shengzhi Dub, and Ananthakrishnan Srinivasan. Electronics : Nonvolatile Memory Technologies. In Munmaya Mishra, editor, *Encycl. Polym. Appl. First Ed.*, chapter Electronic, pages 913–931. CRC Press, 2018, New York, 1st edition, 2018. ISBN 9781351019422. doi: 10.1201/9781351019422-140000259.

[12] Hai Li and Yiran Chen. *NONVOLATILE MEMORY DESIGN: Magnetic , Resistive , and Phase Change.* Taylor & Francis Group, 2012. ISBN 9781439807460.

[13] Bruce Jacob, Sadagopan Srinivasan, and David T Wang. *The Memory System*. 2009. ISBN 9781598295870. URL `http://books.google.com/books?id=S{_}1WML-8yEoC{%}5Cnpapers2://publication/uuid/B5C3DE51-81C8-4331-B6C3-92FF787B09B2`.

[14] Fast Page. DRAM Devices Organization : Basic Circuits and Architecture. chapter 8, pages 353–376.

[15] Myeongsun Kim, Jongmin Ha, Ikhyeon Kwon, Jae Hee Han, Seongjae Cho, and Il Hwan Cho. A novel one-transistor dynamic random-access memory (1T DRAM) featuring partially inserted wide-bandgap double barriers for high-temperature applications. *Micromachines*, 2018. ISSN 2072666X. doi: 10.3390/mi9110581.

[16] Kevin K. Chang, Onur Mutlu, Abhijith Kashyap, Hasan Hassan, Saugata Ghose, Kevin Hsieh, Donghyuk Lee, Tianshi Li, Gennady Pekhimenko, and Samira Khan. Understanding Latency Variation in Modern DRAM Chips. *ACM SIGMETRICS Perform. Eval. Rev.*, pages 323–336, 2016. ISSN 01635999. doi: 10.1145/2896377.2901453. URL `http://dl.acm.org/citation.cfm?doid=2896377.2901453`.

[17] D. M. Barry, M. Meniconi, and N. A. Weir. Reliability modelling of dynamic random access memory devices subjected to high temperature soak tests. *Reliab. Eng.*, 17(4):255–266, 1987. ISSN 01438174. doi: 10.1016/0143-8174(87)90091-6.

[18] Yo Sep Min, Young Jin Cho, Igor P. Asanov, Jeong Hee Han, Wan Don Kim, and Cheol Seong Hwang. Bi1-x-yTixSiyOz (BTSO) thin films for dynamic random access memory capacitor applications. *Chem. Vap. Depos.*, 2005. ISSN 09481907. doi: 10.1002/cvde.200406328.

[19] Sang Woon Lee, Oh Seong Kwon, Jeong Hwan Han, and Cheol Seong Hwang. Enhanced electrical properties of SrTiO3 thin films grown

by atomic layer deposition at high temperature for dynamic random access memory applications. *Appl. Phys. Lett.*, 92(22), 2008. ISSN 00036951. doi: 10.1063/1.2939102.

[20] Thomas Vogelsang. Understanding the energy consumption of Dynamic Random Access Memories. In *Proc. Annu. Int. Symp. Microarchitecture, MICRO*, 2010. ISBN 9780769542997. doi: 10.1109/MICRO.2010.42.

[21] Heesang Kim, Byoungchan Oh, Younghwan Son, Kyungdo Kim, Seon Yong Cha, Jae Goan Jeong, Sung Joo Hong, and Hyungcheol Shin. Characterization of the variable retention time in dynamic random access memory. *IEEE Trans. Electron Devices*, 2011. ISSN 00189383. doi: 10.1109/TED.2011.2160066.

[22] Doo Seok Jeong, Reji Thomas, R. S. Katiyar, J. F. Scott, H. Kohlstedt, A. Petraru, and Cheol Seong Hwang. Emerging memories: resistive switching mechanisms and current status. *Reports Prog. Phys.*, 75 (7):076502, jul 2012. ISSN 0034-4885. doi: 10.1088/0034-4885/75/7/076502. URL `https://iopscience.iop.org/article/10.1088/0034-4885/75/7/076502`.

[23] Tim Wilmshurst. Introducing the PIC midrange family and 16F84A. In *Des. Embed. Syst. with PIC Microcontrollers Princ. Appl.*, pages 27–49. 2010. URL `https://doi.org/10.1016/B978-1-85617-750-4.10004-6`.

[24] Brian L. Dipert. *Inside flash memory*, volume 20. 1995. ISBN 9789048194308.

[25] Jack S. T. Haung. United States Patent (19), 1977.

[26] R. Shirota. *Developments in 3D-NAND Flash technology*. Woodhead Publishing Limited, 2014. ISBN 9780857098092. doi:

10.1533/9780857098092.1.27. URL http://dx.doi.org/10.1533/9780857098092.1.27.

[27] Rino Micheloni, Luca Crippa, and Alessia Marelli. *Inside NAND Flash Memories*, volume 53. Springer Netherlands, Dordrecht, nov 2010. ISBN 978-90-481-9430-8. doi: 10.1007/978-90-481-9431-5. URL http://link.springer.com/10.1007/978-90-481-9431-5.

[28] Joe E. Brewer and Manzur Gill. *Nonvolatile Memory Technologies with Emphasis on Flash: A Comprehensive Guide to Understanding and Using NVM Devices*. 2007. ISBN 9780471770022. doi: 10.1002/9780470181355.

[29] T. Eshita, T. Tamura, and Y. Arimoto. *Ferroelectric random access memory (FRAM) devices*. Woodhead Publishing Limited, 2014. ISBN 9780857098092. doi: 10.1533/9780857098092.3.434. URL http://dx.doi.org/10.1533/9780857098092.3.434.

[30] R. Bez and A. Pirovano. *Overview of non-volatile memory technology: markets, technologies and trends*. Woodhead Publishing Limited, 2014. ISBN 9780857098092. doi: 10.1533/9780857098092.1. URL http://dx.doi.org/10.1533/9780857098092.1.

[31] H. S.Philip Wong, Simone Raoux, Sangbum Kim, Jiale Liang, John P. Reifenberg, Bipin Rajendran, Mehdi Asheghi, and Kenneth E. Goodson. Phase change memory. *Proc. IEEE*, 98(12):2201–2227, 2010. ISSN 00189219. doi: 10.1109/JPROC.2010.2070050.

[32] Stanford R. Ovshinsky. Reversible electrical switching phenomena in disordered structures. *Phys. Rev. Lett.*, 1968. ISSN 00319007. doi: 10.1103/PhysRevLett.21.1450.

[33] S. Raoux and T.J. Ibm. *Phase change memory (PCM) materials and devices*. Number Feinleib 1971. Woodhead Publishing Limited, 2014.

ISBN 9780857098092. doi: 10.1533/9780857098092.2.161. URL http://dx.doi.org/10.1533/9780857098092.2.161.

[34] Geoffrey W. Burr, Matthew J. Breitwisch, Michele Franceschini, Davide Garetto, Kailash Gopalakrishnan, Bryan Jackson, Bülent Kurdi, Chung Lam, Luis A. Lastras, Alvaro Padilla, Bipin Rajendran, Simone Raoux, and Rohit S. Shenoy. Phase change memory technology. *J. Vac. Sci. Technol. B, Nanotechnol. Microelectron. Mater. Process. Meas. Phenom.*, 28(2):223–262, 2010. ISSN 2166-2746. doi: 10.1116/1.3301579.

[35] Z. H.U. Jian-Gang. Magnetoresistive random access memory: The path to competitiveness and scalability. *Proc. IEEE*, 2008. ISSN 00189219. doi: 10.1109/JPROC.2008.2004313.

[36] Dmytro Apalkov, Bernard Dieny, and J. M. Slaughter. Magnetoresistive Random Access Memory. *Proc. IEEE*, 2016. ISSN 0018-9219. doi: 10.1109/jproc.2016.2590142.

[37] Akihito Sawa. Resistive switching in transition metal oxides. *Mater. Today*, 11(6):28–36, 2008. ISSN 13697021. doi: 10.1016/S1369-7021(08)70119-6. URL http://dx.doi.org/10.1016/S1369-7021(08)70119-6.

[38] T. W. Hickmott. Low-Frequency Negative Resistance in Thin Anodic Oxide Films. *J. Appl. Phys.*, 33(9):2669–2682, sep 1962. ISSN 0021-8979. doi: 10.1063/1.1702530. URL http://aip.scitation.org/doi/10.1063/1.1702530.

[39] Jianyong Ouyang. *Emerging Resistive Switching Memories*. SpringerBriefs in Materials. Springer International Publishing, Cham, 2016. ISBN 978-3-319-31570-6. doi: 10.1007/978-3-319-31572-0. URL http://link.springer.com/10.1007/978-3-319-31572-0.

[40] Linggang Zhu, Jian Zhou, Zhonglu Guo, and Zhimei Sun. An overview of materials issues in resistive random access memory. *J. Mater.*, 1 (4):285–295, 2015. ISSN 23528486. doi: 10.1016/j.jmat.2015.07.009. URL `http://dx.doi.org/10.1016/j.jmat.2015.07.009`.

[41] Shimeng Yu. Resistive Random Access Memory (RRAM). *Synth. Lect. Emerg. Eng. Technol.*, 2(5):1–79, mar 2016. ISSN 2381-1412. doi: 10.2200/S00681ED1V01Y201510EET006. URL `http://www.morganclaypool.com/doi/10.2200/S00681ED1V01Y201510EET006https://www.morganclaypool.com/doi/pdf/10.2200/S00681ED1V01Y201510EET006`.

[42] Yong Du, Shirley Z. Shen, Kefeng Cai, and Philip S. Casey. Research progress on polymer-inorganic thermoelectric nanocomposite materials, 2012. ISSN 00796700.

[43] Sreedevi Vallabhapurapu, L.D. Varma Sangani, M. Ghanashyam Krishna, V.V. Srinivasu, C. Du, Shengzhi Du, and Ananthakrishnan Srinivasan. Resistive Switching in Reduced Graphene Oxide Incorporated Polyvinyl Alcohol Films. *Mater. Today Proc.*, 9(April 2018):615–620, 2019. ISSN 22147853. doi: 10.1016/j.matpr.2018.10.383. URL `https://linkinghub.elsevier.com/retrieve/pii/S2214785318326889http://dx.doi.org/10.1007/s00339-018-2062-y`.

[44] Feng Pan, Chao Chen, Zhi Shun Wang, Yu Chao Yang, Jing Yang, and Fei Zeng. Nonvolatile resistive switching memories-characteristics, mechanisms and challenges. *Prog. Nat. Sci. Mater. Int.*, 20(1):1–15, 2010. ISSN 10020071. doi: 10.1016/s1002-0071(12)60001-x. URL `http://dx.doi.org/10.1016/S1002-0071(12)60001-X`.

[45] D. Prime and S. Paul. Overview of organic memory devices.

Philos. Trans. R. Soc. A Math. Phys. Eng. Sci., 367(1905):4141–4157, oct 2009. doi: 10.1098/rsta.2009.0165. URL `https://royalsocietypublishing.org/doi/10.1098/rsta.2009.0165`.

[46] F. Pan, S. Gao, C. Chen, C. Song, and F. Zeng. Recent progress in resistive random access memories: Materials, switching mechanisms, and performance. *Mater. Sci. Eng. R Reports*, 83(1):1–59, 2014. ISSN 0927796X. doi: 10.1016/j.mser.2014.06.002. URL `http://dx.doi.org/10.1016/j.mser.2014.06.002`.

[47] Guangdong Zhou, Bai Sun, Ankun Zhou, Bo Wu, and Haishen Huang. A larger nonvolatile bipolar resistive switching memory behaviour fabricated using eggshells. *Curr. Appl. Phys.*, 17(2):235–239, feb 2017. ISSN 15671739. doi: 10.1016/j.cap.2016.09.018. URL `http://dx.doi.org/10.1016/j.cap.2016.09.018https://linkinghub.elsevier.com/retrieve/pii/S156717391630270X`.

[48] Chen Wang, Huaqiang Wu, Bin Gao, Teng Zhang, Yuchao Yang, and He Qian. Conduction mechanisms, dynamics and stability in ReRAMs. *Microelectron. Eng.*, 187-188:121–133, feb 2018. ISSN 01679317. doi: 10.1016/j.mee.2017.11.003. URL `https://doi.org/10.1016/j.mee.2017.11.003https://linkinghub.elsevier.com/retrieve/pii/S0167931717303672`.

[49] Sreedevi Vallabhapurapu, Ashwini Rohom, N. B. Chaure, C. Tu, S. Du, V. V. Srinivasu, and Ananthakrishnan Srinivasan. Hopping conductivity-mediated O-shaped memory behaviour in gelatin–graphene oxide composite films. *Appl. Phys. A*, 124(9):1–5, sep 2018. ISSN 14320630. doi: 10.1007/s00339-018-2062-y. URL `http://dx.doi.org/10.1007/s00339-018-2062-yhttp://link.springer.com/10.1007/s00339-018-2062-y`.

[50] Yujia Yang Li, Qingyun Qian, Xiaolin Zhu, Yujia Yang Li, Mayue Zhang, Jingni Li, Chunlan Ma, Hua Li, Jianmei Lu, and Qichun Zhang. Recent advances in organic-based materials for resistive memory applications. *InfoMat*, 2(6):995–1033, 2020. ISSN 2567-3165. doi: 10.1002/inf2.12120.

[51] Zongjie Shen, Chun Zhao, Yanfei Qi, Wangying Xu, Yina Liu, Ivona Z. Mitrovic, Li Yang, and Cezhou Zhao. Advances of RRAM devices: Resistive switching mechanisms, materials and bionic synaptic application. *Nanomaterials*, 10(8):1–31, 2020. ISSN 20794991. doi: 10.3390/nano10081437.

[52] Kuan Yew Cheong, Ilias Ait Tayeb, Feng Zhao, and Jafri Malin Abdullah. Review on resistive switching mechanisms of bio-organic thin film for non-volatile memory application. *Nanotechnol. Rev.*, 10(1): 680–709, 2021. ISSN 21919097. doi: 10.1515/ntrev-2021-0047.

[53] P.O Sliva, G Dir, and C Griffiths. Bistable switching and memory devices. *J. Non. Cryst. Solids*, 2:316–333, jan 1970. ISSN 00223093. doi: 10.1016/0022-3093(70)90148-1. URL `https://linkinghub.elsevier.com/retrieve/pii/0022309370901481`.

[54] Zhe Xi Lim, Sasidharan Sreenivasan, Yew Hoong Wong, Feng Zhao, and Kuan Yew Cheong. Filamentary Conduction in Aloe Vera Film for Memory Application. *Procedia Eng.*, 184:655–662, 2017. ISSN 18777058. doi: 10.1016/j.proeng.2017.04.133. URL `http://dx.doi.org/10.1016/j.proeng.2017.04.133https://linkinghub.elsevier.com/retrieve/pii/S1877705817316387`.

[55] Niloufar Raeis Hosseini and Jang-Sik Sik Lee. Resistive switching memory based on bioinspired natural solid polymer electrolytes.

ACS Nano, 9(1):419–426, jan 2015. ISSN 1936086X. doi: 10.1021/nn5055909. URL https://pubs.acs.org/doi/10.1021/nn5055909.

[56] Jiaqi Xu, Xiaoning Zhao, Zhongqiang Wang, Haiyang Xu, Junli Hu, Jiangang Ma, and Yichun Liu. Biodegradable Natural Pectin-Based Flexible Multilevel Resistive Switching Memory for Transient Electronics. *Small*, 15(4):1803970, jan 2019. ISSN 16136810. doi: 10.1002/smll.201803970. URL http://doi.wiley.com/10.1002/smll.201803970https://onlinelibrary.wiley.com/doi/10.1002/smll.201803970.

[57] Hong Wang, Bowen Zhu, Hua Wang, Xiaohua Ma, Yue Hao, and Xiaodong Chen. Ultra-Lightweight Resistive Switching Memory Devices Based on Silk Fibroin. *Small*, 12(25):3360–3365, 2016. ISSN 16136829. doi: 10.1002/smll.201600893.

[58] Sreedevi Vallabhapurapu, Ashwini Rohom, N. B. Chaure, Shengzhi Du, and Ananthakrishnan Srinivasan. Bistable resistive memory behavior in gelatin-CdTe quantum dot composite film. In *AIP Conf. Proc.*, volume 1953, page 030271, 2018. ISBN 9780735416482. doi: 10.1063/1.5032606. URL http://aip.scitation.org/doi/abs/10.1063/1.5032606.

[59] Poh Choon Ooi, Jian Lin, Tae Whan Kim, and Fushan Li. Indium-tin-oxide, free, flexible, nonvolatile memory devices based on graphene quantum dots sandwiched between polymethylsilsesquioxane layers. *Org. Electron.*, 32:115–119, may 2016. ISSN 15661199. doi: 10.1016/j.orgel.2016.02.020. URL http://dx.doi.org/10.1016/j.orgel.2016.02.020https://linkinghub.elsevier.com/retrieve/pii/S1566119916300635.

[60] Xinglong Ji, Li Song, Shuai Zhong, Yu Jiang, Kian Guan Lim, Chao

Wang, and Rong Zhao. Biodegradable and Flexible Resistive Memory for Transient Electronics. *J. Phys. Chem. C*, 122(29):16909–16915, jul 2018. ISSN 1932-7447. doi: 10.1021/acs.jpcc.8b03075. URL https://pubs.acs.org/doi/10.1021/acs.jpcc.8b03075.

[61] Shuchao Qin, Ruixin Dong, Xunling Yan, and Qianqian Du. A reproducible write-(read)n-erase and multilevel bio-memristor based on DNA molecule. *Org. Electron.*, 22:147–153, 2015. ISSN 15661199. doi: 10.1016/j.orgel.2015.03.045. URL http://dx.doi.org/10.1016/j.orgel.2015.03.045.

[62] Q. Li, E. T. Dunn, E. W. Grandmaison, and M. F.A. Goosen. Applications and Properties of Chitosan. *J. Bioact. Compat. Polym.*, 7(4): 370–397, 1992. ISSN 08839115. doi: 10.1177/088391159200700406.

[63] Niloufar Raeis Hosseini and Jang-Sik Sik Lee. Biocompatible and Flexible Chitosan-Based Resistive Switching Memory with Magnesium Electrodes. *Adv. Funct. Mater.*, 25(35):5586–5592, sep 2015. ISSN 16163028. doi: 10.1002/adfm.201502592. URL http://doi.wiley.com/10.1002/adfm.201502592https://onlinelibrary.wiley.com/doi/10.1002/adfm.201502592.

[64] Bindu Nair. FINAL REPORT ON THE SAFETY ASSESSMENT OF POLYVINYLPYRROLIDONE (PVP). *Int. J. Toxicol.*, 17(1):95–130, sep 1998. ISSN 1091-5818. doi: 10.1080/109158198226017. URL http://www.informaworld.com/openurl?genre=article{&}doi=10.1080/109158198226017{&}magic=crossref{%}7C{%}7CD404A21C5BB053405B1A640AFFD44AE3.

[65] G. Amokrane, C. Falentin-Daudré, S. Ramtani, and Véronique Migonney. A Simple Method to Functionalize PCL Surface by Grafting Bioactive Polymers Using UV Irradiation. *Irbm*, 39(4):268–278,

2018. ISSN 18760988. doi: 10.1016/j.irbm.2018.07.002. URL `https://doi.org/10.1016/j.irbm.2018.07.002`.

[66] Richard Voo, M. Mariatti, and L. C. Sim. Properties of epoxy nanocomposite thin films prepared by spin coating technique. *J. Plast. Film Sheeting*, 27(4):331–346, 2011. ISSN 87560879. doi: 10.1177/8756087911419745.

[67] Ken NAKAJIMA, Kei SEKINE, Kaede MOGI, Makiko ITO, and Xiaobin LIANG. Atomic Force Microscopy. *J. Japan Soc. Colour Mater.*, 93(10):321–328, oct 2020. ISSN 0010-180X. doi: 10.4011/shikizai.93.321. URL `https://www.jstage.jst.go.jp/article/shikizai/93/10/93{_}321/{_}article/-char/ja/`.

[68] Akram Jassim Jawad and Queen Mary. *AFM Handbook ; Theoretical Principles and Experimental Parameters*. Number September. International Book Market Service LTD, 2020. ISBN 978-613-8-94061-6.

[69] G. Binnig, C. F. Quate, and Ch. Gerber. Atomic Force Microscope. *Phys. Rev. Lett.*, 56(9):930–933, mar 1986. ISSN 0031-9007. doi: 10.1103/PhysRevLett.56.930. URL `https://www.taylorfrancis.com/books/9781420075250https://link.aps.org/doi/10.1103/PhysRevLett.56.930`.

[70] NanoScience instruments. Scanning Electron Microscopy - Nanoscience Instruments, 2018. URL `https://www.nanoscience.com/techniques/scanning-electron-microscopy/`.

[71] JEOL-JSM-6700F-SEM-Users-Manual.pdf.

[72] Bernard Geffroy, Philippe le Roy, and Christophe Prat. Organic light-emitting diode (OLED) technology: materials, devices and display technologies. *Polym. Int.*, 55(6):572–582, jun 2006. ISSN 0959-

8103. doi: 10.1002/pi.1974. URL `https://onlinelibrary.wiley.com/doi/10.1002/pi.1974`.

[73] Yong-Jae Lee, Se-Heon Kim, Joon Huh, Guk-Hyun Kim, Yong-Hee Lee, Sang-Hwan Cho, Yoon-Chang Kim, and Young Rag Do. A high-extraction-efficiency nanopatterned organic light-emitting diode. *Appl. Phys. Lett.*, 82(21):3779–3781, may 2003. ISSN 0003-6951. doi: 10.1063/1.1577823. URL `http://aip.scitation.org/doi/10.1063/1.1577823`.

[74] Jiangeng Xue, Soichi Uchida, Barry P. Rand, and Stephen R. Forrest. 4.2% efficient organic photovoltaic cells with low series resistances. *Appl. Phys. Lett.*, 84(16):3013–3015, apr 2004. ISSN 0003-6951. doi: 10.1063/1.1713036. URL `http://aip.scitation.org/doi/10.1063/1.1713036`.

[75] Hagen Klauk. Organic thin-film transistors. *Chem. Soc. Rev.*, 39(7):2643, 2010. ISSN 0306-0012. doi: 10.1039/b909902f. URL `http://xlink.rsc.org/?DOI=b909902f`.

[76] Björn Lüssem, Chang-Min Keum, Daniel Kasemann, Ben Naab, Zhenan Bao, and Karl Leo. Doped Organic Transistors. *Chem. Rev.*, 116(22):13714–13751, nov 2016. ISSN 0009-2665. doi: 10.1021/acs.chemrev.6b00329. URL `https://pubs.acs.org/doi/10.1021/acs.chemrev.6b00329`.

[77] Sunkook Kim, Hyuk-Jun Kwon, Sunghun Lee, Hongshik Shim, Youngtea Chun, Woong Choi, Jinho Kwack, Dongwon Han, Myoungseop Song, Sungchul Kim, Saeed Mohammadi, Inseo Kee, and Sang Yoon Lee. Low-Power Flexible Organic Light-Emitting Diode Display Device. *Adv. Mater.*, 23(31):3511–3516, aug 2011.

ISSN 09359648. doi: 10.1002/adma.201101066. URL https://onlinelibrary.wiley.com/doi/10.1002/adma.201101066.

[78] Sang Jin Kim, Kyoungjun Choi, Bora Lee, Yuna Kim, and Byung Hee Hong. Materials for Flexible, Stretchable Electronics: Graphene and 2D Materials. *Annu. Rev. Mater. Res.*, 45(1):63–84, jul 2015. ISSN 1531-7331. doi: 10.1146/annurev-matsci-070214-020901. URL http://www.annualreviews.org/doi/10.1146/annurev-matsci-070214-020901.

[79] M Hussain Muhammad, Zhenqiang Ma, and Sohail F Shaikh. *Flexible and Stretchable Electronics*, volume 27. MDPI, jun 2017. ISBN 978-3-03842-437-6. doi: 10.3390/books978-3-03842-437-6. URL http://www.mdpi.com/books/pdfview/book/323.

[80] Sreedevi Vallabhapurapu, L. D. Varma Sangani, M. Ghanashyam Krishna, J. Das, A. Srinivasan, and V. V. Srinivasu. Optical and resistive switching properties of Chitosan-aluminum-doped zinc oxide composite thin films for transparent resistive random access memory application. *J. Mater. Sci. Mater. Electron.*, 32(3):3556–3565, feb 2021. ISSN 0957-4522. doi: 10.1007/s10854-020-05102-y. URL http://link.springer.com/10.1007/s10854-020-05102-y.

[81] Hanju Jo, Jieun Ko, Jung Ah Lim, Hye Jung Chang, and Youn Sang Kim. Organic Nonvolatile Resistive Switching Memory Based on Molecularly Entrapped Fullerene Derivative within a Diblock Copolymer Nanostructure. *Macromol. Rapid Commun.*, 34(4):355–361, feb 2013. ISSN 10221336. doi: 10.1002/marc.201200614. URL https://onlinelibrary.wiley.com/doi/10.1002/marc.201200614.

[82] Michael Cölle, Michael Büchel, and Dago M. de Leeuw. Switching and filamentary conduction in non-volatile organic memories. *Org. Elec-*

tron., 7(5):305–312, oct 2006. ISSN 15661199. doi: 10.1016/j.orgel.2006.03.014. URL https://linkinghub.elsevier.com/retrieve/pii/S1566119906000577.

[83] Niloufar Raeis-hosseini and Jang-sik Lee. Resistive switching memory using biomaterials. *J. Electroceramics*, 39(1-4):223–238, dec 2017. ISSN 1385-3449. doi: 10.1007/s10832-017-0104-z. URL https://link.springer.com/article/10.1007/s10832-017-0104-zhttp://link.springer.com/10.1007/s10832-017-0104-z.

[84] Lei Li and Guangming Li. Multi-bit biomemory based on chitosan: Graphene oxide nanocomposite with wrinkled surface. *Micromachines*, 11(6):1–13, 2020. ISSN 2072666X. doi: 10.3390/mi11060580.

[85] Ying-fan Liu and Jun-sheng Yu. Selective synthesis of CdTe and high luminescence CdTe/CdS quantum dots: The effect of ligands. *J. Colloid Interface Sci.*, 333(2):690–698, may 2009. ISSN 00219797. doi: 10.1016/j.jcis.2009.01.008. URL http://dx.doi.org/10.1016/j.jcis.2009.01.008https://linkinghub.elsevier.com/retrieve/pii/S0021979709000228.

[86] Zheng Fang, Lu Liu, Linlin Xu, Xiaoguang Yin, and Xinhua Zhong. Synthesis of highly stable dihydrolipoic acid capped water-soluble CdTe nanocrystals. *Nanotechnology*, 19(23):235603, jun 2008. ISSN 0957-4484. doi: 10.1088/0957-4484/19/23/235603. URL https://iopscience.iop.org/article/10.1088/0957-4484/19/23/235603.

[87] Haiyan Wang, Qiongfang Chen, Zhian Tan, Xunxun Yin, and Lun Wang. Electrochemiluminescence of CdTe quantum dots capped with glutathione and thioglycolic acid and its sensing of pb2+. *Electrochim. Acta*, 72:28–31, jun 2012. ISSN 00134686. doi: 10.1016/j.electacta.2012.03.146. URL

http://dx.doi.org/10.1016/j.electacta.2012.03.146https://linkinghub.elsevier.com/retrieve/pii/S0013468612004987.

[88] Debasis Bera, Lei Qian, Teng-Kuan Tseng, and Paul H Holloway. Quantum Dots and Their Multimodal Applications: A Review. *Materials (Basel).*, 3(4):2260–2345, mar 2010. ISSN 1996-1944. doi: 10.3390/ma3042260. URL http://www.mdpi.com/1996-1944/3/4/2260.

[89] Suli Wu, Dou Jun, Jie Zhang, and Shufen Zhang. A simple and economical one-pot method to synthesize high-quality water soluble CdTe QDs. *J. Mater. Chem.*, 22(29):14573–14578, 2012. doi: 10.1039/c2jm31409f.

[90] Jandi Kim, Bui The Huy, Kavitha Sakthivel, Hye Jung Choi, Woo Hong Joo, Seung Kyun Shin, Min Jae Lee, and Yong-Ill Lee. Highly fluorescent CdTe quantum dots with reduced cytotoxicity-A Robust biomarker. *Sens. Bio-Sensing Res.*, 3:46–52, mar 2015. ISSN 22141804. doi: 10.1016/j.sbsr.2014.12.001. URL http://dx.doi.org/10.1016/j.sbsr.2014.12.001https://linkinghub.elsevier.com/retrieve/pii/S2214180414000427.

[91] Shan-Shan Yang, Cui-Ling Ren, Zhen-Yang Zhang, Jun-Jie Hao, Qin Hu, and Xing-Guo Chen. Aqueous Synthesis of CdTe/CdSe Core/Shell Quantum Dots as pH-Sensitive Fluorescence Probe for the Determination of Ascorbic Acid. *J. Fluoresc.*, 21(3):1123–1129, may 2011. ISSN 1053-0509. doi: 10.1007/s10895-010-0788-9. URL http://link.springer.com/10.1007/s10895-010-0788-9.

[92] Xiaogang Chen, Liang Li, Yongxian Lai, Jianna Yan, Yichen Tang, and Xiuli Wang. Microwave-Assisted Synthesis of Glutathione-Capped CdTe/CdSe Near-Infrared Quantum Dots for Cell Imaging. *Int. J.*

Mol. Sci., 16(12):11500–11508, may 2015. ISSN 1422-0067. doi: 10.3390/ijms160511500. URL http://www.mdpi.com/1422-0067/16/5/11500.

[93] Hongyan Zhang, Pan Sun, Chang Liu, Huanyu Gao, Linru Xu, Jin Fang, Meng Wang, Jinling Liu, and Shukun Xu. L-Cysteine capped CdTe-CdS core-shell quantum dots: preparation, characterization and immuno-labeling of HeLa cells. *Luminescence*, 26(2):86–92, mar 2011. ISSN 15227235. doi: 10.1002/bio.1188. URL https://onlinelibrary.wiley.com/doi/10.1002/bio.1188.

[94] Do Hyeong Kim, Chaoxing Wu, Dong Hyun Park, Woo Kyum Kim, Hae Woon Seo, Sang Wook Kim, and Tae Whan Kim. Flexible Memristive Devices Based on InP/ZnSe/ZnS Core–Multishell Quantum Dot Nanocomposites. *ACS Appl. Mater. Interfaces*, 10(17):14843–14849, may 2018. ISSN 1944-8244. doi: 10.1021/acsami.7b18817. URL https://pubs.acs.org/doi/10.1021/acsami.7b18817.

[95] Tejasvinee S. Bhat, Chetan C. Revadekar, Satyajeet S. Patil, Tukaram D. Dongale, Deok-kee Kim, and Pramod S. Patil. Photo-induced resistive switching in CdS-sensitized TiO2 nanorod array memristive device. *J. Mater. Sci. Mater. Electron.*, 31(13):10919–10929, jul 2020. ISSN 0957-4522. doi: 10.1007/s10854-020-03643-w. URL https://doi.org/10.1007/s10854-020-03643-whttps://link.springer.com/10.1007/s10854-020-03643-w.

[96] Jianwei Guo, Shen Guo, Xiaoming Su, Sheng Zhu, Yue Pang, Wei Luo, Jianbing Zhang, Huajun Sun, Honglang Li, and Daoli Zhang. Nonvolatile Resistive Switching Memory Device Employing CdSe/CdS Core/Shell Quantum Dots as an Electrode Modification Layer. *ACS Appl. Electron. Mater.*, 2(3):827–837, mar 2020. ISSN 2637-6113.

doi: 10.1021/acsaelm.0c00006. URL https://pubs.acs.org/doi/10.1021/acsaelm.0c00006.

[97] Olamide Abiodun Daramola, Xavier Siwe-Noundou, Potlaki Foster Tseki, and Rui Werner Maçedo Krause. Rapid Synthesis of Thiol-Co-Capped-CdTe/CdSe/ZnSe Core Shell-Shell Nanoparticles: Their Optical and Structural Morphology. *Nanomaterials*, 11(5):1193, may 2021. ISSN 2079-4991. doi: 10.3390/nano11051193. URL https://www.mdpi.com/2079-4991/11/5/1193.

[98] M. Melvin David Kumar and Suganthi Devadason. Structural and optical properties of CdTe/CdSe heterostructure multilayer thin films prepared by physical vapor deposition technique. *Appl. Nanosci.*, 3(5): 453–459, oct 2013. ISSN 2190-5509. doi: 10.1007/s13204-012-0150-4. URL http://link.springer.com/10.1007/s13204-012-0150-4.

[99] Vandana Ghormade, Haribhau Gholap, Sonia Kale, Vaishnavi Kulkarni, Suresh Bhat, and Kishore Paknikar. Fluorescent cadmium telluride quantum dots embedded chitosan nanoparticles: A stable, biocompatible preparation for bio-imaging. *J. Biomater. Sci. Polym. Ed.*, 26(1):42–56, jan 2015. ISSN 15685624. doi: 10.1080/09205063.2014.982240. URL http://dx.doi.org/10.1080/09205063.2014.982240http://www.tandfonline.com/doi/abs/10.1080/09205063.2014.982240.

[100] Y. B. Zhu, K. Zheng, X. Wu, and L. K. Ang. Enhanced stability of filament-type resistive switching by interface engineering. *Sci. Rep.*, 7 (1):43664, may 2017. ISSN 2045-2322. doi: 10.1038/srep43664. URL http://www.nature.com/articles/srep43664.

[101] Kuan-Liang Lin, Tuo-Hung Hou, Jiann Shieh, Jun-Hung Lin, Cheng-Tung Chou, and Yao-Jen Lee. Electrode dependence of filament for-

mation in HfO 2 resistive-switching memory. *J. Appl. Phys.*, 109(8): 084104, apr 2011. ISSN 0021-8979. doi: 10.1063/1.3567915. URL `http://aip.scitation.org/doi/10.1063/1.3567915`.

[102] H. Y. Peng, L. Pu, J. C. Wu, D. Cha, J. H. Hong, W. N. Lin, Y. Y. Li, J. F. Ding, A. David, K. Li, and T. Wu. Effects of electrode material and configuration on the characteristics of planar resistive switching devices. *APL Mater.*, 1(5):052106, nov 2013. ISSN 2166-532X. doi: 10.1063/1.4827597. URL `http://aip.scitation.org/doi/10.1063/1.4827597`.

[103] E Hernández-Rodríguez, A Márquez-Herrera, E Zaleta-Alejandre, M Meléndez-Lira, W de la Cruz, and M Zapata-Torres. Effect of electrode type in the resistive switching behaviour of TiO 2 thin films. *J. Phys. D. Appl. Phys.*, 46(4):045103, jan 2013. ISSN 0022-3727. doi: 10.1088/0022-3727/46/4/045103. URL `https://iopscience.iop.org/article/10.1088/0022-3727/46/4/045103`.

[104] P.K. K Biswas, A De, L.K. K Dua, and L Chkoda. Work function of sol–gel indium tin oxide (ITO) films on glass. *Appl. Surf. Sci.*, 253(4): 1953–1959, dec 2006. ISSN 01694332. doi: 10.1016/j.apsusc.2006.03.042. URL `www.elsevier.com/locate/apsuschttps://linkinghub.elsevier.com/retrieve/pii/S0169433206002959`.

[105] J.K. Grepstad, P.O. Gartland, and B.J. Slagsvold. Anisotropic work function of clean and smooth low-index faces of aluminium. *Surf. Sci.*, 57(1):348–362, jul 1976. ISSN 00396028. doi: 10.1016/0039-6028(76)90187-4. URL `https://linkinghub.elsevier.com/retrieve/pii/0039602876901874`.

[106] Sreedevi Vallabhapurapu, S. Du, T.S. S. Mahule, N.B. B. Chaure, V.V. V. Srinivasu, Ashwini Roham, C. Tu, and A. Srinivasan. Resis-

tive Switching Memory Effect and Conduction Mechanism in Nano-Silver Incorporated Type-A Gelatin Films. In *2018 Open Innov. Conf. OI 2018*, pages 281–284. IEEE, oct 2018. ISBN 9781538653166. doi: 10.1109/OI.2018.8535678. URL `https://ieeexplore.ieee.org/document/8535678/`.

[107] Olawumi Akinfenwa Oladeji, Sreedevi Vallabhapurapu, and Issac O. Osunmakinde. ReRAM Memory Cells Based on Gelatin Nano Composites: Towards Green Computing. In *2019 Open Innov.*, pages 216–218. IEEE, oct 2019. ISBN 978-1-7281-3464-2. doi: 10.1109/OI.2019.8908208. URL `https://ieeexplore.ieee.org/document/8908208/`.

[108] Francisco J. Romero, Alejando Toral, Alberto Medina-Rull, Carmen Lucia Moraila-Martinez, Diego P. Morales, Akiko Ohata, Andres Godoy, Francisco G. Ruiz, and Noel Rodriguez. Resistive Switching in Graphene Oxide. *Front. Mater.*, 7(January):1–5, jan 2020. ISSN 22968016. doi: 10.3389/fmats.2020.00017. URL `https://www.frontiersin.org/article/10.3389/fmats.2020.00017/full`.

[109] Guangdong Zhou, Yanqing Yao, Zhisong Lu, Xiude Yang, Juanjuan Han, Gang Wang, Xi Rao, Ping Li, Qian Liu, and Qunliang Song. Hydrogen-peroxide-modified egg albumen for transparent and flexible resistive switching memory. *Nanotechnology*, 28(42):425202, oct 2017. ISSN 13616528. doi: 10.1088/1361-6528/aa8397. URL `https://iopscience.iop.org/article/10.1088/1361-6528/aa8397`.

[110] Li Zhou, Jingyu Mao, Yi Ren, Su Ting Han, Vellaisamy A.L. Roy, and Ye Zhou. Recent Advances of Flexible Data Storage Devices Based on Organic Nanoscaled Materials. *Small*, 14(10):1–27, 2018. ISSN 16136829. doi: 10.1002/smll.201703126.

[111] Sun Yanmei, Ai Chunpeng, Lu Junguo, Li Lei, Wen Dianzhong, and

Bai Xuduo. The influence of thickness onmemory characteristic based on nonvolatile tuning behavior in poly(N-vinylcarbazole) films. *Thin Solid Films*, 598:293–298, jan 2016. ISSN 00406090. doi: 10.1016/j.tsf.2015.12.029. URL `https://linkinghub.elsevier.com/retrieve/pii/S0040609015012791`.

[112] Bai Huang, Hui He, Hao Liu, Yue Zhang, Handong Chen, and Yuanbin Ma. Co-precipitated poly(vinyl alcohol)/chitosan composites with excellent mechanical properties and tunable water-induced shape memory. *Carbohydr. Polym.*, 245(March):116445, 2020. ISSN 01448617. doi: 10.1016/j.carbpol.2020.116445. URL `https://doi.org/10.1016/j.carbpol.2020.116445`.

[113] Hau Huu Do Ho, Trung Minh Le, and Ngoc Kim Pham. The Resistive Switching Behavior of Al/Chitosan-Graphene Oxide/FTO Structure. *J. Nanomater.*, 2021:1–7, 2021. ISSN 1687-4110. doi: 10.1155/2021/5565169.

[114] Niloufar Raeis-Hosseini and Jang Sik Lee. Controlling the Resistive Switching Behavior in Starch-Based Flexible Biomemristors. *ACS Appl. Mater. Interfaces*, 8(11):7326–7332, 2016. ISSN 19448252. doi: 10.1021/acsami.6b01559.

[115] Ritesh Kumar, Sapana Ranwa, and Gulshan Kumar. Biodegradable Flexible Substrate Based on Chitosan/PVP Blend Polymer for Disposable Electronics Device Applications. *J. Phys. Chem. B*, 124(1):149–155, jan 2020. ISSN 1520-6106. doi: 10.1021/acs.jpcb.9b08897. URL `https://pubs.acs.org/doi/10.1021/acs.jpcb.9b08897`.

[116] Bolin Guo, Bai Sun, Wentao Hou, Yuanzheng Chen, Shouhui Zhu, Suangsuo Mao, Liang Zheng, Ming Lei, Bing Li, and Guoqiang Fu. A sustainable resistive switching memory device based on organic ker-

atin extracted from hair. *RSC Adv.*, 9(22):12436–12440, 2019. ISSN 20462069. doi: 10.1039/c8ra10643f.

[117] Zolile Wiseman Dlamini, Sreedevi Vallabhapurapu, Olamide Abiodun Daramola, Potlaki Foster Tseki, Rui Werner Macedo Krause, Xavier Siwe-Noundou, Tebogo Sfiso Mahule, and Srinivasu Vijaya Vallabhapurapu. Resistive Switching in CdTe/CdSe Core–Shell Quantum Dots Embedded Chitosan-Based Memory Devices. *J. Circuits, Syst. Comput.*, 31(06), apr 2022. ISSN 0218-1266. doi: 10.1142/S0218126622501134. URL `https://www.worldscientific.com/doi/abs/10.1142/S0218126622501134`.

[118] Ee Wah Lim and Razali Ismail. Conduction mechanism of valence change resistive switching memory: A survey. *Electron.*, 4(3):586–613, sep 2015. ISSN 20799292. doi: 10.3390/electronics4030586. URL `www.mdpi.com/journal/electronicshttp://www.mdpi.com/2079-9292/4/3/586`.

[119] Shiwei Wu, Hong Wang, Jing Sun, Fang Song, Zhan Wang, Mei Yang, He Xi, Yong Xie, Haixia Gao, Jigang Ma, Xiaohua Ma, and Yue Hao. Dissolvable and biodegradable resistive switching memory based on magnesium oxide. *IEEE Electron Device Lett.*, 37(8):990–993, 2016. ISSN 07413106. doi: 10.1109/LED.2016.2585665.

[120] Fu-chien Chiu. A Review on Conduction Mechanisms in Dielectric Films. *Adv. Mater. Sci. Eng.*, 2014:1–18, 2014. ISSN 1687-8434. doi: 10.1155/2014/578168. URL `http://eds.a.ebscohost.com/eds/pdfviewer/pdfviewer?vid=4{&}sid=5e5d80fd-ae57-4301-901b-487ad3996e6b{%}40sessionmgr4001{&}hid=4110http://www.hindawi.com/journals/amse/2014/578168/`.

[121] Guoping Li, Yun Hou, and Aizhi Wu. Fourth Industrial Revo-

lution: technological drivers, impacts and coping methods. *Chinese Geogr. Sci.*, 27(4):626–637, aug 2017. ISSN 1002-0063. doi: 10.1007/s11769-017-0890-x. URL `http://link.springer.com/10.1007/s11769-017-0890-x`.

[122] Gerhard Fettweis and E Zimmermann. ICT energy consumption-trends and challenges. *Int. Symp. Wirel. Pers. Multimed. Commun.*, (Wpmc 2008):2006–2009, 2008. URL `https://mns.ifn.et.tu-dresden.de/Lists/nPublications/Attachments/559/Fettweis{_}G{_}WPMC{_}08.pdf`.

[123] Shuting Liu, Shurong Dong, Xingang Wang, Lin Shi, Hongsheng Xu, Shuyi Huang, and Jikui Luo. Flexible and fully biodegradable resistance random access memory based on a gelatin dielectric. *Nanotechnology*, 31(25), 2020. ISSN 13616528. doi: 10.1088/1361-6528/ab7a2c.

[124] Tsung-Ling Tsai, Hsiang-Yu Chang, Jesse Jen-Chung Lou, and Tseung-Yuen Tseng. A high performance transparent resistive switching memory made from ZrO 2 /AlON bilayer structure. *Appl. Phys. Lett.*, 108(15):153505, apr 2016. ISSN 0003-6951. doi: 10.1063/1.4946006. URL `http://aip.scitation.org/doi/10.1063/1.4946006`.

[125] Abiodun Temidayo Fabiyi, Sreedevi Vallabhapurapu, and Issac O. Osunmakinde. Biodegradable ReRAM based on chitosan for nonvolatile memory application. In *2019 Open Innov.*, pages 211–215. IEEE, oct 2019. ISBN 978-1-7281-3464-2. doi: 10.1109/OI.2019.8908222. URL `https://ieeexplore.ieee.org/document/8908222/`.

[126] Chia-Wen Zhong, Wen-Hsien Tzeng, Kou-Chen Liu, Horng-Chih Lin, Kow-Ming Chang, Yi-Chun Chan, Chun-Chih Kuo, Pang-Shiu Chen, Heng-Yuan Lee, Frederick Chen, and Ming-Jinn Tsai. Effect of ITO

electrode with different oxygen contents on the electrical characteristics of HfO x RRAM devices. *Surf. Coatings Technol.*, 231:563–566, sep 2013. ISSN 02578972. doi: 10.1016/j.surfcoat.2012.07.039. URL http://dx.doi.org/10.1016/j.surfcoat.2012.07.039https://linkinghub.elsevier.com/retrieve/pii/S025789721200727X.

[127] O. El Beqqali, I. Zorkani, F. Rogemond, H. Chermette, R. Ben Chaabane, M. Gamoudi, and G. Guillaud. Electrical properties of molybdenum disulfide MoS2. Experimental study and density functional calculation results. *Synth. Met.*, 90(3):165–172, 1997. ISSN 03796779. doi: 10.1016/s0379-6779(98)80002-7.

[128] Xiao Li and Hongwei Zhu. Two-dimensional MoS2: Properties, preparation, and applications. *J. Mater.*, 1(1):33–44, 2015. ISSN 23528486. doi: 10.1016/j.jmat.2015.03.003.

[129] Muharrem Acerce, Damien Voiry, and Manish Chhowalla. Metallic 1T phase MoS2 nanosheets as supercapacitor electrode materials. *Nat. Nanotechnol.*, 10(4):313–318, 2015. ISSN 17483395. doi: 10.1038/nnano.2015.40.

[130] Ravi Prakash, Shubham Sharma, Anuj Kumar, and Davinder Kaur. Improved resistive switching performance in Cu-cation migrated MoS2 based ReRAM device incorporated with tungsten nitride bottom electrode. *Curr. Appl. Phys.*, 19(3):260–265, mar 2019. ISSN 15671739. doi: 10.1016/j.cap.2018.10.013. URL https://doi.org/10.1016/j.cap.2018.10.013https://linkinghub.elsevier.com/retrieve/pii/S1567173918302839.

[131] Na Bai, Min Xu, Cong Hu, Yaodong Ma, Qi Wang, Deyan He, Jing Qi, and Yingtao Li. Resistive switching behaviors mediated by grain boundaries in one longitudinal Al/MoS2&PVP/ITO device. *Mater.*

Sci. Semicond. Process., 91(November 2018):246–251, 2019. ISSN 13698001. doi: 10.1016/j.mssp.2018.11.024. URL `https://doi.org/10.1016/j.mssp.2018.11.024`.

[132] Zijin Wu, Tongtong Wang, Changqi Sun, Peitao Liu, Baorui Xia, Jingyan Zhang, Yonggang Liu, and Daqiang Gao. Resistive switching effect of N-doped MoS 2 -PVP nanocomposites films for nonvolatile memory devices. *AIP Adv.*, 7(12):125213, dec 2017. ISSN 2158-3226. doi: 10.1063/1.4994227. URL `http://dx.doi.org/10.1063/1.4994227http://aip.scitation.org/doi/10.1063/1.4994227`.

[133] S. Vallabhapurapu, L. D. Varma Sangani, M. Ghanashyam Krishna, J. Das, C. Tu, S. Du, and A. Srinivasan. Resistive switching behaviour in PMMA/Al:ZnO Composite films. *Acta Phys. Pol. A*, 134(1):68–70, 2018. ISSN 1898794X. doi: 10.12693/APhysPolA.134.68.

[134] B. Sun, S. Ranjan, G. Zhou, T. Guo, Y. Xia, L. Wei, Y. N. Zhou, and Y. A. Wu. Multistate resistive switching behaviors for neuromorphic computing in memristor. *Mater. Today Adv.*, 9, 2021. ISSN 25900498. doi: 10.1016/j.mtadv.2020.100125.

[135] Yanhong Liu, Ping Gao, Xuening Jiang, La Li, Jialiang Zhang, and Wei Peng. Percolation mechanism through trapping/de-trapping process at defect states for resistive switching devices with structure of Ag/SixC 1-x/p-Si. *J. Appl. Phys.*, 116(6), 2014. ISSN 10897550. doi: 10.1063/1.4893016.

[136] Komal T. Patil, Kiran A. Nirmal, Sushilkumar A. Jadhav, Swapnil R. Patil, Tukaram D. Dongale, Deok kee Kim, and Pramod S. Patil. Bipolar resistive switching and non-volatile memory properties of MnO2-polyaniline (PANI) nanocomposite. *Materialia*, 15(February):

101026, 2021. ISSN 25891529. doi: 10.1016/j.mtla.2021.101026. URL https://doi.org/10.1016/j.mtla.2021.101026.

[137] Ujjal Das, Anupriya Nyayban, Bappi Paul, Arabinda Barman, Pranab Sarkar, and Asim Roy. Compliance Current-Dependent Dual-Functional Bipolar and Threshold Resistive Switching in All-Inorganic Rubidium Lead-Bromide Perovskite-Based Flexible Device. *ACS Appl. Electron. Mater.*, 2(5):1343–1351, 2020. ISSN 2637-6113. doi: 10.1021/acsaelm.0c00130.

[138] Yu Chao Yang, Feng Pan, and Fei Zeng. Bipolar resistance switching in high-performance Cu/ZnO : MMn/Pt nonvolatile memories: Active region and influence of Joule heating. *New J. Phys.*, 12, 2010. ISSN 13672630. doi: 10.1088/1367-2630/12/2/023008.

[139] Sachin M. Shinde, Golap Kalita, and Masaki Tanemura. Fabrication of poly(methyl methacrylate)-MoS 2 /graphene heterostructure for memory device application. *J. Appl. Phys.*, 116(21):214306, dec 2014. ISSN 0021-8979. doi: 10.1063/1.4903552. URL http://aip.scitation.org/doi/10.1063/1.4903552.

[140] Muhammad Muqeet Rehman, Ghayas Uddin Siddiqui, Jahan Zeb Gul, Soo Wan Kim, Jong Hwan Lim, and Kyung Hyun Choi. Resistive Switching in All-Printed, Flexible and Hybrid MoS2 -PVA Nanocomposite based Memristive Device Fabricated by Reverse Offset. *Sci. Rep.*, 6(November):1–10, 2016. ISSN 20452322. doi: 10.1038/srep36195.

[141] P Senthil Kumar, A Sakunthala, M V Reddy, and Prabu Moni. Structural , morphological , electrical and electrochemical study on plasticized PVdF-HFP / PEMA blended polymer electrolyte for lithium

polymer battery application. 319(May 2017):256–265, 2018. doi: 10.1016/j.ssi.2018.02.022.

[142] Qiangqiang Zhang, Yaxiang Lu, Hao Yu, Gaojing Yang, Qiuyan Liu, Zhaoxiang Wang, Liquan Chen, and Yong-sheng Hu. PEO-NaPF 6 Blended Polymer Electrolyte for Solid State Sodium Battery. *J. Electrochem. Soc.*, 167(7):070523, jan 2020. ISSN 0013-4651. doi: 10.1149/1945-7111/ab741b. URL `https://iopscience.iop.org/article/10.1149/1945-7111/ab741b`.

[143] Angesh Chandra. Hot-pressed PEO-PVP blended solid polymer electrolytes: ion transport and battery application. *Polym. Bull.*, 73(10): 2707–2718, oct 2016. ISSN 01700839. doi: 10.1007/s00289-016-1616-4. URL `http://link.springer.com/10.1007/s00289-016-1616-4`.

[144] Xiangdong Ma, Xiaoxi Zuo, Jinhua Wu, Xiao Deng, Xin Xiao, Jiansheng Liu, and Junmin Nan. Polyethylene-supported ultra-thin polyvinylidene fluoride/hydroxyethyl cellulose blended polymer electrolyte for 5 v high voltage lithium ion batteries. *J. Mater. Chem. A*, 6(4):1496–1503, 2018. ISSN 20507496. doi: 10.1039/c7ta08741a. URL `http://xlink.rsc.org/?DOI=C7TA08741A`.

[145] W.N.E. Wan Mohd Noral Azman, J Jaafar, W.N.W. Salleh, A.F. Ismail, M.H.D. Othman, M.A. Rahman, and F.R.M. Rasdi. Highly selective SPEEK/ENR blended polymer electrolyte membranes for direct methanol fuel cell. *Mater. Today Energy*, 17: 100427, sep 2020. ISSN 24686069. doi: 10.1016/j.mtener.2020.100427. URL `https://doi.org/10.1016/j.mtener.2020.100427https://linkinghub.elsevier.com/retrieve/pii/S2468606920300460`.

[146] Chien A Nguyen, Shanxin Xiong, Jan Ma, Xuehong Lu, and Pooi See Lee. High ionic conductivity P(VDF-TrFE)/PEO blended polymer

electrolytes for solid electrochromic devices. *Phys. Chem. Chem. Phys.*, 13(29):13319–13326, 2011. ISSN 14639076. doi: 10.1039/c0cp01505a. URL `http://xlink.rsc.org/?DOI=c0cp01505a`.

[147] Il-Jin Baek and Won-Ju Cho. Resistive switching characteristics of solution-processed organic-inorganic blended films for flexible memory applications. *Solid. State. Electron.*, 140(October 2017): 129–133, feb 2018. ISSN 00381101. doi: 10.1016/j.sse.2017.10.030. URL `https://doi.org/10.1016/j.sse.2017.10.030https://linkinghub.elsevier.com/retrieve/pii/S0038110117307761`.

[148] Hui Wang, Chiao-Tzu Wang, Fan Xu, Jiang Yang, Jianhua Liu, Wenbin Cai, and Guodong Zhu. Resistive switching and nanoscale chemical mapping of phase separation in PVDF/PMMA/F8T2 ternary thin films. *Polymer (Guildf).*, 153(May):498–506, 2018. ISSN 0032-3861. doi: 10.1016/j.polymer.2018.08.051. URL `https://doi.org/10.1016/j.polymer.2018.08.051`.

[149] M A Khan, Unnat S Bhansali, Dongkyu Cha, and H N Alshareef. All-polymer bistable resistive memory device based on nanoscale phase-separated PCBM-ferroelectric blends. *Adv. Funct. Mater.*, 23(17): 2145–2152, 2013. ISSN 1616301X. doi: 10.1002/adfm.201202724.

[150] Takayuki Kawahara and Hiroyuki Mizuno. *Green Computing with Emerging Memory*, volume 9781461408. Springer New York, 2013. ISBN 978-1-4614-0811-6. doi: 10.1007/978-1-4614-0812-3. URL `http://link.springer.com/10.1007/978-1-4614-0812-3`.

[151] Yu-Chi Chang and Yeong-Her Wang. Resistive Switching Behavior in Gelatin Thin Films for Nonvolatile Memory Application. *ACS Appl. Mater. Interfaces*, 6(8):5413–5421, apr 2014. ISSN 1944-8244. doi:

10.1021/am500815n. URL www.acsami.orghttps://pubs.acs.org/doi/10.1021/am500815n.

[152] A. Rawat, H. K. Mahavar, A. Tanwar, and P. J. Singh. Study of electrical properties of polyvinylpyrrolidone/polyacrylamide blend thin films. *Bull. Mater. Sci.*, 37(2):273–279, 2014. ISSN 02504707. doi: 10.1007/s12034-014-0639-4.

[153] M. Ravi, S. Bhavani, K. Kiran Kumar, and V. V.R. Narasimaha Rao. Investigations on electrical properties of PVP:KIO4 polymer electrolyte films. *Solid State Sci.*, 19:85–93, 2013. ISSN 12932558. doi: 10.1016/j.solidstatesciences.2013.02.006.

[154] R. Poonguzhali, S. Khaleel Basha, and V. Sugantha Kumari. Synthesis and characterization of chitosan/poly (vinylpyrrolidone) biocomposite for biomedical application. *Polym. Bull.*, 74(6):2185–2201, 2017. ISSN 01700839. doi: 10.1007/s00289-016-1831-z.

[155] Jen-taut Yeh, Chin-Lai Chen, K. S. Huang, Y H Nien, J L Chen, and P Z Huang. Synthesis, characterization, and application of PVP/chitosan blended polymers. *J. Appl. Polym. Sci.*, 101(2):885–891, jul 2006. ISSN 0021-8995. doi: 10.1002/app.23517. URL https://onlinelibrary.wiley.com/doi/10.1002/app.23517.

[156] Jamie J Grant, Suresh C Pillai, Tatiana S Perova, Sarah Hehir, Steven J Hinder, Marion McAfee, and Ailish Breen. Electrospun Fibres of Chitosan/PVP for the Effective Chemotherapeutic Drug Delivery of 5-Fluorouracil. *Chemosensors*, 9(4):70, mar 2021. ISSN 2227-9040. doi: 10.3390/chemosensors9040070. URL https://www.mdpi.com/2227-9040/9/4/70.

[157] Young Ho Do, June Sik Kwak, Jin Pyo Hong, Kyooho Jung, and Hyunsik Im. Al electrode dependent transition to bipolar resistive

switching characteristics in pure TiO2 films. *J. Appl. Phys.*, 104(11): 114512, dec 2008. ISSN 0021-8979. doi: 10.1063/1.3032896. URL `http://aip.scitation.org/doi/10.1063/1.3032896`.

[158] Jaeho Choi, Sunghak Park, Joohee Lee, Kootak Hong, Do-Hong Hong Kim, Cheon Woo Moon, Gyeong Do Park, Junmin Suh, Jinyeon Hwang, Soo Young Kim, Hyun Suk Jung, Nam-gyu Gyu Park, Seungwu Han, Ki Tae Nam, and Ho Won Jang. Organolead Halide Perovskites for Low Operating Voltage Multilevel Resistive Switching. *Adv. Mater.*, 28(31):6562–6567, aug 2016. ISSN 09359648. doi: 10.1002/adma.201600859. URL `https://onlinelibrary.wiley.com/doi/10.1002/adma.201600859`.

[159] Niloufar Raeis-Hosseini, Seokjae Lim, Hyunsang Hwang, and Junsuk Rho. Reliable Ge2Sb2Te5-Integrated High-Density Nanoscale Conductive Bridge Random Access Memory using Facile Nitrogen-Doping Strategy. *Adv. Electron. Mater.*, 4(11), 2018. ISSN 2199160X. doi: 10.1002/aelm.201800360.

[160] Suk-Won Hwang, Jun-Kyul Song, Xian Huang, Huanyu Cheng, Seung-Kyun Kang, Bong Hoon Kim, Jae-Hwan Kim, Sooyoun Yu, Yonggang Huang, and John A. Rogers. High-Performance Biodegradable/Transient Electronics on Biodegradable Polymers. *Adv. Mater.*, 26(23):3905–3911, jun 2014. ISSN 09359648. doi: 10.1002/adma.201306050. URL `https://onlinelibrary.wiley.com/doi/10.1002/adma.201306050`.

[161] Fengzhen Lv, Kang Ling, Tingting Zhong, Fuchi Liu, Xiaoguang Liang, Changming Zhu, Jun Liu, and Wenjie Kong. Multilevel Resistive Switching Memory Based on a CH3NH3PbI 3xClx Film with Potassium Chloride Additives. *Nanoscale Res. Lett.*, 15(1), 2020. ISSN 1556276X. doi: 10.1186/s11671-020-03356-3.

[162] Z. W. Dlamini, S. Vallabhapurapu, T. S. Mahule, and V. S. Vallabhapurapu. Electrical conduction and resistive switching in cow milk-based devices prepared using the spin-coat method. *AIP Adv.*, 12 (9):095321, 2022. ISSN 21583226. doi: 10.1063/5.0098976. URL `https://doi.org/10.1063/5.0098976`.

[163] Zolile Wiseman Dlamini, Sreedevi Vallabhapurapu, Shuying Wu, Tebogo Sfiso Mahule, Ananthakrishnan Srivivasan, and Vijaya Srinivasu Vallabhapurapu. Resistive switching memory based on chitosan/polyvinylpyrrolidone blend as active layers. *Solid State Commun.*, 345:114677, apr 2022. ISSN 00381098. doi: 10.1016/j.ssc.2022.114677. URL `https://linkinghub.elsevier.com/retrieve/pii/S0038109822000254`.